



**DEVELOPMENT OF PHASE RETRIEVAL
TECHNIQUES IN OPTICAL MEASUREMENT**

BY

NIU HONGTAO

(M. Eng.)

A THESIS SUBMITTED

FOR THE DEGREE OF DOCTOR OF PHILOSOPHY

DEPARTMENT OF MECHANICAL ENGINEERING

NATIONAL UNIVERSITY OF SINGAPORE

2011

ACKNOWLEDGEMENTS

The author would like to take this opportunity to gratefully acknowledge his supervisors **A/Prof. Quan Chenggen** and **A/Prof. Tay Cho Jui** for their favorable suggestions and technical discussions throughout the research. It is their inspiration, guidance and support that enable him to complete this work.

The author would like to acknowledge all staffs of the Experimental Mechanics Laboratory and the Strength of Materials Lab for their helps with experimental setup and general advice during his study. The author would like to thank Dr. Basanta Bhaduri for his invaluable suggestions.

The author would also like to thank his peer research students for their favorable discussions and helps in the Laboratory.

Finally, the author is forever indebted to his parents for their understanding, endless patience and encouragement when it was most required.

TABLE OF CONTENTS

ACKNOWLEDGEMENTS	i
TABLE OF CONTENTS	ii
SUMMARY	v
LIST OF TABLES	vii
LIST OF FIGURES	viii
NOMENCLATURE	xii
CHAPTER 1 INTRODUCTION	1
1.1 Optical measurement techniques	1
1.2 Challenges in optical measurement	4
1.2.1 Phase retrieval	5
1.2.2 Phase unwrapping	6
1.3 Work scope	7
1.4 Outline of thesis	8
CHAPTER 2 LITERATURE REVIEW	10
2.1 Review of optical techniques for measurement	10
2.1.1 Incoherent optical measurement techniques	10
2.1.1.1 Shadow moiré interferometry	10
2.1.1.2 Fringe projection technique	13
2.1.2 Coherent optical measurement techniques	14
2.1.2.1 Electronic speckle pattern interferometry (ESPI)	14
2.1.2.2 Digital speckle shearing interferometry (DSSI)	19
2.1.2.3 Multiple-wavelength interferometry	22
2.1.3 Phase retrieval techniques	25

2.1.3.1	Phase shifting techniques	25
2.1.3.2	Fourier transform method	26
2.2	Continuous wavelet transform (CWT) in optical measurement	31
2.3	Windowed Fourier transform (WFT) in optical measurement	39
CHAPTER 3	DEVELOPMENT OF THEORY	45
3.1	Two-dimensional (2D) CWT for phase retrieval	45
3.1.1	Limitations of previous 2D CWT	47
3.1.2	Advanced 2D Gabor CWT	50
3.2	Improved WFT for fringe demodulation	55
3.2.1	Limitations of WFT with convolution algorithm	55
3.2.2	Phase retrieval using improved WFT	56
3.2.3	Suppression of boundary effect	60
3.3	Phase fringe denoising using windowed Fourier filtering	62
3.3.1	Phase retrieval for relatively large deformation measurement	63
3.3.1.1	Windowed Fourier filtering	63
3.3.1.2	Iterative sine-cosine average filtering	65
3.3.2	Combined filtering technique for noise reduction	66
3.3.2.1	Phase error correction algorithm	68
CHAPTER 4	EXPERIMENTAL WORK	72
4.1	ESPI with carriers	72
4.2	DSSI with carriers	74
4.3	ESPI with temporal phase shifting	75
4.4	Two-wavelength DSSI system	77
CHAPTER 5	RESULTS AND DISCUSSION	80
5.1	Two-dimensional CWT for phase retrieval in ESPI	80
5.1.1	Simulation results	80

5.1.2	Experimental results	85
5.2	Improved WFT for fringe demodulation in DSSI	89
5.2.1	Simulated analysis	89
5.2.2	Experimental results	96
5.3	Relatively large deformation measurement	100
5.3.1	Phase fringe denoising in ESPI	100
5.3.1.1	Simulated results	100
5.3.1.2	Experimental results	103
5.3.2	Phase fringe denoising in DSSI	106
5.4	Two-wavelength DSSI using combined filter	111
CHAPTER 6	CONCLUSIONS AND RECOMMENDATIONS	117
6.1	Concluding remarks	117
6.2	Recommendations	119
REFERENCES		121
APPENDICES		131
Appendix A.	Code for 2D Gabor and 2D fan CWT	131
Appendix B.	Code for improved WFT	136
Appendix C.	List of publications	141

SUMMARY

Optical measurement techniques are very important in industry for their widely varying applications such as nondestructive testing and phase retrieval. In this thesis, time-frequency analysis based algorithms for optical phase retrieval in digital speckle interference measurement were studied. To improve the noise reduction capability of the phase retrieval techniques, two-dimensional (2D) Gabor continuous wavelet transform (CWT) and advanced windowed Fourier transform (WFT) were developed for phase retrieval and noise reduction for noisy fringe patterns.

A new algorithm of 2D Gabor CWT for speckle noise reduction and phase retrieval was developed for speckle fringe pattern demodulation with carriers. Experiment using electronic speckle pattern interferometry (ESPI) was conducted to measure the deformation on an object surface with sub-wavelength sensitivity. Compared with other time-frequency analysis based algorithms, such as Fourier transform, one-dimensional (1D) CWT and 2D fan CWT, the proposed 2D Gabor CWT has better noise immunity for speckle fringe demodulation. In addition, the proposed 2D Gabor CWT overcomes the problem of previous 2D fan CWT which fails to reduce speckle noise or show correct phase values in some speckle fringe patterns due to the narrow bandwidth of 2D fan wavelet. The experimental results obtained have validated the proposed algorithm.

Another new algorithm of improved WFT for phase retrieval from speckle fringe patterns was also proposed in this thesis. Windowed Fourier transform is an important time-frequency analysis algorithm based on Fourier transform in fringe analysis. Unlike CWT which has a variable resolution, WFT has a fixed time and frequency resolution in the processing of fringe patterns. The appropriate window size in both space and frequency domain is favorable in noise reduction and phase retrieval. Windowed Fourier transform has promising potential in fringe analysis and the highly efficient algorithm of WFT can reduce computation time. The proposed advanced WFT which employs fast Fourier transform reduces the computation time significantly compared with the previous WFT with convolution method. The experimental results obtained on out-of-plane displacement derivative measurement using digital speckle-shearing interferometry (DSSI) have also shown a good noise reduction capability of the proposed method. It is observed that the proposed CWT and WFT have a good noise reduction capability in phase retrieval and subsequently better phase fringe patterns can be obtained.

A two-wavelength DSSI using simultaneous red and green lights illumination was also proposed. Windowed Fourier transform was employed for phase retrieval of the speckle phase fringe patterns obtained by phase shifting method and it shows better results than the sine-cosine average filtering method. Furthermore, a phase error correction algorithm was also proposed to improve the sensitivity of the proposed technique.

A list of publications arising from this research is shown in Appendix C.

LIST OF TABLES

Table 5.1	Comparison between the proposed method and the WFF with convolution method	94
Table 5.2	Comparison of RMSE between the Fourier transform, 2D Gabor CWT and proposed WFF method	95
Table 5.3	Parameters used for the fast WFF algorithm	113

LIST OF FIGURES

Fig. 2.1	Shadow moiré fringe pattern on a coin's surface	11
Fig. 2.2	Schematic diagram of shadow moiré technique	12
Fig. 2.3	Phase shifting ESPI setup	18
Fig. 2.4	A schematic drawing of DSSI	22
Fig. 2.5	(a) A simulated intensity signal with a normally distributed random noise; (b) Fourier spectrum of the signal; (c) selected positive first order spectrum from (b); (d) retrieved wrapped phase; (e) unwrapped phase	30
Fig. 2.6	(a) A 1D Morlet wavelet and its spectrum; (b) a scalogram of $ Wf(q, m) $ for the signal shown in Fig. 2.5(a) and the dash line represents the ridge of CWT; (c) unwrapped phase using CWT	38
Fig. 2.7	Basis of transform for time-frequency analysis	39
Fig. 3.1	(a) Real part of a 2D Morlet wavelet; (b) imaginary part of a 2D Morlet wavelet; (c) Fourier spectrum of a 2D Morlet wavelet	47
Fig. 3.2	(a) Real part of a 2D fan wavelet; (b) imaginary part of a 2D fan wavelet; (c) Fourier spectrum of a 2D fan wavelet	49
Fig. 3.3	Flow chart of the Gerchberg extrapolation method	61
Fig. 3.4	An example of fringe extrapolation	62
Fig. 3.5	A flow chart of the phase error correction algorithm	70
Fig. 3.6	(a) Subroutine 1; (b) Subroutine 2	71
Fig. 4.1	ESPI setup for deformation measurement	73
Fig. 4.2	DSSI for deformation derivative measurement with carriers	75
Fig. 4.3	ESPI for deformation measurement with phase shifting	76
Fig. 4.4	Two-wavelength DSSI for deformation derivative measurement	78

LIST OF FIGURES

Fig. 5.1	(a) Original phase values $\phi(X)$; (b) simulated phase values with a carrier; (c) simulated fringe pattern with <i>WGN</i>	81
Fig. 5.2	(a) Wrapped phase map retrieved using 2D Gabor CWT; (b) wrapped phase map retrieved using advanced 2D fan CWT	82
Fig. 5.3	(a) Error map by 2D Gabor CWT; (b) error map by advanced 2D fan CWT	83
Fig. 5.4	Error on the 256 th row of phase maps obtained using the two methods: the solid line denotes the 2D Gabor CWT errors and the dash line denotes the advanced 2D fan CWT errors	84
Fig. 5.5	Speckle fringe pattern with spatial carriers	85
Fig. 5.6	(a) Wrapped phase map by advanced 2D fan CWT; (b) wrapped phase map by 2D Fourier transform; (c) wrapped phase map by 2D Gabor CWT	86
Fig. 5.7	Unwrapped phase map with carriers removed using 2D Gabor CWT	87
Fig. 5.8	(a) 3D phase map using advanced 2D fan CWT; (b) 3D phase map using 2D Fourier transform; (c) 3D phase map using 2D Gabor CWT	88
Fig. 5.9	(a) Simulated phase map; (b) simulated speckle-shearing fringe pattern	92
Fig. 5.10	Extrapolated fringe pattern	93
Fig. 5.11	(a) Retrieved phase map using the proposed WFF method; (b) retrieved phase map using the WFF with convolution method	93
Fig. 5.12	(a) Error map by the proposed WFF method; (b) error map by the WFF with convolution method	94
Fig. 5.13	(a) A simulated speckle fringe pattern with both dense and sparse fringe patterns; (b) error map using the proposed WFF method without using boundary extension	95
Fig. 5.14	(a) Speckle fringe pattern indicating displacement derivative; (b) carrier fringe pattern; (c) extrapolated speckle fringe pattern based on (a)	97
Fig. 5.15	(a) Retrieved phase map using fast Fourier transform method; (b) retrieved phase map using proposed WFF method; (c) retrieved phase map using WFF with convolution method	98

LIST OF FIGURES

Fig. 5.16	(a) Unwrapped phase map after carrier removal using proposed WFF method; (b) unwrapped phase map after carrier removal using WFF with convolution method; (c) unwrapped phase values along central line CC in (a) and (b)	99
Fig. 5.17	Simulated wrapped phase map with speckle noise	101
Fig. 5.18	(a) Phase values along the first row of pixels in Fig. 5.17; (b) filtered phase fringe pattern using fast WFF technique	102
Fig. 5.19	A plot of speckle size versus the RMSE	103
Fig. 5.20	Phase difference map retrieved using Carré phase shifting method	104
Fig. 5.21	(a) Filtered phase fringe pattern by fast WFF technique; (b) filtered phase fringe pattern by conventional sine-cosine average filtering technique	105
Fig. 5.22	(a) Unwrapped phase map by fast WFF technique; (b) unwrapped phase map by conventional sine-cosine average filtering technique	106
Fig. 5.23	(a) Phase difference retrieved for red light; (b) phase difference retrieved for green light	107
Fig. 5.24	(a) Filtered phase of Fig. 5.23(a) obtained with ISCAF; (b) raw phase difference of the synthetic wavelength obtained by subtracting the phase difference maps between the red and green lights	108
Fig. 5.25	(a) Filtered phase difference of the synthetic wavelength obtained with ISCAF; (b) filtered phase of Fig. 5.23(a) using fast WFF	109
Fig. 5.26	Unwrapped phase map of Fig. 5.25(a)	110
Fig. 5.27	Unwrapped phase map of Fig. 5.25(b)	110
Fig. 5.28	Phase values along cross-section A-A from the unwrapped phase maps using two filtering techniques	111
Fig. 5.29	(a) Wrapped phase $\Delta\phi_r$ for red light; (b) wrapped phase $\Delta\phi_g$ for green light; (c) filtered wrapped phase $\overline{\Delta\phi_r}$; (d) filtered wrapped phase $\overline{\Delta\phi_g}$	112
Fig. 5.30	(a) Phase $\Delta\phi_s$ for synthetic wavelength $\lambda_s = 3.3398 \mu\text{m}$; (b) filtered phase $\overline{\Delta\phi_s}$	113
Fig. 5.31	(a) Unwrapped phase $\Delta\phi_{gu}$ without combined filter; (b) corresponding 3D plot	115

- Fig. 5.32 (a) Phase values (Line 1) and corresponding values of $Coef_diff$ 116 (Line 2) on cross-section A-A in Fig. 5.31(a); (b) initial values of Fig. 5.32(a) (from 1 to 120 pixels); (c) phase map $\overline{\Delta\phi_{gu}}$ with combined filter

NOMENCLATURE

a	Background intensity
a_o	Amplitude of object beam
a_R	Amplitude of reference beam
$angle$	Taking argument operation
$arctan$	Arc tangent operation
A	Fourier transform of a
b	Modulation factor
\mathbf{b}_t	Translation parameter of (b_x, b_y)
b_x	Translation along the x -axis
b_y	Translation along the y -axis
D	Windowed Fourier element
\hat{D}	Fourier spectrum of a windowed Fourier element
f	Carrier frequency in the x direction
f_{1d}	A periodic signal
F	Fourier transform
F^{-1}	Inverse Fourier transform
g	Gaussian function
\hat{G}	Fourier spectrum of a Gaussian function
h	Height

i	Square root of -1
I	Intensity of a fringe pattern
I^l	A local speckle fringe pattern
I_{l0}	Background intensity of a local fringe pattern
I_{l1}	Modulation factor of a local fringe pattern
Im	Operation for taking imaginary part
I_{m_1}	Intensity of an interferogram by phase shifting
I_s	Intensity of a resultant speckle fringe pattern
\hat{I}	Fourier transform of I
I'	Intensity of an interferogram after object deformation
k_0	Central frequency along the x -axis
K	Frequency coordinates of (ω_x, ω_y)
K_θ	Central frequency of a 2D Morlet wavelet
m	Translation variable on the x -axis
m_1	Number of phase shifted frames
p	Grating period
P	Local fringe period
P_1	Phase in a complex form
q	Scale
$r_{-\theta}$	Rotation matrix
Re	Operation for taking real part
Sf	Coefficients of windowed Fourier transform

u	Displacement along the x -axis
$\frac{\partial u}{\partial x}$	Displacement derivative of u
U_o	Object beam
U_R	Reference beam
U_z	Wavefront of light
w	Out-of-plane deformation
$\frac{\partial w}{\partial x}$	Displacement derivative of w
Wf	Coefficients of 1D wavelet transform
WT	2D wavelet transform
\mathbf{X}	Spatial coordinates of (x, y)
δ	Dirac function
δ_1	Phase shifting value
ε	Angular frequency variable in the x -axis
εl	Lower integral limit of ε
εh	Upper integral limit of ε
ϕ	Phase
ϕ'	Phase derivative
$\Delta\phi$	Phase difference
ϕ_a	Phase after object deformation
ϕ_b	Phase before object deformation
ϕ_o	Phase of object beam
ϕ_R	Phase of reference beam

φ	Local fringe direction
γ	Angular frequency variable in the y -axis
γ_l	Lower integral limit of γ
γ_h	Upper integral limit of γ
λ	Wavelength
σ	Parameter for a Gaussian window
θ	A rotation angle
θ_1	Illumination angle
θ_2	View angle
θ_3	Angle between illumination direction and view direction
ω	Angular frequency coordinate
ω_0	A fixed frequency
ω_x	Frequency along the x -axis
ω_y	Frequency along the y -axis
ψ	Wavelet function
$\hat{\psi}$	Fourier spectrum of ψ
ψ_{Fan}	2D fan wavelet
$\hat{\psi}_{Fan}$	Fourier spectrum of a 2D fan wavelet
ψ_G	2D Gabor wavelet
$\hat{\psi}_G$	Fourier spectrum of a 2D Gabor wavelet
ψ_M	2D Morlet wavelet
Δ_x	Shearing distance in the x direction

—	Filtering operator
*	Complex conjugation operator
^	Fourier spectrum

CHAPTER ONE

INTRODUCTION

Optical measurement techniques are among the most sensitive known today apart from being noncontact, noninvasive, and fast. In recent years, the use of optical measurement techniques has dramatically increased, and applications range from determining the topography of landscapes to checking the roughness of polished surfaces. Further, they have been widely used in the industry, such as manufacturing, aircraft industry and biomedical engineering.

1.1 Optical measurement techniques

Any of the characteristics of a light wave, such as amplitude, phase, length, frequency, polarization, and direction of propagation, can be modulated by the measurand. On demodulation, the value of the measurand at a spatial point and at a particular time instant can be obtained. Optical measurement techniques can effect measurement at discrete points or over the whole field with extremely fine spatial resolution. These techniques have been greatly developed with the development of electronic and software technology. The fundamental system of optical measurement techniques currently includes advanced computer, analysis software, optical source, optical components and high resolution charge coupled device (CCD) camera. In general, optical measurement techniques can be categorized into two types, namely coherent

light measurement and incoherent light measurement. Both measurements have some similarities and differences. The main similarity is that the light intensity recorded by CCD camera is utilized to retrieve the measurand in both measurements. The difference is that for the former the recorded intensity is generated by interference light, while for the latter it is generated by non-interference light. The commonly used methods of coherent light measurement include heterodyne interferometry (Massie et al, 1979), speckle interferometry (Dainty, 1975; Ennos, 1975; Goodman, 1976), holographic interferometry (Vest, 1979; Kreis, 2005) and white light interferometry (Sandoz, 1997), while for incoherent light measurement there are fringe projection profilometry (Huang et al, 2003), moiré fringe interferometry (Jin et al, 2000; Jin et al, 2001; Yokozeki et al, 1975) and digital image correlation techniques (Chu et al, 1985; Bruck et al, 1989).

Optical measurement techniques have received a great deal of attention nowadays and been widely applied in semiconductor manufacturing industry, automotive industry, medical industry and bioengineering. With the applications of computer and CCD camera instead of the traditional photographic film, the digital image processing techniques (Funnell, 1981) of the optical interference images have played a dominant role in optical measurement. To extract the phase information directly from the intensity distribution recorded has become an important technique in optical measurement called the phase retrieval (Robinson and Reid, 1993; Dorrió and Fernández, 1999; Malacara et al, 1998). The commonly used methods of quantitative phase evaluation include temporal phase shifting method, spatial phase shifting

method and Fourier transform method. In the methods, the principal value of the optical phase is computed by an arctan function whose argument is related to intensity values.

Optical interference measurement such as holography interferometry, can produce special fringe patterns recording the amplitude and phase information of a detected object. After reconstruction of the object wavefront, a three-dimensional (3D) image of the object can be obtained. With the development of digital holography, holographic interferometry technology has been used for high-precision measurement due to its quantitative measurement. Similar to holographic interferometry, ESPI, also known as TV holography, is a development of two-beam speckle interference for deformation measurement. Unlike holographic interferometry, ESPI uses correlation fringe patterns obtained from speckle interference to detect phase change of an object wavefront. Electronic speckle pattern interferometry can be used for deformation measurements with high accuracy, non-contact and real-time display. As a development from single wavelength interferometry, two-wavelength interferometry was also proposed for profile and deformation measurement of relatively large dimension. Two wavelengths are used to generate two different interferograms of the single wavelength and the phase maps of the two interferograms are then extracted using phase shifting techniques. The subtraction of two phase maps generates a phase map of a synthetic wavelength representing the profile of the object. This technique is able to extend the measurement range due to the longer synthetic wavelength. Advanced 3D topography measurement methods also include moiré (Takasaki, 1973)

and fringe projection techniques (Takeda et al, 1982). Moiré and fringe projection techniques used as tools for measuring object profile and displacement have had a history of several decades because of the advantages of simplicity, low costs and non-contact and non-destructive measurement.

Nowadays, the main focuses in the phase evaluation technology are mostly on the improvement of accuracy of phase retrieval and phase unwrapping. Since the principal phase values retrieved by the phase retrieval techniques range from $-\pi$ to π , phase unwrapping is required to remove the discontinuity of the wrapped phase map in order to obtain correct phase values. Spatial phase unwrapping becomes a complex issue when a wrapped phase map is corrupted by heavy speckle noise. Besides, breakpoints in a wrapped phase map may appear due to noise or physical breakpoints on the surface of a test object and the correct integral multiples of 2π at these locations will be lost. It is a challenge for spatial phase unwrapping techniques to automatically distinguish and unwrap this type of wrapped phase maps without human intervention. Other important issues are noise reduction and improvement in accuracy and computational speed for phase retrieval in optical measurement.

1.2 Challenges in optical measurement

There are still many challenges in optical measurement, such as improvements in accuracy and stability. However, two issues are of fundamental importance, namely phase retrieval and unwrapping.

1.2.1 Phase retrieval

Phase retrieval is an improvement from fringe tracking (Judge and Bryanston-Cross, 1994) to determine phase values of an interferogram. The accuracy of optical measurement based on fringe tracking has been greatly improved since phase retrieval technique was developed. Furthermore, phase retrieval is normally a simple processing technique. There are several commonly used phase retrieval techniques, such as Fourier transform method (Takeda and Mutoh, 1983; Su and Chen, 2001), phase shifting technique (Creath, 1985; Kong and Kim, 1995; Yamaguchi and Zhang, 1997), CWT method (Watkins et al, 1997; Durson et al, 2004; Gdeisat et al, 2006) and WFT method (Qian, 2004; Qian, 2007a; Qian, 2007b). Among these phase retrieval methods, phase shifting technique has a relatively higher accuracy. It requires at least three image patterns for phase retrieval, overcoming phase-ambiguity problem. Phase shifting technique is basically used in static measurements. However, dynamic measurements can be also achieved by using the phase shifting technique when a special phase mask polarizer and sensor array are employed (Wyant, 2003). Unlike phase shifting technique, Fourier transform method requires only one fringe pattern with carriers introduced for phase extraction, and therefore, this technique can be easily applied to dynamic measurement. Wavelet transform method is one of the most important time-frequency analysis methods in signal processing and can be applied to extract phase information from an optical fringe pattern. It also has a better noise reduction capability than the Fourier transform method. Another important time-frequency analysis method is called WFT method. It can be considered as a local

Fourier transform of the fringe patterns, and therefore it has a better noise reduction capability than the Fourier transform method in optical measurement. Since the WFT method can produce better accuracy than the CWT method, it has received much attention in recent years.

1.2.2 Phase unwrapping

Phase unwrapping technique is a necessary post-processing technique after phase retrieval technique has been applied to retrieve a wrapped phase pattern. Speckle noise and breakpoints in a wrapped phase map are two major factors affecting the unwrapping process. It is necessary to overcome these problems. Phase unwrapping techniques can be categorized as spatial phase unwrapping (Macy, 1983; Ghiglia et al, 1987; Xu and Cumming, 1996; Ghiglia and Pritt, 1998) and temporal phase unwrapping (Huntley and Saldner, 1993; Saldner and Huntley, 1997a; Saldner and Huntley, 1997b; Huntley and Saldner, 1997a; Huntley and Saldner, 1997b). Spatial phase unwrapping is simple and requires only one wrapped phase map, while temporal phase unwrapping which was proposed to measure the surface profile of a discontinuous object requires a series of wrapped phase maps with different fringe periods. There are several commonly used spatial phase unwrapping techniques, such as branch cut algorithm (Goldstein et al, 1988; Xiao et al, 2007), quality-guided path following algorithm (Bone, 1991; Quiroga et al, 1995; Lim et al, 1995), mask cut algorithm (Flynn, 1996), Flynn's minimum discontinuity approach (Flynn, 1997), unweighted least-squares phase unwrapping algorithm (Ghiglia and Romero, 1994),

weighted least-squares phase unwrapping algorithm (Lu et al, 2007) and minimum L^p -Norm algorithm (Ghiglia and Romero, 1996). The first four algorithms perform the path-following method for phase unwrapping while the last three perform the path-independent method. Obviously, spatial phase unwrapping methods are based on 2D phase unwrapping and temporal phase unwrapping method is based on 1D phase unwrapping along the temporal axis. Therefore, temporal phase unwrapping method is employed to unwrap the wrapped phase maps pixel by pixel and the adjacent pixels will not affect each other. One advantage of the temporal phase unwrapping method is that it has a good noise immune capability than the spatial phase unwrapping. However, it requires more wrapped phase maps with different fringe periods.

1.3 Work scope

The work scope of the study is focused on developing advanced phase retrieval techniques to reduce speckle noise in optical measurement. In this thesis, the time-frequency analysis algorithms for phase retrieval are studied. The applications of 1D CWT and 2D CWT in optical techniques are studied. Two-dimensional Gabor CWT for speckle noise reduction and phase retrieval is developed for deformation measurement using ESPI. Furthermore, another important time-frequency analysis algorithm, namely 2D WFT is studied in detail due to its better noise reduction capability for phase retrieval. An improved algorithm of WFT is proposed to reduce the computation time significantly compared with the conventional convolution algorithm of WFT. The same is applied to retrieve phase of the fringe patterns from

DSSI for displacement derivative measurement. Meanwhile, two-wavelength DSSI with simultaneous illumination is also proposed for displacement derivative measurement. A phase error correction algorithm is also proposed to improve the sensitivity of the two-wavelength DSSI.

1.4 Outline of thesis

The thesis is organized into six chapters.

In Chapter 1, various optical measurement techniques and the importance of phase retrieval are briefly introduced. The work scope is also included.

In Chapter 2, a literature review on optical measurement is presented. Optical measurement techniques including fringe projection, shadow moiré interferometry, ESPI and DSSI, as well as phase retrieval techniques are reviewed. In addition, the application of CWT to optical measurement for phase retrieval is reviewed. The important time-frequency analysis technique, WFT in optical measurement for phase retrieval is reviewed.

In Chapter 3, the theory of 2D Gabor CWT for phase retrieval is presented. The limitation of 2D fan CWT is also shown and the selection of wavelet functions is discussed. Furthermore, an improved WFT to reduce the computation time for fringe demodulation is also proposed and a theoretical derivation is presented. Windowed Fourier filtering (WFF) method in DSSI for noise reduction of phase fringe patterns is proposed. A theory of two-wavelength DSSI using WFT and a phase error correction algorithm for noise reduction is presented.

In Chapter 4, experimental work based on ESPI and DSSI with carriers, ESPI with temporal phase shifting and two-wavelength DSSI system is presented.

In Chapter 5, simulation and experimental results are presented. The limitations and accuracy of the proposed methods are discussed. The novelties of the proposed methods are stressed.

In Chapter 6, conclusions of this study are made and the recommendations for future research works are discussed.

CHAPTER TWO

LITERATURE REVIEW

2.1 Review of optical techniques for measurement

Modern optical measurement techniques have two important parts, optical theory of measurement and image processing. This section provides a review on the principle of optical methods and the applications of time-frequency analysis for phase retrieval.

2.1.1 Incoherent optical measurement techniques

The commonly used incoherent optical measurement techniques include shadow moiré interferometry and fringe projection technique, which provide structured light pattern for quantitative measurement.

2.1.1.1 Shadow moiré interferometry

Shadow moiré interferometry is a commonly used method for 3D profile measurement in the early period, as proposed by Takasaki (1970, 1973) and Meadows et al (1970). The principle of this technique is to use the mechanical interference of a grating and its shadow projected on the surface of a test object to measure the surface profile. The so called mechanical interference can produce a fringe pattern with lower frequency than the grating used. As shown in Fig. 2.1 is a moiré fringe pattern on a coin's surface. The wide fringe pattern is moiré fringe pattern representing the surface

information of the coin and the dense fringe pattern is generated by the grating which needs to be filtered out. Moiré fringe pattern can be represented by cosine function which is similar to the fringe pattern generated in laser interferometry and therefore, phase retrieval techniques can be employed to extract the phase information representing the measurand for the measurement. In addition, Choi and Kim (1998) proposed a phase shifting projection moiré method to measure 3D fine objects at a high measurement speed. This method is capable of removing undesirable high-frequency original grating patterns using a time-integral fringe capturing scheme. Jin et al (2001) implemented a frequency-sweeping technique to measure the spatially separated surfaces of objects with rotation of a grating. This technique utilizes Fourier-transform technique to analyze the intensity signal of moiré fringe patterns in temporal domain using the temporal carrier frequency. Therefore, moiré effect has an important impact in optical measurement.



Fig. 2.1 Shadow moiré fringe pattern on a coin's surface

The schematic diagram of shadow moiré technique is shown in Fig. 2.2. According to the principle of moiré technique, the intensity of a moiré fringe pattern recorded by the CCD camera is given by (Robinson and Reid, 1993)

$$I(x, y) = a + b \cos[\phi(x, y)] \quad (2.1)$$

where a is background intensity, b is the modulation factor. The relation between the measured height $h(x, y)$ and the phase $\phi(x, y)$ is given as

$$\phi(x, y) = 2\pi \frac{u_1 + u_2}{p} = 2\pi \frac{h(x, y)}{p} (\tan \theta_1 + \tan \theta_2) \quad (2.2)$$

where θ_1 and θ_2 are the illumination angle and view angle respectively, p is the grating period.

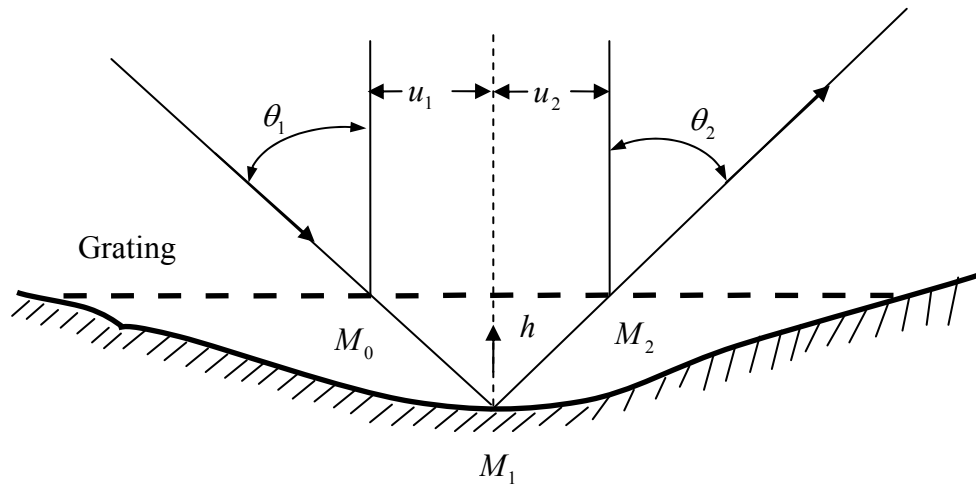


Fig. 2.2 Schematic diagram of shadow moiré technique

2.1.1.2 Fringe projection technique

Fringe projection technique has an important application in 3D surface contouring. Takeda et al (1982) first employed a fast Fourier transform method to a noncontour type of fringe pattern, which showed a better accuracy than the previous methods and had an advantage of simpleness over fringe-scanning techniques (Bruning, 1978). This study proposed an automatic fringe analysis technique using time-frequency algorithm, Fourier transform method, for phase retrieval. Furthermore, Takeda and Mutoh (1983) applied this technique to the automatic 3D shape measurement and verified it by experiments. The projected fringe pattern of a grating was processed in both spatial frequency domain and space-signal domain. A much higher sensitivity than the conventional moiré technique can be obtained and this technique is capable of application to dynamic deformation measurement. Huang et al (1999) proposed a special fringe projection technique using a color fringe pattern with RGB three colors for high-speed 3D surface profile measurement. Phase shifting method was employed and therefore, it had the potential for dynamic deformation measurement. Later, Huang et al (2003) proposed a high-speed 3D shape measurement technique using phase shifting of a color fringe pattern which had a potential measurement speed up to 100 Hz. In addition, Guo et al (2004) proposed a Gamma correction algorithm to reduce the gamma nonlinearity of the video projector for digital fringe projection profilometry, which can improve the accuracy and resolution of the measurement. Later, Guo et al (2005) applied a least-squares calibration method in fringe projection profilometry to retrieve the related parameters. Zhang and Yau (2007) proposed a

generic nonsinusoidal phase error correction algorithm using a digital video projector for 3D shape measurement. A small look-up table was utilized to reduce the phase error for a three-step phase shifting algorithm. Because of the advantages of accuracy and portability using fringe projection technique, it has been applied to reverse engineering as well. Burke et al (2002) employed a calibrated LCD matrix for fringe-pattern generation in the reverse engineering for profile retrieval.

2.1.2 Coherent optical measurement techniques

Coherent optical measurement techniques for high precision measurement normally utilize light interference of two beams, one for the object beam and the other for the reference beam. This section provides a review on the various coherent optical measurement techniques, *viz* ESPI, DSSI and multiple-wavelength interferometry.

2.1.2.1 Electronic speckle pattern interferometry (ESPI)

Electronic speckle pattern interferometry has been widely used to nondestructive evaluation (NDE) since 1970's. Due to its versatility, ESPI has replaced many of the film-based methods. Løkberg and Høgmoen (1976) proposed a simple approach using phase modulation with time-average ESPI for vibration measurement. This technique is able to produce a phase contour map of a vibrating object for the measurement. In 1977, Høgmoen and Løkberg (1977) employed phase modulation in time-average ESPI for real-time detection and measurement of small vibrations. Slettemoen (1980) proposed an ESPI system based on a reference beam which would not be affected by

dust and scratches on optical components. Later, Løkberg and Malmo (1988) employed ESPI for the detection of defects in composite materials. This technique is able to reveal extremely small abnormal surface behavior of composite materials.

The phase shifting method is normally incorporated in ESPI due to its high inherent accuracy. A computerized phase shifting speckle interferometer (PSSI) was developed by Johansson and Predko (1989) for deformation measurement. Furthermore, Joenathan and Khorana (1992) also introduced a phase stepping method by stretching a fiber wrapped around a piezoelectric transducer in PSSI. Minimization methods of a phase drift caused by temperature fluctuation were also studied. In 1993, Kato et al (1993) proposed a phase shifting method in ESPI using the frequency modulation capability of a laser diode for automatic deformation measurement and achieved an accuracy of better than $\lambda/30$. In addition, Wang et al (1996) compared three different image-processing methods using ESPI technique for vibration measurement. In 2003 Trillo et al (2003) also employed a spatial Fourier transform method to measure the complex amplitude of a transient surface acoustic wave using ESPI.

Unlike digital holography, ESPI does not require an image reconstruction. It only requires a CCD camera with a relatively lower resolution for deformation measurement (Yamaguchi and Zhang, 1997; Cuhe et al, 1999; Yamaguchi, 2006). A commonly used phase shifting ESPI setup is shown in Fig. 2.3. In this setup, a laser beam from a He-Ne laser is expanded by a beam expander for illumination. A beam splitter is employed to separate the illumination beam into an object and a reference

beam. The object beam illuminates the test object and is reflected back through the beam splitter to the CCD camera, while the reference beam illuminates a reference plane and is reflected back through the beam splitter to the CCD camera. Both object and reference beams interfere at the CCD plane. The object beam is given by

$$U_o(x, y) = a_o(x, y) \exp[i\phi_o(x, y)] \quad (2.3)$$

where $a_o(x, y)$ represents the amplitude and $\phi_o(x, y)$ represents the phase of the object beam and $i = \sqrt{-1}$. Similarly, the reference beam is given by

$$U_r(x, y) = a_r(x, y) \exp[i\phi_r(x, y)] \quad (2.4)$$

where $a_r(x, y)$ and $\phi_r(x, y)$ represent amplitude and phase of the reference beam, respectively. The intensity of an interferogram is given by

$$\begin{aligned} I &= [U_o + U_r] \times [U_o + U_r]^* \\ &= a_o^2 + a_r^2 + 2a_o a_r \cos(\phi_o - \phi_r) \end{aligned} \quad (2.5)$$

where (x, y) is omitted for simplicity and symbol $*$ represents a conjugate operation.

The interferogram appears as a speckle pattern due to the diffused reflection of the object and reference beams. Intensity of the interferogram captured after the object deformation is given by

$$I' = a_O^2 + a_R^2 + 2a_O a_R \cos(\phi_O + \Delta\phi - \phi_R) \quad (2.6)$$

where $\Delta\phi$ represents the phase difference introduced by the object deformation. By subtraction of the intensities recorded before and after the deformation, the resultant speckle fringe pattern is given by

$$I_S = |I - I'| = 4a_O a_R \left| \sin(\phi_O - \phi_R + \frac{\Delta\phi}{2}) \sin(\frac{\Delta\phi}{2}) \right| \quad (2.7)$$

When the illumination angle between the illumination direction of the object beam and the normal line perpendicular to the object surface is approximately zero, the relationship between the phase difference and out-of-plane deformation is given by

$$\Delta\phi = \frac{4\pi w}{\lambda} \quad (2.8)$$

where w and λ represent the out-of-plane deformation of the object surface and the wavelength of the illuminating beam, respectively.

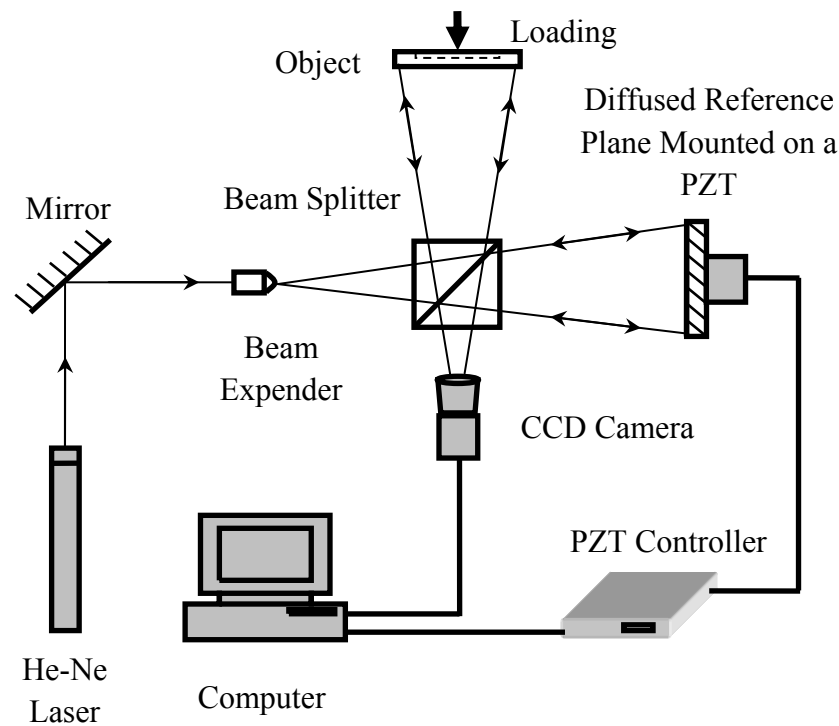


Fig. 2.3 Phase shifting ESPI setup

In addition, ESPI can also be applied to measure in-plane displacement. In 1990, Moore and Tyrer (1990) devised an ESPI setup to measure in-plane displacement which can measure two in-plane interferograms at the same time. Later, Fan et al (1997) presented a work on whole field in-plane displacement measurement using ESPI with optical fiber phase shifting technique. Electronic speckle pattern interferometry can also be applied to profile measurement. Ford et al (1993) conducted surface profile measurement using ESPI with a sinusoidal frequency modulation and Ettemeyer (2000) applied ESPI to measure the shape and 3D deformation of an object for quantitative 3D strain analysis.

2.1.2.2 Digital speckle shearing interferometry (DSSI)

As in ESPI, DSSI is a technique for the measurement of displacement derivative on the surface of deformed object (Rastogi, 2001). In 1973, Hung and Taylor (1973) introduced digital speckle-pattern shearing interferometry as a tool to measure derivative of surface-displacement. This technique can reduce the stringent requirement for environmental stability during testing. It is not that sensitive to vibration and has been applied to various in-situ inspections, such as aircraft tire inspection. In 1979, Hung and Durelli (1979) developed a setup using a multiple image-shearing camera to simultaneously measure the derivatives of surface displacement in three directions. Since shearography has an advantage over holography of less requirement for vibration isolation, it has an important application in the factory environment. Nakadate et al (1980) applied a digital image processing technique to measurement of surface strain and slope during vibration using shearography. Iwahashi et al (1985) introduced a single- and double-aperture method in speckle shearing interferometry for in-plane displacement measurement. Mohan and Sirohi (1996) also introduced a three-aperture configuration with various locations in speckle shearing interferometry to measure in-plane displacement. Furthermore, Pedrini et al (1996) also applied spatial carrier fringes to DSSI to extract phase information for gradient measurement. In addition, Shang et al (2000a) proposed a method to measure the profile of a 3D object using shearography technique. Shang et al (2000b) also conducted research work on the formation of shearographic carrier fringes. Hung (1982, 1998) also introduced some applications

for cracks detection using shearography.

Although DSSI is similar to ESPI, the optical setups and the measurands of both techniques are different in principle. A common schematic drawing of DSSI is shown in Fig. 2.4. As can be seen, a prism which covers half of a convex lens is used for generating a sheared image of the object at the CCD plane while the other uncovered half of the lens generates an image of the object without shearing. An interferogram is generated by the two sheared images of the object surface. The wavefront of a non-sheared image is given by

$$U_z(x, y) = a_o \exp[i\phi(x, y)] \quad (2.9)$$

where a_o denotes the amplitude and $\phi(x, y)$ represents the phase information. The wavefront of a sheared image (in the x direction with a shearing distance Δ_x) is given by

$$U_z(x + \Delta_x, y) = a_o \exp[i\phi(x + \Delta_x, y)] \quad (2.10)$$

Therefore, the wavefront from a point $Q(x, y)$ on the object surface will interfere with the wavefront from a neighbouring point $Q(x + \Delta_x, y)$ in the image plane, and thus the intensity captured by the CCD camera is given by

$$I = 2a_o^2 (1 + \cos[\phi(x + \Delta_x, y) - \phi(x, y)]) \quad (2.11)$$

After the object is deformed, another speckle pattern captured by the CCD camera is given by

$$I' = 2a_o^2 (1 + \cos[\phi(x + \Delta_x, y) - \phi(x, y) + \Delta\phi]) \quad (2.12)$$

where $\Delta\phi$ represents the phase difference introduced by the object deformation. Two speckle patterns captured before and after deformation are subtracted to produce a real time speckle fringe pattern, which is given by

$$I_s = |I - I'| = 4a_o^2 \left| \sin[\phi(x + \Delta_x, y) - \phi(x, y) + \frac{\Delta\phi}{2}] \sin(\frac{\Delta\phi}{2}) \right| \quad (2.13)$$

The relationship between the phase difference $\Delta\phi$ and the displacement derivatives can be given by (Robinson and Reid, 1993)

$$\Delta\phi = \frac{2\pi}{\lambda} \left((1 + \cos \theta_3) \frac{\partial w}{\partial x} + \sin \theta_3 \frac{\partial u}{\partial x} \right) \Delta_x \quad (2.14)$$

where $\frac{\partial w}{\partial x}$ and $\frac{\partial u}{\partial x}$ represents the displacement derivatives of w and u along the x -axis, respectively. w and u represents the displacement along the z -axis and x -axis, respectively. θ_3 represents the angle between the illumination and view direction to

the object. When θ_3 is very small, Eq. (2.14) becomes

$$\Delta\phi = \frac{4\pi}{\lambda} \frac{\partial w}{\partial x} \Delta_x \quad (2.15)$$

Therefore, the out-of-plane displacement derivative can be obtained.

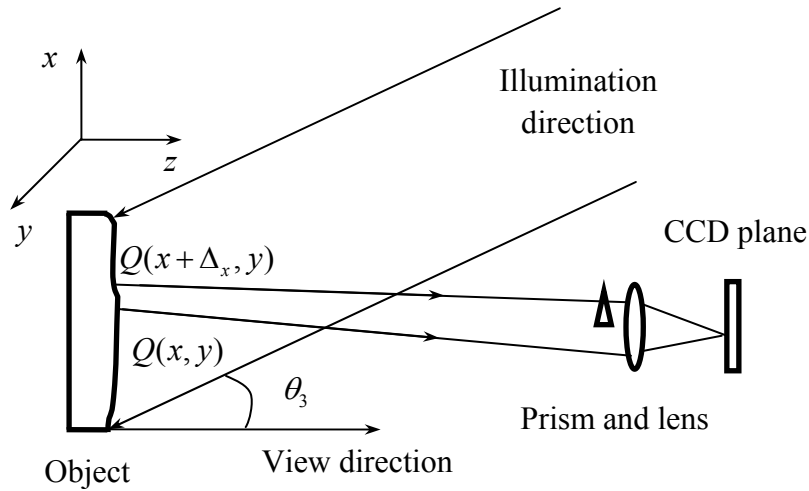


Fig. 2.4 A schematic drawing of DSSI

2.1.2.3 Multiple-wavelength interferometry

Multiple-wavelength interferometry is useful for large scale measurement due to its lower sensitivity for a longer synthetic wavelength. Multiple-wavelength interferometry includes two- and three-wavelength technique. Wyant (1971) has studied two-wavelength holography using both single and double exposure. Using the two-wavelength technique, an interferogram identical to that of a longer invisible wavelength can be obtained, and hence disadvantages of invisibility and limitations of ordinary refractive elements in using a longer wavelength in the interferometer can be

overcome. Polhemus (1973) reviewed a simplified two-wavelength technique for interferometry under static conditions and extended it to real-time dynamic testing. The phase shifting method is useful for two-wavelength interferometry and has been used to extend the phase measurement range of the single wavelength method (Cheng and Wyant, 1984). Cheng and Wyant (1985) proposed to use a three-wavelength interferometry to enhance the capability of the two-wavelength technique for surface height measurement. A better repeatability can be obtained using their method. In 1987, Creath (1987) proposed to use the two-wavelength technique for step height measurement. The variable measurement sensitivity can be obtained by changing the wavelengths. A correction of 2π ambiguities for a single wavelength phase map using a two-wavelength phase map was realized to increase the precision of the two-wavelength measurement. Furthermore, the three-wavelength technique (Wang et al, 1993) can be applied to white-light interferometry to simplify the central fringe identification, and hence the minimum requirement of signal-to-noise ratio can be reduced. In 2003, Decker et al (2003) developed a multiple-wavelength technique to perform step height measurement unambiguously with only one measurement sequence.

Multi-wavelength interferometry, also known as synthetic wavelength technique, has recently been studied since it has advantages over the single wavelength interferometry in ambiguity-free measurement (Kumar et al, 2009a; Kumar et al, 2009b). A synthetic wavelength longer than the individual wavelengths can be obtained in multi-wavelength interferometry and hence, the measurement

range is extended. The synthetic wavelength technique which has important applications in surface profile and slope measurements (Huang et al, 1997; Hack et al, 1998), does not require the conventional spatial phase unwrapping if the optical path difference of the measurands is less than the synthetic wavelength (Warnasooriya and Kim, 2009). However, a disadvantage of the synthetic wavelength technique is that the phase noise is amplified.

In two-wavelength interferometry, the phase difference of a synthetic wavelength is given by

$$\Delta\phi_s = \Delta\phi_g - \Delta\phi_r = \frac{4\pi}{\lambda_g} w - \frac{4\pi}{\lambda_r} w = \frac{4\pi}{\lambda_s} w \quad (2.16)$$

where $\Delta\phi_g$, $\Delta\phi_r$, $\Delta\phi_s$ and λ_g , λ_r , λ_s represent phase difference and wavelength of the green, red, and effective wavelength, respectively, while λ_s is given by

$$\lambda_s = \frac{\lambda_r \lambda_g}{\lambda_r - \lambda_g} \quad (2.17)$$

In multi-wavelength interferometry, the optical path for each wavelength must be the same, which means the light beams with different wavelengths should propagate in the same path.

2.1.3 Phase retrieval techniques

Phase retrieval techniques are an improvement of the fringe tracking technique. The techniques do not require tracking the intensity maxima and minima in a fringe pattern and are able to avoid the disadvantages of the fringe tracking technique (Judge and Bryanston-Cross, 1994). Phase retrieval techniques include phase shifting, Fourier transform, CWT and WFT methods.

2.1.3.1 Phase shifting techniques

Phase shifting techniques have been widely applied in many kinds of optical interferometers due to their high accuracy in phase evaluation and different phase shifting techniques have been proposed. Phase retrieval using a phase shifting algorithm normally requires at least three interferograms with different phase shifted values. The commonly used algorithms are three-step phase shifting (Huang and Zhang, 2006) and four-step phase shifting algorithm (Robinson and Reid, 1993). In 1966, Carré (1966) presented a four-step phase shifting method with a constant phase shifted value. Multiple-step phase shifting algorithms have also been reported for phase retrieval and phase shifting error reduction. In a phase shifting algorithm, the intensity I_{m_1} of an interferogram is expressed as

$$I_{m_1} = a + b \cos[\phi + (m_1 - 1)\delta_1] \quad (2.18)$$

where a and b are the background intensity and modulation factor of the

interferogram, respectively, ϕ is an unknown phase for retrieval, m_1 is the number of phase shifted frame and δ_1 is a phase shift which is achieved by moving a piezoelectric transducer (PZT). In Carré phase shifting algorithm, $m_1 = (1, 2, 3, 4)$ and the phase value ϕ is given by (Robinson and Reid, 1993)

$$\phi = \arctan\left(\frac{\tan(\delta_1 / 2) \times (I_2 - I_3 + I_1 - I_4)}{(I_2 + I_3 - I_1 - I_4)}\right) - \frac{3}{2}\delta_1 \quad (2.19)$$

where \arctan represents an arc tangent operation. The phase values retrieved from Eq. (2.19) are in the range from $-\pi$ to π and need to be unwrapped to obtain a continuous phase map.

2.1.3.2 Fourier transform method

Unlike the phase shifting technique, Fourier transform method is another important technique for phase retrieval. Takeda et al (1982) first applied Fourier transform to retrieve phase values in fringe patterns for computer-based topography. The main difference between the phase shifting and the Fourier transform method is that, for the former, at least three interferograms are needed for phase retrieval, while for the latter only one interferogram is needed. Therefore, Fourier transform method can be applied to dynamic measurement. The Fourier transform method has received more and more attention for fringe pattern analysis and Fourier transformation profilometry has also been developed for 3D non-contact profile measurement (Su and Chen, 2001).

Furthermore, not only been applied to the spatial fringe analysis, Fourier transform has also been applied to temporal phase retrieval for out-of-plane displacement measurement (Kaufmann and Galizzi, 2002; Kaufmann, 2003). Unlike the processing in the spatial domain, temporal Fourier transform is applied to process a temporal intensity signal with a cosine variation in the time domain. This technique has an advantage in avoiding the propagation of spatial unwrapping errors in dynamic displacement measurement. The principle of Fourier transform method involves transforming the fringe pattern to a frequency domain and the positive first order spectrum is used in an inverse Fourier transform for phase retrieval. This technique requires the positive first order spectrum which must be separable from the zero order and negative first order spectrum. The Fourier transform is defined as

$$F(\omega) = \int_{-\infty}^{+\infty} f_{1d}(x) e^{-i\omega x} dx \quad (2.20)$$

where ω represents an angular frequency coordinate in the x direction, while $f_{1d}(x)$ is a periodic signal and $F(\omega)$ is its spectrum. An Inverse Fourier transform is used to reconstruct the original signal and is defined as

$$f_{1d}(x) = \frac{1}{2\pi} \int_{-\infty}^{+\infty} F(\omega) e^{i\omega x} d\omega \quad (2.21)$$

To make Fourier transform applicable in fringe analysis, a carrier is generally required in a fringe pattern (Takeda et al, 1982). The intensity of a fringe pattern with

a carrier is given by

$$I(x, y) = a(x, y) + c(x, y) \exp(i2\pi fx) + c^*(x, y) \exp(-i2\pi fx) \quad (2.22)$$

where

$$c(x, y) = \frac{1}{2} b(x, y) \exp[i\phi(x, y)] \quad (2.23)$$

where f is the carrier frequency introduced in the x direction. $a(x, y)$, $b(x, y)$ and $\phi(x, y)$ are the background intensity, modulation factor and phase of the fringe pattern, respectively, and they vary slowly compared with the variation introduced by the spatial carrier frequency. Generally, $a(x, y)$ and $b(x, y)$ can be assumed as constants. A Fourier transform with respect to x is performed on Eq. (2.22), which gives

$$\hat{I}(\omega, y) = A(\omega, y) + C(\omega - 2\pi f, y) + C^*(\omega + 2\pi f, y) \quad (2.24)$$

where \hat{I} , A , C and C^* represent a 1D Fourier transform of the corresponding terms in Eq. (2.22). The carrier frequency must be able to separate the spectrum of the three terms in Eq. (2.24) and the second term $C(\omega - 2\pi f, y)$ is selected using a filtering technique. An inverse Fourier transform is applied on the selected spectrum, which gives $c(x, y) \exp(i2\pi fx)$. The phase information is given by

$$\begin{aligned}
2\pi fx + \phi(x, y) &= \text{angle}(c(x, y) \exp(i2\pi fx)) \\
&= \text{angle}\left(\frac{1}{2} b(x, y) \exp(i[2\pi fx + \phi(x, y)])\right)
\end{aligned} \tag{2.25}$$

where *angle* indicates taking the argument of the complex function.

Figure 2.5 shows the process of phase retrieval of a 1D signal fringe pattern using Fourier transform method. Figure 2.5(a) shows a simulated cosine signal with a normally distributed random noise whose variance is 0.2. Figure 2.5(b) shows its Fourier spectrum and Fig. 2.5(c) shows a selected positive first order spectrum. Figure 2.5(d) shows the phase information of the selected positive first order spectrum retrieved using an inverse Fourier transform. The wrapped phase values need to be unwrapped since they are in modulus of 2π . Figure 2.5(e) shows the unwrapped phase values which have been shifted by a specific value and the theoretical phase values. Due to the poor noise filtering capability, fluctuations in the wrapped and unwrapped phase values are observed in Figs. 2.5(d) and 2.5(e), respectively. In addition, the Fourier transform is unable to provide the instantaneous frequency of a signal, and hence more advanced methods are required to reduce the errors caused by noise. Time-frequency analysis techniques such as CWT and WFT, which are based on Fourier transform, with a better noise reduction capability for phase retrieval are discussed in the following sections.

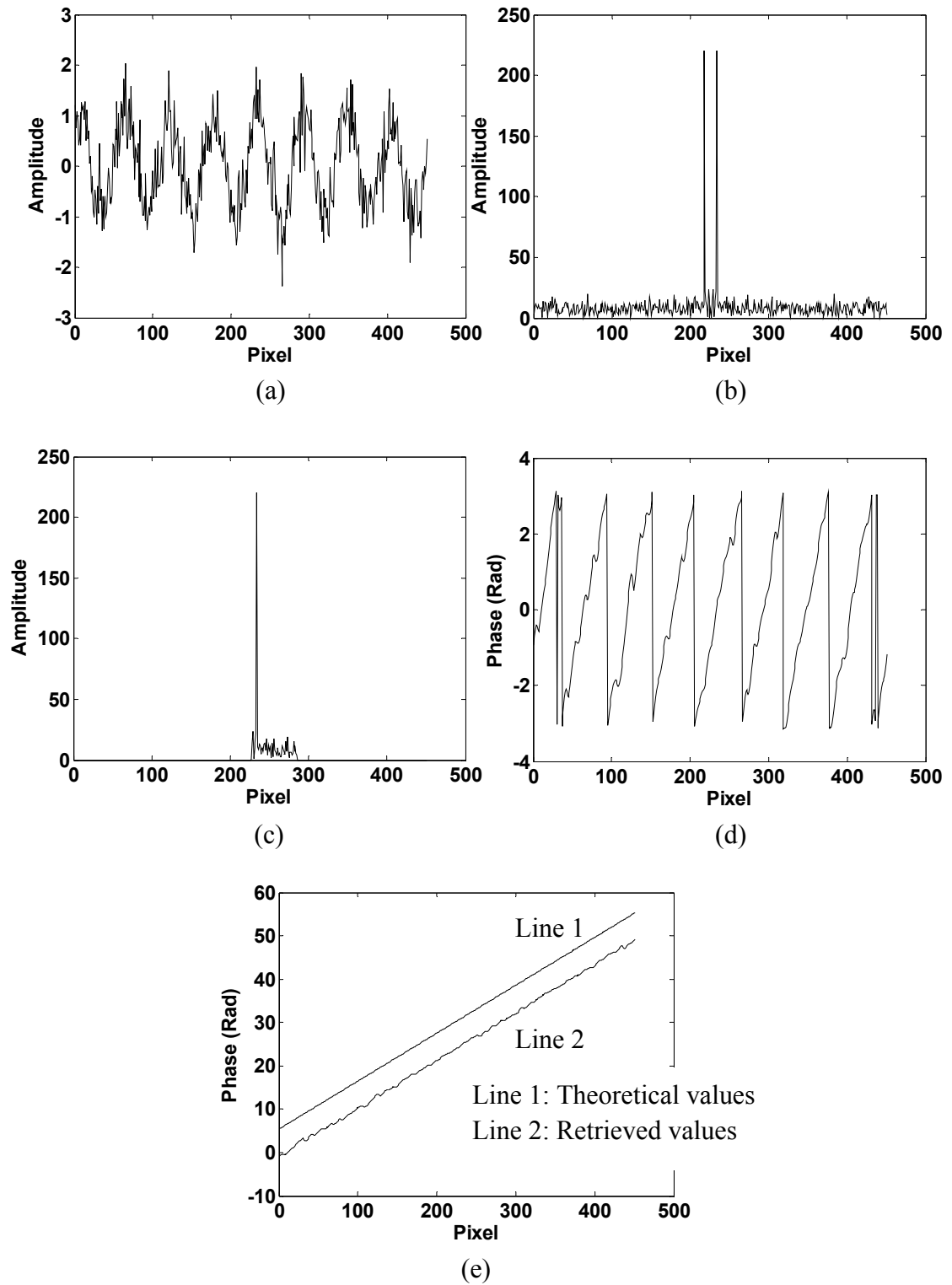


Fig. 2.5 (a) A simulated intensity signal with a normally distributed random noise; (b) Fourier spectrum of the signal; (c) selected positive first order spectrum from (b); (d) retrieved wrapped phase; (e) unwrapped phase

2.2 Continuous wavelet transform (CWT) in optical measurement

The Fourier transform has the advantage that only one fringe pattern is required for phase retrieval so that it has the potential for dynamic deformation measurement. However, The Fourier transform is a global transform of a signal and therefore, signal values at different points will affect each other in the processing and thus is non-robust in noise reduction.

Unlike the Fourier transform method, CWT is a local transform with different resolution for a signal. Therefore, CWT acts as a filter during processing and has a better noise reduction capability than Fourier transform method (Zhong and Weng, 2005; Huang et al, 2010). Continuous wavelet transform can provide space-frequency information synchronously while Fourier transform does not. One-dimensional continuous wavelet transform has been widely applied to fringe analysis in optical measurement. In 1997, Watkins et al (1997) first used CWT to accurately reconstruct surface profiles from interferograms and compared CWT to the standard phase-stepping method. Later, Watkins et al (1999) applied CWT to directly extract phase gradients from a fringe pattern. Continuous wavelet transform of a fringe pattern is able to produce the maximum modulus of wavelet transform when a daughter wavelet is most similar to a signal in a local area. Using this method, the phase gradient of a fringe pattern can be found and integration of the gradient will produce the phase information. This will avoid the need for phase unwrapping. Federico and Kaufmann (2002) applied 1D CWT method to the fringe patterns of ESPI. However this method produces noisy phase maps if the signal to noise ratio is low and the method is not

suitable for analyzing fringe patterns with horizontal and vertical spatial carriers. Dursun et al (2004) applied Morlet wavelet to determine the phase distribution of fringes for 3D profile measurement using a fringe projection technique. Zhong and Weng (2004a) used CWT to retrieve the phase of the spatial carrier-fringe pattern for 3D shape measurement and overcome the limitation of Fourier transform. Watkins (2007) also proposed a theory of the maximum modulus of a wavelet ridge for the retrieval of an instantaneous fringe frequency, while Afifi et al (2002) employed another wavelet, Paul wavelet, for phase retrieval from a single fringe pattern without using phase unwrapping. The theoretical analysis of Paul wavelet algorithm was also presented.

In addition to 1D CWT, 2D CWT has also received much attention for phase retrieval. Compared to 1D CWT, 2D CWT has a rotation parameter in addition to the scale parameter. The 1D CWT is able to retrieve phase values correctly from a fringe pattern with high signal to noise ratio. For a noisy fringe pattern (for example, a fringe pattern with speckle noise), 1D CWT will produce a noisy wrapped phase map which will affect the success rate of the phase unwrapping algorithms and may fail to produce a continuous phase map. It is unable to obtain the correct integral multiples of 2π for the wrapped phase map in this case. Furthermore, 1D CWT is not suitable for analyzing a fringe pattern with spatial frequencies in the vertical and horizontal directions, while the 2D CWT is suitable since processing is in two dimensions. Kadooka et al (2003) first employed 2D CWT for analyzing a moiré interference fringe pattern. This technique overcame the difficulty of phase retrieval encountered

by the Fourier transform method. In 2006, Gdeisat et al (2006) proposed to use a 2D fan CWT algorithm to demodulate phase values from a noisy fringe pattern. Compared to the 1D CWT, the 2D fan CWT algorithm showed an improvement of noise reduction. However, there were still fluctuations affected by noise in the phase map and the method failed to show correct phase values from some speckle fringe patterns due to the narrow bandwidth of the 2D fan wavelet. In 2006, Wang and Ma (2006) also proposed an advanced CWT algorithm for phase retrieval from a fringe pattern using microscopic moiré interferometry. This method produces better results than the 1D CWT.

Two approaches, namely phase estimation from wavelet coefficients and frequency estimation from the ridge of wavelet transform are used for phase retrieval. In the former case, the CWT is used to calculate the correlation between the fringe pattern and the wavelet functions with different scale parameters. When the wavelet function is most similar to the signal in a local area of the fringe pattern, the modulus of the wavelet transform coefficient will reach a maximum value. The phase information can thus be retrieved from the real and imaginary part of the wavelet transform coefficient when its modulus reaches a maximum value. Phase retrieval from the former approach is more accurate, but phase unwrapping is required to remove 2π jumps in a wrapped phase map. For the latter approach, since phase is retrieved from integration of an instantaneous frequency of the fringe pattern, phase unwrapping is avoided. However, the accuracy of this technique depends on the scale resolution. A high scale resolution will increase the computation time. Furthermore,

integration of the instantaneous frequency will propagate phase error from one pixel to its adjacent pixel. Therefore, the former approach is more commonly used.

Complex wavelet such as Morlet wavelet is commonly used in optical measurement for phase retrieval. Figure 2.6(a) shows a plot of a 1D Morlet wavelet and its spectrum. The scale of the Morlet wavelet is 1 and ω_0 is 2π . The upper half of Fig. 2.6(a) shows the real and imaginary parts of the Morlet wavelet which are represented by the solid and dash lines, respectively. The lower half shows its Fourier spectrum. Since a complex Morlet wavelet contains the phase information in its real and imaginary parts, it is used for phase retrieval of the signal from their similarity. The 1D CWT of a signal is defined as (Mallat, 2001; Zhong and Weng, 2005; Watkins, 2007)

$$Wf(q, m) = |q|^{-\frac{1}{2}} \int_{-\infty}^{+\infty} f_{1d}(x) \psi^*\left(\frac{x-m}{q}\right) dx \quad (2.26)$$

where $f_{1d}(x)$ represents a signal and the symbol $*$ represents complex conjugation.

$\psi\left(\frac{x-m}{q}\right)$ denotes a wavelet function with translation on the x -axis by m and

dilation by scale q ($q > 0$) of the mother wavelet $\psi(x)$, which is usually a complex

Morlet wavelet function given by

$$\psi(x) = \pi^{-\frac{1}{4}} \exp\left(-\frac{x^2}{2}\right) \exp(i\omega_0 x) \quad (2.27)$$

where ω_0 is a fixed frequency and can be set as 2π to meet the admissibility condition. As can be seen, the coefficients $Wf(q, m)$ of wavelet transform is able to provide spatial and frequency information simultaneously. A wavelet ridge is a path that follows the maximum values of $|Wf(q, m)|$ from which the phase and instantaneous frequency can be obtained. To use a 1D CWT for phase retrieval from a fringe pattern, the 1D signal of a fringe pattern described by Eq. (2.22) is given by

$$I(x) = a + \frac{1}{2}b \exp(i[\phi(x) + 2\pi fx]) + \frac{1}{2}b \exp(-i[\phi(x) + 2\pi fx]) \quad (2.28)$$

where the background intensity a and the modulation factor b are considered as constants. Assuming that the 1D intensity signal has a linear phase change, which can be easily achieved in the experiment, the phase term may be expanded using Taylor series of the first order and given by

$$\phi(x) = \phi(m) + \phi'(m)(x - m) \quad (2.29)$$

hence the 1D CWT of Eq. (2.28) is given by

$$\begin{aligned} Wf(q, m) &= q^{-\frac{1}{2}} \int_{-\infty}^{+\infty} I(x) \psi^*\left(\frac{x-m}{q}\right) dx \\ &= Wf_1(q, m) + Wf_2(q, m) + Wf_3(q, m) \end{aligned} \quad (2.30)$$

where

$$\begin{aligned}
Wf_1(q, m) &= \sqrt{2qa}\pi^{\frac{1}{4}} \exp\left(-\frac{\omega_0^2}{2}\right) \\
Wf_2(q, m) &= \sqrt{\frac{q}{2}}b\pi^{\frac{1}{4}} \exp\left(i[\phi(m) + 2\pi fm]\right) \exp\left(-\frac{(\omega_0 - [2\pi f + \phi'(m)]q)^2}{2}\right) \\
Wf_3(q, m) &= \sqrt{\frac{q}{2}}b\pi^{\frac{1}{4}} \exp\left(-i[\phi(m) + 2\pi fm]\right) \exp\left(-\frac{(\omega_0 + [2\pi f + \phi'(m)]q)^2}{2}\right)
\end{aligned} \tag{2.31}$$

From Eq. (2.31) it can be seen that when the scale parameter q of the CWT satisfies the following equation

$$q = \frac{\omega_0}{2\pi f + \phi'(m)} \tag{2.32}$$

the modulus of CWT becomes

$$|Wf(q, m)| \approx |Wf_2(q, m)| \tag{2.33}$$

since $|Wf_1(q, m)| \approx 0$ and $|Wf_3(q, m)| \approx 0$. The normalized scalogram represented by

$\frac{|Wf(q, m)|^2}{q}$ will yield a maximum value. For phase retrieval, the maximum value of

$|Wf(q, m)|$ is used to determine the wavelet ridge. Therefore, instantaneous frequency

of the fringe pattern can be retrieved from Eq. (2.32). Furthermore, phase information

can be retrieved from $Wf_2(q, m)$ which is given by

$$\phi(m) + 2\pi fm = \arctan\left(\frac{\text{Im}(Wf(q, m))}{\text{Re}(Wf(q, m))}\right) \quad (2.34)$$

where Im represents the imaginary part of $Wf(q, m)$, Re represents the real part of $Wf(q, m)$. As can be seen from Fig. 2.6(b), a scalogram of $|Wf(q, m)|$ for the signal shown in Fig. 2.5(a) can be obtained. The dash line represents the ridge of CWT. As can be seen from this scalogram, both spatial and frequency information of the signal can be obtained from CWT. Therefore, CWT has the advantage over Fourier transform which can only provide the frequency information of the signal. Figure 2.6(c) shows the unwrapped phase using CWT. The top line shows the theoretical phase values and the bottom line shows the phase values obtained from Eq. (2.34) after unwrapping. For clarity, the calculated phase values are shifted by a certain offset. As can be seen, the retrieved phase values closely approximate to the theoretical values. The noise of an intensity signal is suppressed using the 1D CWT and the result obtained is smoother than that of the Fourier transform. The reason is that the modulus of the wavelet transform coefficient of the noise is less than that of the signal and can be suppressed during the processing.

Two-dimensional wavelet transform has also been proposed for phase retrieval from a fringe pattern in 3D profile measurement. The processing is in two dimensions and the theory is presented in detail in Chapter three.

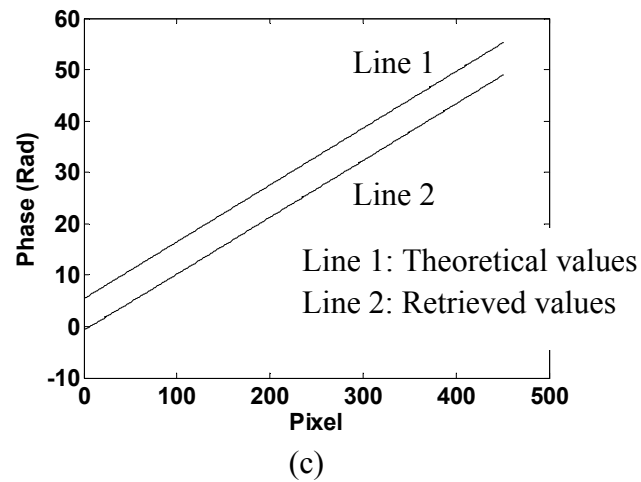
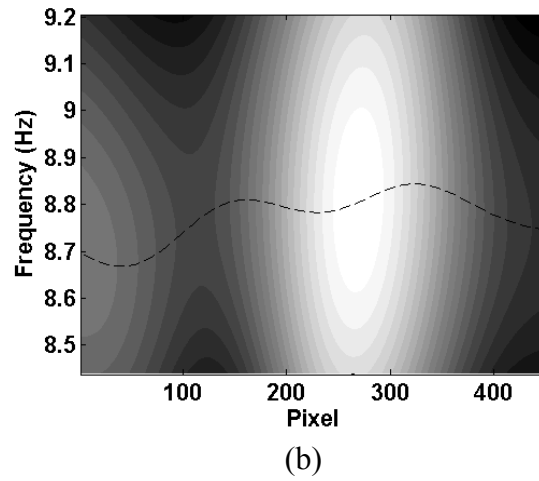
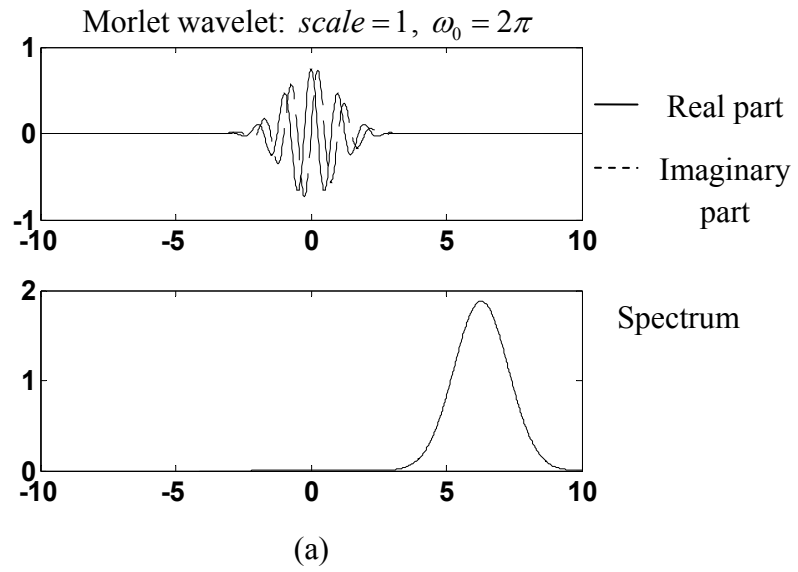


Fig. 2.6 (a) A 1D Morlet wavelet and its spectrum; (b) a scalogram of $|Wf(q, m)|$ for the signal shown in Fig. 2.5(a) and the dash line represents the ridge of CWT; (c) unwrapped phase using CWT

2.3 Windowed Fourier transform (WFT) in optical measurement

Unlike CWT, which has a variable resolution for time-frequency analysis, WFT has a fixed resolution in both time and frequency domain during processing once a window size is selected, according to the uncertainty principle. Figure 2.7 shows different basis for different time-frequency transform. As can be seen, for different frequencies, the Fourier basis is always continuous which means it is a transform for a global signal, while the wavelet basis is dilated or compressed with different resolutions in both time and frequency domain and the transform is applied on a local signal within a window. As for the WFT, the transform has a fixed resolution for all the frequency components and it is also a transform of a local signal within a window.

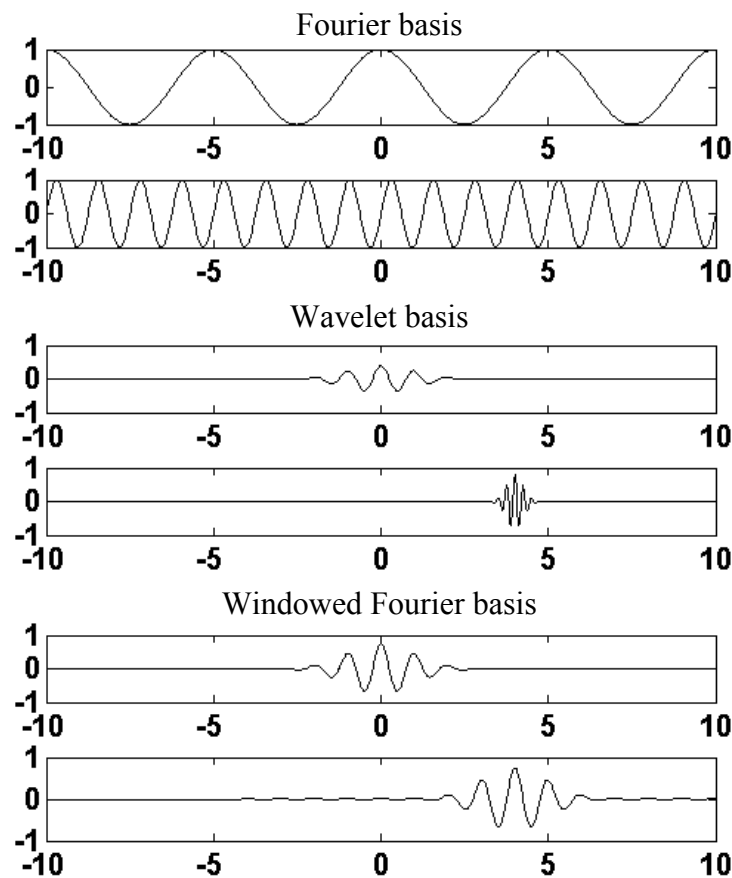


Fig. 2.7 Basis of transform for time-frequency analysis

In 2002, Wang and Asundi (2002) applied the Gabor filter for strain contouring and employed the theory of WFT for phase retrieval. In addition, Qian (2004, 2007b) proposed WFT and 2D WFT as an alternative method for phase retrieval and fringe demodulation and obtained satisfactory results. However, the algorithm was employed using the convolution theory which resulted in a long computational time. Other researchers such as Zhong and Weng (2004b) have proposed a dilating Gabor transform for 3D shape measurement. Multi-scale WFT for phase extraction was also proposed by Zhong and Zeng (2007). An adaptive WFT for 3D shape measurement was also proposed by Zheng et al (2006). Gao et al (2009) employed a real-time 2D parallel system for WFT to show the potential of WFT for real-time phase retrieval.

Similar to CWT, phase can also be retrieved from either coefficient or instantaneous frequency of WFT. However, phase retrieved from the integration of instantaneous frequency, namely phase derivative, normally results in a larger error compared with the phase retrieved from the coefficient of WFT. In WFT, there are two most frequently used methods called WFF method and windowed Fourier ridges method (Qian, 2004; Qian, 2007b). Both methods can be applied to a fringe pattern with speckle noise for noise reduction and phase retrieval. Using WFT for fringe demodulation, both spatial and frequency information can be simultaneously obtained and the parameters of WFT should also be correctly selected.

The 1D WFT and 1D inverse WFT of Eq. (2.28) are given by

$$Sf(m, \varepsilon) = \int_{-\infty}^{+\infty} I(x)g(x-m)\exp(-i\varepsilon x)dx \quad (2.35)$$

$$I(x) = \frac{1}{2\pi} \int_{-\infty}^{+\infty} \int_{-\infty}^{+\infty} Sf(m, \varepsilon)g(x-m)\exp(i\varepsilon x)d\varepsilon dm \quad (2.36)$$

where $Sf(m, \varepsilon)$ represents WFT of the 1D signal and $g(x-m)$ denotes a shifted window function $g(x)$ in the x -axis, which is given by

$$g(x) = \exp\left(-\frac{x^2}{2\sigma^2}\right) \quad (2.37)$$

where σ is a parameter of the Gaussian window size. Substitute the second term of Eq. (2.28) into Eq. (2.35) gives

$$Sf_2(m, \varepsilon) = \frac{b}{2} \exp(i[\phi(m) + 2\pi fm - \varepsilon m]) \int_{-\infty}^{+\infty} g(x) \exp(-i[\varepsilon - \phi'(m) - 2\pi f]x)dx \quad (2.38)$$

Since the Fourier spectrum of a Gaussian function is still a Gaussian function, Eq. (2.38) can be rewritten as

$$Sf_2(m, \varepsilon) = \frac{b}{2} \exp(i[\phi(m) + 2\pi fm - \varepsilon m]) \hat{G}(\varepsilon - \phi'(m) - 2\pi f) \quad (2.39)$$

where $\hat{G}(\omega)$ represents the Fourier spectrum of $g(x)$. When the following condition is satisfied

$$\varepsilon = \phi'(m) + 2\pi f \quad (2.40)$$

the WFT modulus $|Sf(m, \varepsilon)|$ of Eq. (2.28) can be approximated as $|Sf_2(m, \varepsilon)|$, since the WFT modulus of the first and third term of Eq. (2.28) are approximate to zero. The WFT modulus $|Sf(m, \varepsilon)|$ will reach the maximum value when Eq. (2.40) is satisfied. Therefore, the filtered phase information is retrieved as

$$\overline{\phi(m) + 2\pi fm} = \text{angle}(\exp(i\varepsilon m) Sf_2(m, \varepsilon)) \quad (2.41)$$

where symbol ‘ $-$ ’ represents a filtering operation. This method is the windowed Fourier ridges method for phase retrieval. Another method, WFF can also be used for phase retrieval and is given by

$$\overline{I(x)} = \frac{1}{2\pi} \int_{\varepsilon l}^{\varepsilon h} \overline{[I(x) \otimes D(x, \varepsilon)]} \otimes D(x, \varepsilon) d\varepsilon \quad (2.42)$$

where

$$D(x, \varepsilon) = g(x) \exp(i\varepsilon x) \quad (2.43)$$

Symbol \otimes represents a convolution operation and $\overline{[I(x) \otimes D(x, \varepsilon)]}$ denotes the filtered value of $I(x) \otimes D(x, \varepsilon)$ using a threshold value, while $\overline{I(x)}$ denotes the filtered value of $I(x)$ with integration limits from εl to εh . The filtered phase value

can be retrieved using

$$\overline{\phi(x) + 2\pi fx} = \text{angle}(\overline{I(x)}) \quad (2.44)$$

Similar to CWT, the windowed Fourier ridges method is able to retrieve the instantaneous frequencies of a fringe pattern and provide phase information without phase unwrapping by integration of the instantaneous frequencies. However, this approach also has a limitation as the accuracy of the retrieved phase is restricted by the integration step and phase values retrieved from instantaneous frequencies normally incur a large error. In addition, the phase values can be directly retrieved from the coefficients of the windowed Fourier ridges and this approach is more accurate than the integration of the instantaneous frequencies. Besides, the WFF method is also an important method of WFT for phase retrieval. The principle of WFF is similar to the filtering using Fourier transform. The intensity of a fringe pattern is transform to a windowed Fourier domain and a threshold is used to filter the windowed Fourier spectrum. Then the filtered spectrum is transformed back using an inverse WFT and the filtered phase information can be retrieved by taking the argument of the result.

Two-dimensional windowed Fourier transform which has the advantages over 1D CWT and 1D WFT for fringe demodulation because the processing is in both the x and y directions of a fringe pattern has received more attention recently. It is suitable for phase retrieval since fringe patterns normally have variations in both the

x and y directions. Since WFT is a local transform of a signal, the advantage is that signals within the window will not be affected by other signals outside the window. Therefore, WFT has been widely applied in fringe demodulation obtained from interferometry. Moreover, unlike CWT, the temporal and frequency resolution of WFT is always the same during processing once the window size is selected and the resolution can be selected according to the spectrum of a fringe pattern even at very low frequencies. In CWT, the resolution at very low frequencies is very high which means the wavelet window in frequency domain is very narrow around that frequency, it will not be possible to acquire enough information for phase retrieval at the low frequency and may result in failure for phase retrieval. Moreover, a large wavelet scale is required for low frequency and this will incur a large amount of processing time for a wide scale range. Therefore, CWT is not suitable for demodulation of low frequency fringe patterns. Previous WFT method using convolution algorithm requires a large amount of computation time due to the integration step and window size. This is a limitation of the WFT and therefore, the present study is focused on improving its computation efficiency.

CHAPTER THREE

DEVELOPMENT OF THEORY

This chapter focuses on the theoretical development of the proposed optical phase retrieval algorithms. The first section covers theoretical development of 2D Gabor CWT. Limitations of previous 2D CWT are discussed. Previous 2D fan CWT is compared and the advantage of the proposed wavelet transform algorithm is discussed. In the second section, an improved WFT algorithm is proposed for phase retrieval and noise reduction of a speckle fringe pattern. Limitations of the WFT with convolution algorithm are emphasized. The Gerchberg extrapolation method is used to suppress the boundary effect. The last section is devoted to phase fringe denoising using the WFF method. A single wavelength DSSI based on WFF and a two-wavelength DSSI based on sine-cosine filtering are compared. A two-wavelength technique with a combined filtering method for phase retrieval in DSSI is also proposed. The method exploits the advantages of a two-wavelength technique as an alternative to phase unwrapping.

3.1 Two-dimensional (2D) CWT for phase retrieval

Two-dimensional continuous wavelet transform has been applied to digital image analysis (Antoine et al, 1993). Since an interference pattern can be presented in a digital format, digital image processing techniques, such as 2D CWT, can be

employed for fringe demodulation. The 2D CWT of a fringe pattern $I(\mathbf{X})$ with respect to a 2D wavelet $\psi(\mathbf{X})$ is given by (Wang and Ma, 2006; Antoine et al, 1993)

$$WT(q, \mathbf{b}_t, \theta) = q^{-2} \int d^2 \mathbf{X} \psi^*[q^{-1} r_{-\theta}(\mathbf{X} - \mathbf{b}_t)] I(\mathbf{X}) \quad (3.1)$$

where the symbol “*” represents an operation of complex conjugate, $\mathbf{X} = (x, y)$ represents the spatial coordinates of the fringe pattern, $\mathbf{b}_t = (b_x, b_y)$ denotes a translation parameter along two coordinate axes, q is a scale dilation parameter, $r_{-\theta}$ is a rotation matrix of size 2×2 and θ is a rotation angle. The rotation matrix $r_{-\theta}$ which acts on $\mathbf{X} = (x, y)$ is given by

$$r_{-\theta} \mathbf{X} = (x \cos \theta + y \sin \theta, -x \sin \theta + y \cos \theta) \quad (3.2)$$

In addition, the 2D CWT can also be defined in the frequency domain as

$$WT(q, \mathbf{b}_t, \theta) = \int d^2 \mathbf{K} \exp(i \mathbf{b}_t \cdot \mathbf{K}) \hat{\psi}^*(q r_{-\theta} \mathbf{K}) \hat{I}(\mathbf{K}) \quad (3.3)$$

where $\mathbf{K} = (\omega_x, \omega_y)$ denotes the frequency coordinates, $\mathbf{b}_t \cdot \mathbf{K} = b_x \omega_x + b_y \omega_y$ is an Euclidean scalar product, and “ \wedge ” denotes a Fourier spectrum. Using Eq. (3.3), the computation efficiency can be improved significantly since fast Fourier transform is introduced.

3.1.1 Limitations of previous 2D CWT

In fringe pattern analysis, a commonly used mother wavelet for phase retrieval and fringe filtering is a complex Morlet wavelet. In fact, the complex Morlet wavelet is a special case of a complex Gabor wavelet. Figure 3.1 shows a 2D complex Morlet wavelet. The real part, imaginary part and Fourier spectrum of the 2D complex Morlet wavelet with a rotation angle $\theta = -\frac{\pi}{2}$ are shown in Figs. 3.1(a), 3.1(b) and 3.1(c), respectively.

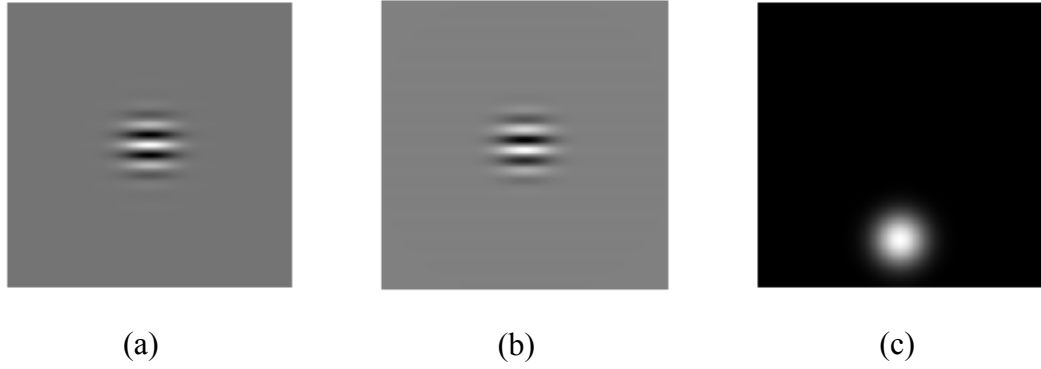


Fig. 3.1 (a) Real part of a 2D Morlet wavelet; (b) imaginary part of a 2D Morlet wavelet; (c) Fourier spectrum of a 2D Morlet wavelet

The mathematical expression of 2D Morlet wavelet is given by

$$\psi_M(\mathbf{X}) = \exp(i\mathbf{K}_\theta \cdot \mathbf{X}) \exp\left(-\frac{1}{2}|\mathbf{X}|^2\right) \quad (3.4)$$

where $\mathbf{K}_\theta = (k_0, 0)$ is the central frequency of a 2D Morlet wavelet, and therefore

$\mathbf{K}_\theta \cdot \mathbf{X} = k_0 x$. As can be seen, the complex Morlet wavelet has a Gaussian envelop.

The real and imaginary parts vary in the form of a cosine and sine function, respectively. Therefore, the complex Morlet wavelet can be used to analyze the fringe variation for phase retrieval. However, in CWT, the frequency resolution for a low frequency component is very high and would result in a narrow frequency window, while for a high frequency component it would result in a wide frequency window. Therefore, the 2D complex Morlet wavelet has a narrow spectrum for a low frequency component (Gdeisat et al, 2006; Kadooka et al, 2003). It is only suitable for phase retrieval from a fringe pattern with a narrow bandwidth and will fail to demodulate fringe patterns with wide bandwidths in the spectrum.

Besides the 2D complex Morlet wavelet, 2D fan CWT has also been used for fringe analysis (Gdeisat et al, 2006). A 2D fan wavelet is constructed by superposing a number of complex Morlet wavelets. Similar to the 2D complex Morlet wavelet, it fails to demodulate fringe patterns with a wide bandwidth and high speckle noise. To overcome this problem, one possible solution is to introduce a window extension parameter σ in a 2D fan wavelet. An advanced 2D fan wavelet with a rotation angle θ is given by

$$\psi_{Fan}(r_{-\theta}\mathbf{X}) = \sum_{t=0}^{N-1} \exp \left\{ -\frac{1}{2\sigma^2} (x^2 + y^2) + ik_0 [x \cos(\theta_t + \theta) + y \sin(\theta_t + \theta)] \right\} \quad (3.5)$$

The Fourier transform of $\psi_{Fan}(r_{-\theta}\mathbf{X})$ is given by

$$\hat{\psi}_{Fan}(r_{-\theta}\mathbf{K}) = \sum_{t=0}^{N-1} \exp \left\{ -\frac{1}{2} \sigma^2 \left([\omega_x - k_0 \cos(\theta_t + \theta)]^2 + [\omega_y - k_0 \sin(\theta_t + \theta)]^2 \right) \right\} \quad (3.6)$$

where $\theta_t = t\Delta$, $\Delta = 30^\circ$ and $N=6$ is the number of superposed Morlet wavelets (Kirby, 2005). Figure 3.2 shows a 2D fan wavelet. The real part, imaginary part and Fourier spectrum of the 2D fan wavelet with a rotation angle $\theta = -\frac{\pi}{3}$ are shown in Figs. 3.2(a), 3.2(b) and 3.2(c), respectively. As can be seen from the spectrum, there are six bumps which represent six Morlet wavelets.

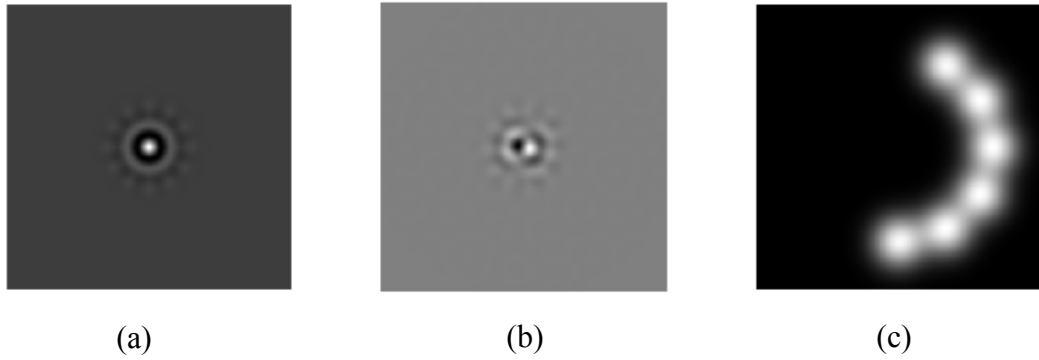


Fig. 3.2 (a) Real part of a 2D fan wavelet; (b) imaginary part of a 2D fan wavelet; (c) Fourier spectrum of a 2D fan wavelet

With an advanced 2D fan wavelet, the frequency window for processing the low frequency components can be enlarged, however, because of the superposition of several complex Morlet wavelets, the spectrum in the frequency domain is wider and thus results in more spatial noise which will degrade the retrieved phase.

3.1.2 Advanced 2D Gabor CWT

To overcome this problem, a suitable wavelet function should be selected. A 2D complex Gabor wavelet can be used since it has a controllable Gaussian window in both the spatial and frequency domains. This character makes its frequency resolution for the low frequency components adjustable using a parameter for window size control. A 2D complex Gabor wavelet is given by

$$\psi_G(\mathbf{X}) = \exp(i\mathbf{K}_0 \cdot \mathbf{X}) \exp\left(-\frac{1}{2\sigma^2}|\mathbf{X}|^2\right) \quad (3.7)$$

where σ is a parameter for controlling the window size. σ is 0.5 (Wang and Ma, 2006) and k_0 is 5.336 (Gdeisat et al, 2006) in this study. k_0 and σ are able to control the window size in both the spatial and frequency domain. The parameter k_0 controls the central frequency and σ determines the window size at that frequency. The Fourier transform of 2D Gabor wavelet is given by

$$\hat{\psi}_G(\mathbf{K}) = \exp\left(-\frac{\sigma^2}{2}|\mathbf{K} - \mathbf{K}_0|^2\right) \quad (3.8)$$

The 2D Gabor wavelet shows similar images with those of the 2D Morlet wavelet shown in Fig. 3.1. Unlike the 2D Morlet wavelet, the 2D Gabor wavelet is suitable for analyzing a fringe pattern with a narrow or wide bandwidth in the frequency domain. This is because the window size of a 2D Gabor wavelet for a low frequency

component can be extended using the parameter σ . Thus more useful information can be obtained since the low frequency region contains most of the energy of the signal. A suitable value of σ should be selected to obtain useful information and reduce the spatial noise in a noisy fringe pattern. The 2D Gabor wavelet $\psi_G^*[q^{-1}r_{-\theta}(\mathbf{X} - \mathbf{b}_t)]$ with a translation parameter \mathbf{b}_t , a dilation parameter q ($q > 0$) and a rotation angle θ is given by

$$\psi_G^*[q^{-1}r_{-\theta}(\mathbf{X} - \mathbf{b}_t)] = \exp \left\{ -\frac{1}{2\sigma^2} \frac{[(x-b_x)^2 + (y-b_y)^2]}{q^2} - ik_0 \frac{[(x-b_x)\cos\theta + (y-b_y)\sin\theta]}{q} \right\} \quad (3.9)$$

hence $\hat{\psi}_G^*(qr_{-\theta}\mathbf{K})$ is given as

$$\hat{\psi}_G^*(qr_{-\theta}\mathbf{K}) = \exp \left\{ -\frac{1}{2}\sigma^2 [(q\omega_x - k_0 \cos\theta)^2 + (q\omega_y - k_0 \sin\theta)^2] \right\} \quad (3.10)$$

The following section discusses the use of 2D Gabor CWT for phase retrieval from a speckle fringe pattern with a spatial carrier. A local speckle fringe pattern with a spatial carrier is given by (Wang and Ma, 2006)

$$I^l(\mathbf{X}) = I_{l0} + I_{l1} \cos \left[2\pi \frac{(x-b_x)\cos\phi + (y-b_y)\sin\phi}{P} + \phi \right] \quad (3.11)$$

where b_x and b_y denote translation parameters of \mathbf{b}_t in the fringe pattern, P is a local fringe period, φ is a local fringe direction, ϕ is an unknown phase to be retrieved, I_{l0} and I_{l1} considered as constants are background intensity and modulation factor, respectively. The Fourier spectrum of Eq. (3.11) is given by

$$\begin{aligned}
 F[I^l(\mathbf{X})] = & 4I_{l0}\pi^2\delta(\omega_x, \omega_y) \\
 & + 2I_{l1}\pi^2\exp(i\phi)\exp\left[-i\frac{2\pi}{P}(b_x\cos\varphi + b_y\sin\varphi)\right] \\
 & \times \delta\left(\omega_x - \frac{2\pi}{P}\cos\varphi, \omega_y - \frac{2\pi}{P}\sin\varphi\right) \\
 & + 2I_{l1}\pi^2\exp(-i\phi)\exp\left[i\frac{2\pi}{P}(b_x\cos\varphi + b_y\sin\varphi)\right] \\
 & \times \delta\left(\omega_x + \frac{2\pi}{P}\cos\varphi, \omega_y + \frac{2\pi}{P}\sin\varphi\right)
 \end{aligned} \tag{3.12}$$

where F denotes the Fourier transform, δ is the Dirac function. In Eq. (3.12) the direct current term (zero-frequency term) and two side-frequency components are separated by the carrier. Therefore, the direct current term and the left side-frequency component in the frequency domain are first removed for phase extraction to remove their interference. Eq. (3.12) then becomes

$$\begin{aligned}
 F_{\text{removed}}[I^l(\mathbf{X})] = & 2I_{l1}\pi^2\exp(i\phi)\exp\left[-i\frac{2\pi}{P}(b_x\cos\varphi + b_y\sin\varphi)\right] \\
 & \times \delta\left(\omega_x - \frac{2\pi}{P}\cos\varphi, \omega_y - \frac{2\pi}{P}\sin\varphi\right)
 \end{aligned} \tag{3.13}$$

The 2D Gabor CWT is then employed to process the right side-frequency component.

Substitute Eq. (3.10) and Eq. (3.13) into Eq. (3.3), the 2D Gabor CWT becomes

$$WT^l(q, \mathbf{b}_t, \theta) = 2I_{l1}\pi^2 \exp(i\phi) \times \exp \left\{ -\frac{1}{2} \sigma^2 \left[\left(\frac{2\pi}{P} q \cos \varphi - k_0 \cos \theta \right)^2 + \left(\frac{2\pi}{P} q \sin \varphi - k_0 \sin \theta \right)^2 \right] \right\} \quad (3.14)$$

where $WT(q, \mathbf{b}_t, \theta) = WT^l(q, \mathbf{b}_t, \theta)$ denotes the wavelet transform of the whole fringe pattern for a translation \mathbf{b}_t . This is equivalent to the wavelet transform of the local fringe pattern for a translation \mathbf{b}_t . In Eq. (3.12), a rectangular window is employed to select the second term from the spectrum of the fringe pattern and an inverse Fourier transform is performed. The phase value can then be obtained by removing the spatial noise outside the rectangular window. However, this method is only suitable for a fringe pattern with less noise. In addition, the rectangular window used is not optimal for a circular spectrum and it is not easy to determine the window size automatically. Using a maximum modulus algorithm of the 2D Gabor CWT, Eq. (3.14) becomes

$$\left| WT^l(q, \mathbf{b}_t, \theta) \right|_{\max} = \max \left| 2I_{l1}\pi^2 \exp(i\phi) \times \exp \left\{ -\frac{1}{2} \sigma^2 \left[\left(\frac{2\pi}{P} q \cos \varphi - k_0 \cos \theta \right)^2 + \left(\frac{2\pi}{P} q \sin \varphi - k_0 \sin \theta \right)^2 \right] \right\} \right| \quad (3.15)$$

In Eq. (3.15), when the local fringe direction and period are respectively equal to the wavelet direction and period multiplied by a constant, i.e. $\varphi = \theta$ and $q = (k_0 / 2\pi)P$, the modulus in Eq. (3.15) will reach its maximum value and is much greater than the

modulus of the wavelet transform of the noise, hence the phase value ϕ can be retrieved from Eq. (3.14) using the maximum modulus method of the wavelet transform. In the 2D Gabor CWT, the integration in Eq. (3.1) analyzes the local similarity between the 2D Gabor wavelets and the fringe pattern. The wavelets are dilated and rotated during processing. Wavelet transform is a local transform to measure the similarity between a daughter wavelet and the fringe pattern in a local region. When the wavelet and the fringe pattern are locally most similar, the modulus of the 2D CWT reaches its maximum value for a particular value of translation along the horizontal and vertical axis in the fringe pattern. Using the complex wavelet, phase information of the fringe pattern can be obtained from the real and imaginary parts of the wavelet transform.

Therefore, the 2D Gabor CWT algorithm shows a better speckle noise reduction capability than the 2D Fourier transform with a rectangular window filter. In this study, Eq. (3.14) is multiplied by the scale dilation parameter q and then the maximum modulus algorithm is employed to retrieve the phase. The parameter q does not affect the maximum modulus algorithm due to the exponential function of Eq. (3.14). This approximation shows a better noise reduction capability in the 2D Gabor CWT.

It should be noted that in the 2D Gabor CWT, the frequency window of the wavelet transform for a high frequency component is larger than that for a low frequency component, hence more noise will be introduced for a large frequency

window even though it is able to obtain more useful signals. A suitable window extension parameter σ should be selected to provide an optimal window. Normally, σ is recommended as an initial value of 0.5 (Wang and Ma, 2006).

3.2 Improved WFT for fringe demodulation

Unlike CWT, WFT has a fixed resolution for signal processing once a window size is selected. Therefore, the frequency window of a windowed Fourier element remains constant for either a high or low frequency component. It is a suitable method for demodulating a fringe pattern with either a wide or narrow spectrum due to the controllable time-frequency resolution.

3.2.1 Limitations of WFT with convolution algorithm

Windowed Fourier transform applied to phase retrieval has shown a good noise reduction capability. However, the WFT with convolution algorithm which is affected by the window size, image size and interval of the integration is time consuming. The intensity $I(x, y)$ of an interference fringe pattern can be expressed by Eq. (2.1). Similar to the 1D WFT, the 2D WFT and 2D inverse WFT of a fringe pattern using a convolution operation are given by

$$Sf(m, n, \varepsilon, \gamma) = [I(m, n) \otimes D_{\varepsilon, \gamma}(m, n)] \exp(-i\varepsilon m - i\gamma n) \quad (3.16)$$

$$I(x, y) = \frac{1}{4\pi^2} \int_{-\infty}^{+\infty} \int_{-\infty}^{+\infty} [I(x, y) \otimes D_{\varepsilon, \gamma}(x, y)] \otimes D_{\varepsilon, \gamma}(x, y) d\varepsilon d\gamma \quad (3.17)$$

where

$$D_{\varepsilon,\gamma}(x,y) = \exp\left(-\frac{x^2 + y^2}{2\sigma^2}\right) \exp(i\varepsilon x + i\gamma y) \quad (3.18)$$

and $D_{\varepsilon,\gamma}(x,y)$ represents the window element of the WFT. A filtered phase value can be retrieved using 2D windowed Fourier ridges or 2D WFF method (Qian, 2007b). Using the WFF with convolution algorithm, the computation time for phase retrieval from a fringe pattern of 512×512 pixels will be a few minutes and hence, the computation efficiency should be enhanced.

3.2.2 Phase retrieval using improved WFT

To reduce the computation time for phase retrieval, an improved algorithm of WFT is proposed. The algorithm is based on the introduction of a fast Fourier transform in WFT and able to avoid the window size effect on computation time. Windowed Fourier transform method includes windowed Fourier ridges method and WFF method. Theoretical analysis of the improved windowed Fourier ridges method and WFF method is proposed.

In Eq. (3.18), the window element of the WFT shows a Gaussian envelop and the Fourier spectrum of Eq. (3.18) is given by

$$\hat{D}_{\varepsilon,\gamma}(\omega_x, \omega_y) = 2\pi\sigma^2 \exp\left(-\frac{\sigma^2[(\omega_x - \varepsilon)^2 + (\omega_y - \gamma)^2]}{2}\right) \quad (3.19)$$

where “ \wedge ” denotes the Fourier spectrum. ω_x and ω_y are frequencies along the x - and y -axis, respectively. The constant factor $2\pi\sigma^2$ can be ignored for the given factor σ since it only affects the amplitude of the WFT except the phase. According to the convolution theorem (Mallat, 2001), convolution can easily be performed using frequency-domain multiplication by the fast Fourier transform, hence Eq. (3.16) can be written as

$$Sf(m, n, \varepsilon, \gamma) = \exp(-i\varepsilon m - i\gamma n) F^{-1}[\hat{I}(\omega_x, \omega_y) \hat{D}_{\varepsilon,\gamma}(\omega_x, \omega_y)] \quad (3.20)$$

where $\hat{I}(\omega_x, \omega_y)$ is the Fourier transform of $I(x, y)$ and F^{-1} denotes an inverse Fourier transform operation. Thus, Eq. (3.17) can be re-written as

$$I(x, y) = \frac{1}{4\pi^2} \int_{-\infty}^{+\infty} \int_{-\infty}^{+\infty} F^{-1}\left(F\{F^{-1}[\hat{I}(\omega_x, \omega_y) \hat{D}_{\varepsilon,\gamma}(\omega_x, \omega_y)]\} \hat{D}_{\varepsilon,\gamma}(\omega_x, \omega_y)\right) d\varepsilon d\gamma \quad (3.21)$$

where F denotes a Fourier transform operation. Furthermore, the phase $\phi(x, y)$ can be expressed as

$$\phi(x, y) = \phi(m, n) + \omega_1(m, n)(x - m) + \omega_2(m, n)(y - n) \quad (3.22)$$

where $\phi(m, n)$, $\omega_1(m, n)$ and $\omega_2(m, n)$ are respectively the phase value, frequency along the x - and y -axis at a point $M_0(m, n)$. The coordinate (m, n) is omitted for simplification. Thus $\hat{I}(\omega_x, \omega_y)$ is given as

$$\begin{aligned}\hat{I}(\omega_x, \omega_y) = & 4\pi^2 a \delta(\omega_x, \omega_y) \\ & + 2\pi^2 b \exp[i(\phi - \omega_1 m - \omega_2 n)] \delta(\omega_x - \omega_1, \omega_y - \omega_2) \\ & + 2\pi^2 b \exp[-i(\phi - \omega_1 m - \omega_2 n)] \delta(\omega_x + \omega_1, \omega_y + \omega_2)\end{aligned}\quad (3.23)$$

where δ is a Dirac function. In Eq. (3.23) the direct current term and two side-frequency components are separated by the carrier. The direct current and the left side-frequency components in the frequency domain are first removed to reduce their effect on phase retrieval from the right side-frequency component, and hence Eq. (3.23) becomes

$$\hat{I}_r(\omega_x, \omega_y) = 2\pi^2 b \exp[i(\phi - \omega_1 m - \omega_2 n)] \delta(\omega_x - \omega_1, \omega_y - \omega_2) \quad (3.24)$$

Substituting Eq. (3.24) into Eq. (3.20), we have

$$Sf(m, n, \varepsilon, \gamma) = \exp[-i(\varepsilon m + \gamma n)] 2\pi^2 b \exp(i\phi) \hat{D}_{\varepsilon, \gamma}(\omega_1, \omega_2) \quad (3.25)$$

The phase values ϕ are contained in Eq. (3.25) and can be retrieved from the following equation

$$\phi = \text{angle} \left(\exp[i(\varepsilon m + \gamma n)] Sf(m, n, \varepsilon, \gamma) \Big|_{\varepsilon=\omega_1, \gamma=\omega_2} \right) \quad (3.26)$$

The modulus of $Sf(m, n, \varepsilon, \gamma)$ would reach a maximum value when $\varepsilon = \omega_1, \gamma = \omega_2$ is satisfied. The phase value for the coefficient of $Sf(m, n, \varepsilon, \gamma)$ with a maximum modulus is equal to the phase of the fringe pattern. Phase retrieval from the ridges of the $Sf(m, n, \varepsilon, \gamma)$ is termed windowed Fourier ridges method. In Eq. (3.20), the fast Fourier transform is employed and the computation efficiency is improved for the windowed Fourier ridges method. In the WFF method, the phase ϕ can be obtained by substituting Eq. (3.24) into Eq. (3.21). The filtered values of $I(x, y)$ using the WFF method is given by

$$\overline{I(x, y)} = \frac{1}{4\pi^2} \int_{\gamma l}^{\gamma h} \int_{\varepsilon l}^{\varepsilon h} F^{-1} \left(F \left\{ \overline{F^{-1}[\hat{I}_r(\omega_x, \omega_y) \hat{D}_{\varepsilon, \gamma}(\omega_x, \omega_y)]} \right\} \hat{D}_{\varepsilon, \gamma}(\omega_x, \omega_y) \right) d\varepsilon d\gamma \quad (3.27)$$

where εl , εh and γl , γh are the integration limits of ε and γ , respectively, and

$$\overline{F^{-1}[\hat{I}_r(\omega_x, \omega_y) \hat{D}_{\varepsilon, \gamma}(\omega_x, \omega_y)]} = \begin{cases} F^{-1}[\hat{I}_r(\omega_x, \omega_y) \hat{D}_{\varepsilon, \gamma}(\omega_x, \omega_y)] & \text{if } \left| F^{-1}[\hat{I}_r(\omega_x, \omega_y) \hat{D}_{\varepsilon, \gamma}(\omega_x, \omega_y)] \right| \geq \text{threshold} \\ 0 & \text{if } \left| F^{-1}[\hat{I}_r(\omega_x, \omega_y) \hat{D}_{\varepsilon, \gamma}(\omega_x, \omega_y)] \right| < \text{threshold} \end{cases} \quad (3.28)$$

where $\overline{F^{-1}[\hat{I}_r(\omega_x, \omega_y) \hat{D}_{\varepsilon, \gamma}(\omega_x, \omega_y)]}$ denotes the filtered values of $F^{-1}[\hat{I}_r(\omega_x, \omega_y) \hat{D}_{\varepsilon, \gamma}(\omega_x, \omega_y)]$ using a threshold value. Only the modulus of $F^{-1}[\hat{I}_r(\omega_x, \omega_y) \hat{D}_{\varepsilon, \gamma}(\omega_x, \omega_y)]$ which is greater than or equal to the threshold value is

retained, otherwise it is set as zero. Using this method, speckle noise can be suppressed. The phase values ϕ are given by

$$\phi = \text{angle}(\overline{I(x, y)}) \quad (3.29)$$

where $\overline{I(x, y)}$ denotes a filtered fringe pattern, hence with the fast Fourier transform employed, the computation time using the WFF method is reduced significantly.

3.2.3 Suppression of boundary effect

With the introduction of fast Fourier transform in the WFT, the computation time for fringe demodulation can be reduced significantly. However, the Fourier transform of the fringe pattern is influenced by the boundary effect. To overcome this problem, the Gerchberg extrapolation method (Gerchberg, 1974; Roddier C. and F. Roddier, 1987; Chen et al, 2007) is employed to extrapolate the fringe pattern at each boundary (using 20 pixels). After applying the proposed WFT to the extrapolated fringe pattern, the desired area on a retrieved phase map can be obtained by removing the boundary. Before the Gerchberg method is employed, a fringe pattern is pre-processed to retain its grey value in the range of $[-v, +v]$, where v is the maximum grey value (chosen as 127.5 in this study). Figure 3.3 shows a flow chart of the Gerchberg extrapolation method. The processed fringe pattern is padded with zeros at each boundary (with 20 pixels) and the fast Fourier transform is then applied to obtain the Fourier spectrum. The zero frequency and two-side lobes are then selected. Frequencies outside the

selected areas in the Fourier spectrum are set to zeros. An inverse Fourier transform of this Fourier spectrum would produce a fringe pattern with the extrapolated fringes. The values within the extrapolated fringe pattern are replaced by the original values. Another fast Fourier transform is then performed on the newly generated fringe pattern and the whole procedure is repeated. After N iterations, the desired extrapolated fringe pattern is obtained. In this study, ten iterations are required to obtain a satisfactory fringe pattern.

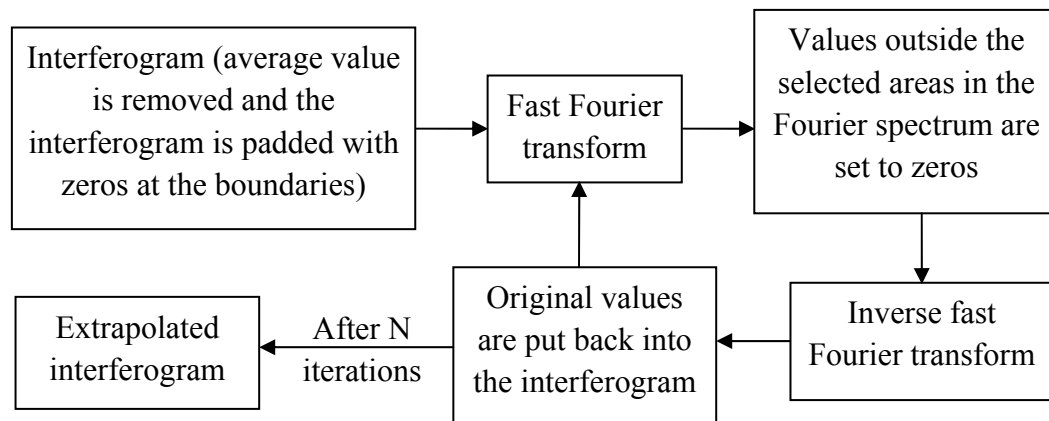


Fig. 3.3 Flow chart of the Gerchberg extrapolation method

An example of the fringe extrapolation using this technique is shown in Fig. 3.4. After 10 iterations, an extrapolated speckle fringe pattern from the original speckle fringe pattern is obtained. It should be noted that the Gerchberg extrapolation method requires a proper selection of the Fourier spectrum.

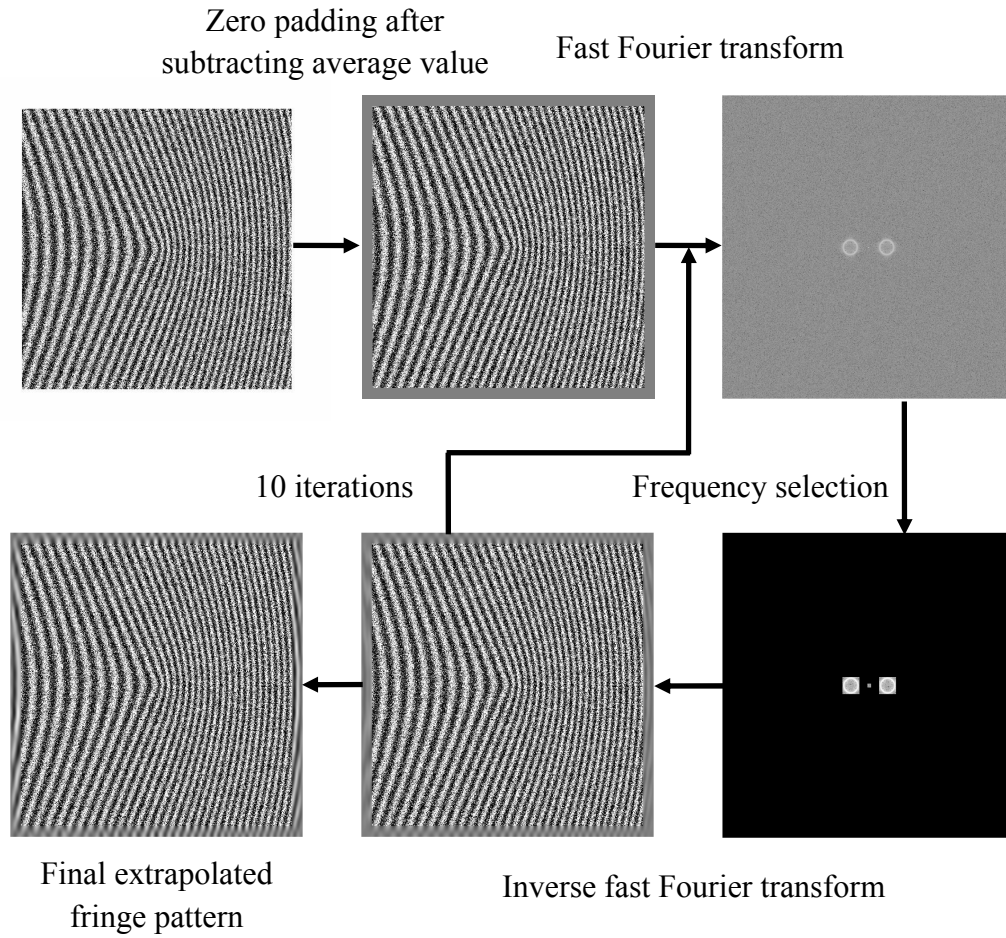


Fig. 3.4 An example of fringe extrapolation

3.3 Phase fringe denoising using windowed Fourier filtering

Speckle noise reduction is an important aspect in the WFF method. Since speckle noise always appears in laser interferograms, it is necessary to suppress the speckle noise for accurate measurement. Moreover, speckle noise reduction in a phase fringe pattern is often necessary since the noise will affect the spatial phase unwrapping techniques to obtain a correct continuous phase map. For relatively large deformation measurement, wrapped phase maps are usually dense and conventional sine-cosine average filtering technique is difficult to reduce the noise in such a case. In this

section, the WFF method is proposed to reduce speckle noise in wrapped phase maps for deformation measurement.

3.3.1 Phase retrieval for relatively large deformation measurement

Digital speckle shearing interferometry is widely employed to determine the deformation derivative. However, for relatively large deformation measurement using single wavelength illumination, the iterative sine-cosine average filtering (ISCAF) method, which is a commonly used filtering technique for noise reduction, is no longer suitable to filter the wrapped phase pattern correctly. The ISCAF technique only works well in phase fringe patterns which are relatively less dense, hence the measurement range is limited especially when a single wavelength is used. Since the WFF technique shows a good potential in noise reduction for phase retrieval from a noisy fringe pattern, it is proposed to reduce speckle noise of a dense phase fringe pattern for relatively large deformation measurement using single wavelength illumination in DSSI.

3.3.1.1 Windowed Fourier filtering

Using Carré algorithm, four interferograms are recorded with the phase between two consecutive interferograms shifted by a constant amount. The phase is retrieved using Eq. (2.19). The phase value at each point in the interferogram before and after the object deformation (ϕ_b and ϕ_a) can be obtained and the phase difference $\Delta\phi$ is given by

$$\Delta\phi = \phi_a - \phi_b = \frac{4\pi\Delta_x}{\lambda} \frac{\partial w}{\partial x} \quad (3.30)$$

where λ is the wavelength used, Δ_x is a shear value in the x -direction, w is the out-of-plane deformation and $\partial w / \partial x$ is the derivative of out-of-plane deformation. As $\Delta\phi$ is in modulo of 2π , it needs to be unwrapped. However, speckle noise contained in the phase map of $\Delta\phi$ requires to be suppressed before phase unwrapping. The phase deference obtained from Eq. (3.30) can be represented using the complex form by

$$P_1(x, y) = \exp[i\Delta\phi(x, y)] \quad (3.31)$$

where $P_1(x, y)$ represents the unfiltered complex phase values. Applying the WFF method using Eqs. (3.27) and (3.28), the filtered phase difference is given by

$$\overline{\Delta\phi(x, y)} = \text{angle}(\overline{P_1(x, y)}) \quad (3.32)$$

while $\overline{P_1(x, y)}$ indicates the filtered values of $P_1(x, y)$. The filtered phase fringe pattern $\overline{\Delta\phi(x, y)}$ representing the measurand can then be unwrapped correctly using spatial phase unwrapping (Ghiglia and Pritt, 1998).

3.3.1.2 Iterative sine-cosine average filtering

Since the WFF method requires correct parameters for noise reduction and phase retrieval, it is complicated to use compared with the ISCAF method. The ISCAF technique was employed by Aebischer and Waldner (1999) for speckle noise suppression in phase retrieval due to its simplicity. It is a suitable technique for filtering a phase fringe pattern with low fringe density when combined with the multiple-wavelength technique, which can provide a longer synthetic wavelength and less dense phase fringe pattern compared with the single wavelength technique for relatively large deformation measurement (Wagner et al, 2000; Patil and Rastogi, 2007; Kumar et al, 2009a; Kumar et al, 2009c). In two-wavelength DSSI, the phase difference $\Delta\phi_s(x, y)$ of the synthetic wavelength λ_s is given by

$$\Delta\phi_s(x, y) = \Delta\phi_g(x, y) - \Delta\phi_r(x, y) = \frac{4\pi\Delta_x}{\lambda_s} \frac{\partial w}{\partial x} \quad (3.33)$$

where $\Delta\phi_g(x, y)$ and $\Delta\phi_r(x, y)$ are the phase difference of a green and red lights, respectively, and the synthetic wavelength λ_s is given by Eq. (2.17). Since the phase can be represented as a complex datum using Eq. (3.31), $\Delta\phi_s(x, y)$ is given by

$$\exp[i\Delta\phi_s(x, y)] = Re + iIm \quad (3.34)$$

where $Re = \cos[\Delta\phi_s(x, y)]$ and $Im = \sin[\Delta\phi_s(x, y)]$ are respectively the real and

imaginary parts of the complex phase. In the ISCAF technique, the real and imaginary parts are individually filtered iteratively by an average filtering with a rectangular window. The speckle noise is suppressed and the filtered phase map is retrieved by an arctangent operation as

$$\overline{\Delta\phi_s(x, y)} = \arctan\left(\frac{\overline{Im}}{\overline{Re}}\right) \quad (3.35)$$

where the symbol “ $\overline{}$ ” indicates a filtering operation.

3.3.2 Combined filtering technique for noise reduction

The multi-wavelength interferometry, also known as synthetic wavelength interferometry, has advantages over single wavelength interferometry for ambiguity-free measurement (Cheng and Wyant, 1984; Kumar et al, 2009a; Kumar et al, 2009b; Kumar et al, 2009c). It has also been applied to surface profile and slope measurements (Huang et al, 1997; Hack et al, 1998). However, a disadvantage of the multi-wavelength technique is that the phase noise is amplified (Warnasooriya and Kim, 2009). A novel technique to suppress the noise in a two-wavelength interferometry using simultaneous red and green lights illumination for small displacement derivative measurement is proposed. The proposed method can also avoid the conventional spatial phase unwrapping if the optical path difference of the measurands is less than the synthetic wavelength. In addition, to achieve the same

level of sensitivity as the single wavelength method, the phase map obtained by the synthetic wavelength is used to guide the phase unwrapping for either of the individual wavelength. A combined filtering technique consisting of WFF and a phase error correction algorithm is proposed for noise reduction and phase retrieval.

In DSSI using two-wavelength simultaneous illumination, the red ($\lambda_r = 632.8$ nm) and green ($\lambda_g = 532$ nm) lights are employed. The phase difference, which is obtained by subtraction of the phase values retrieved using Carré phase shifting method before and after the object deformation, indicates the slope of a test object for a particular wavelength. However, the resulting phase map is normally very noisy due to the speckles. For speckle noise reduction of a phase fringe pattern, the fast WFF algorithm is employed. Let $\overline{\Delta\phi_r}$ and $\overline{\Delta\phi_g}$ be the filtered phase values for the red and green lights, respectively, using the fast WFF technique. The difference between these two filtered phase values produces a phase value $\Delta\phi_s$ of the synthetic wavelength λ_s given by Eq. (2.17) and is expressed as

$$\Delta\phi_s = \overline{\Delta\phi_g} - \overline{\Delta\phi_r} = \frac{4\pi\Delta_x}{\lambda_s} \frac{\partial w}{\partial x} \quad (3.36)$$

As the phase difference $\Delta\phi_s$ still contains noise, it is again filtered by fast WFF to obtain a noise reduced phase $\overline{\Delta\phi_s}$ which is in principle an unwrapped phase as long as the optical path difference of the measurands is less than the synthetic wavelength. The phase $\overline{\Delta\phi_s}$ can thus be used to evaluate the derivative $\partial w / \partial x$. However, due to

error amplification, the derivatives obtained directly from $\overline{\Delta\phi_s}$ contain relatively large error compared with those obtained from a spatially unwrapped phase map of the green light. To improve the accuracy and avoid the conventional spatial phase unwrapping, integral multiples of 2π obtained from $\overline{\Delta\phi_s}$ are used to guide the unwrapping of $\overline{\Delta\phi_g}$ (assuming $\overline{\Delta\phi_s}\lambda_s = \Delta\phi_{gu}\lambda_g$ where $\Delta\phi_{gu}$ is an unwrapped phase of the green light). However, spikes arise in some values of $\Delta\phi_{gu}$ due to incorrect integral multiples of 2π . A phase error correction algorithm is introduced to remove the spikes in $\Delta\phi_{gu}$. It is worth mentioning that the WFF technique is first employed to suppress the speckle noise in the phase map which can not be removed by the proposed phase error correction algorithm.

3.3.2.1 Phase error correction algorithm

This section describes a phase error correction algorithm for removing incorrect integral multiples of 2π in $\Delta\phi_{gu}$. Figure 3.5 shows a flow chart of the phase error correction algorithm. Figures 3.6(a) and 3.6(b) show respectively subroutines 1 and 2 in Fig. 3.5. In Fig. 3.5, ‘*round()*’ indicates rounding off of values to the nearest integer and ‘*diff()*’ indicates an operation to calculate the phase difference between adjacent pixels along the x -axis. There are five steps in the algorithm. In step 1, the values of *Coef* are first obtained from $\overline{\Delta\phi_s}$ and in step 2, the values of $\Delta\phi_{gu}$ are subsequently determined from $\overline{\Delta\phi_g}$ and *Coef*, where $\overline{\Delta\phi_{gu}}$ represents the filtered values of $\Delta\phi_{gu}$ and is assigned the values of $\Delta\phi_{gu}$ before phase error correction is carried out. In step 3, the phase difference $P_diff(i, j)$ between adjacent pixels of $\overline{\Delta\phi_{gu}}$ along the

x -axis is calculated as

$$P_diff(i_1, j) = \overline{\Delta\phi_{gu}}(i_1, j+1) - \overline{\Delta\phi_{gu}}(i_1, j) \quad (3.37)$$

where $i_1 = 1, 2, 3, \dots, Row$, $j = 1, 2, 3, \dots, Col-1$, Row and Col are respectively the row and column numbers of $\overline{\Delta\phi_{gu}}$. In the flowchart, step 4 calculates the values of $Coef_diff$ to the nearest integer which are then used to remove any spike in $\overline{\Delta\phi_{gu}}$. $Coef_diff$ can either be positive, zero or negative integers. In step 5, line scanning of $Coef_diff$ is performed to detect any errors shown as an upward or downward spike in the phase map $\overline{\Delta\phi_{gu}}$. The errors in the phase values of $\overline{\Delta\phi_{gu}}$ due to upward or downward spikes are corrected by subtracting (for upward spike) or adding (for downward spike) 2π . As shown in Figs. 3.6(a) and 3.6(b), Subroutine 1 and Subroutine 2 are applied to correct the phase values due to the downward and upward spikes, respectively. A pair of positive and negative numbers in each line of $Coef_diff$ indicates a spike in the same line of $\overline{\Delta\phi_{gu}}$. A positive number followed by a negative number indicates an upward spike in the same line of $\overline{\Delta\phi_{gu}}$ (zeros may appear in between), therefore, a 2π value would need to be subtracted to the phase values of $\overline{\Delta\phi_{gu}}$ and vice versa. After the correction, if spikes still exist in the phase map, steps 3 to 5 would be repeated. The processed $\overline{\Delta\phi_{gu}}$ is taken as the final unwrapped phase.

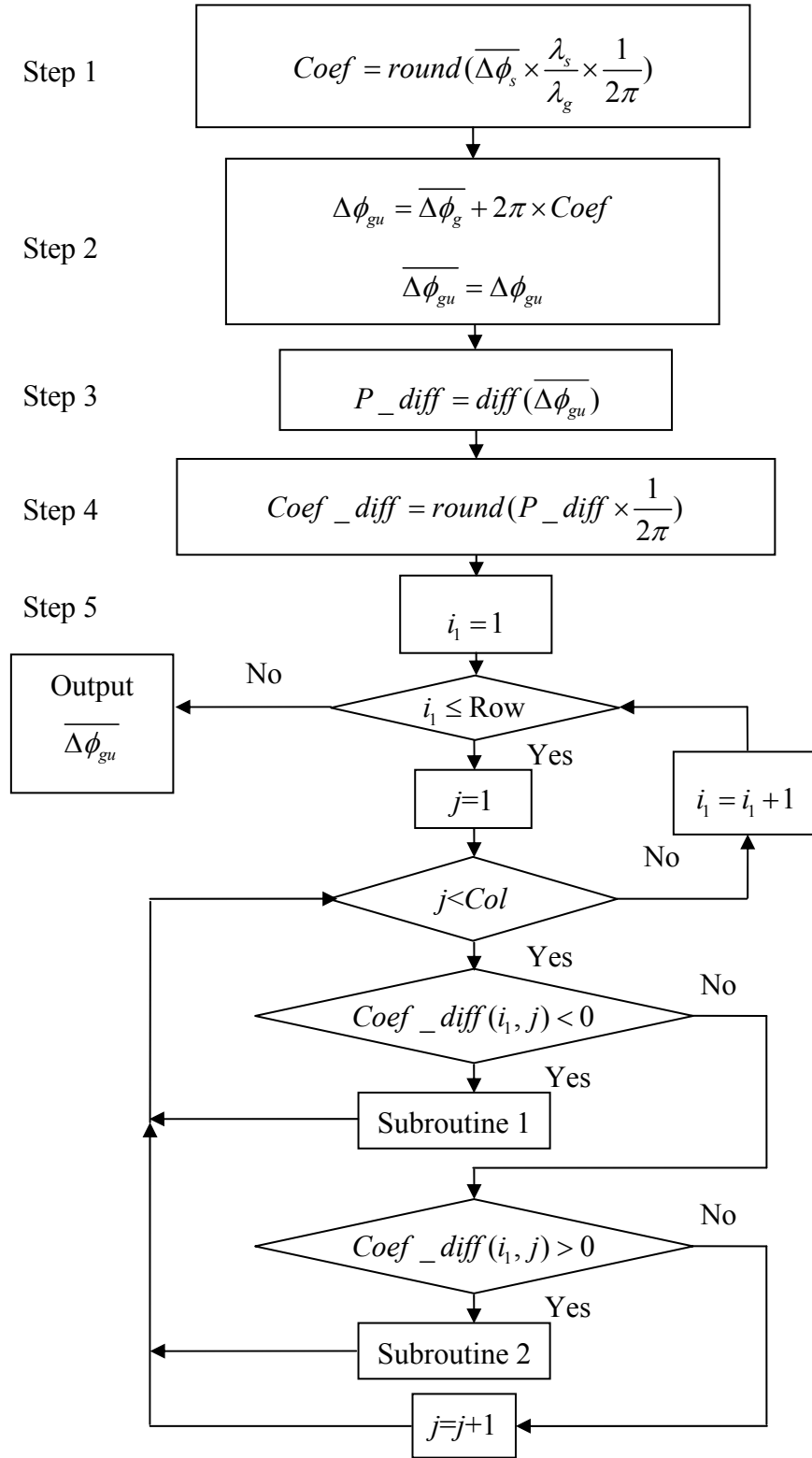
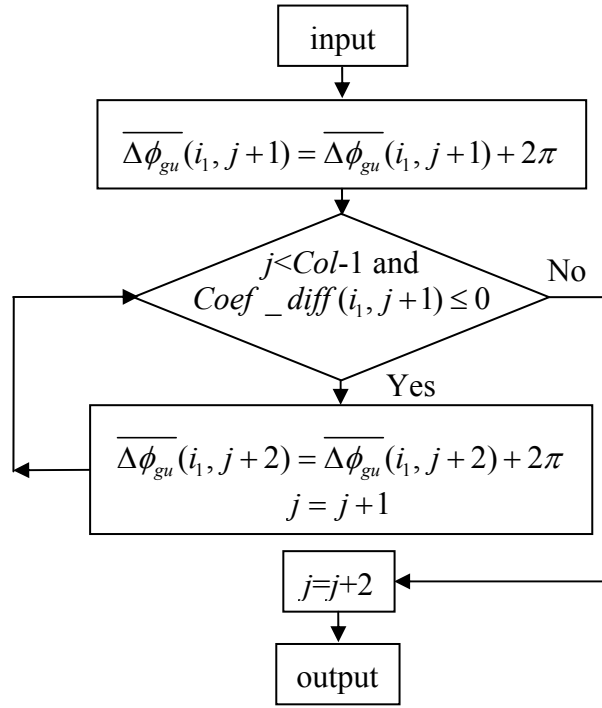
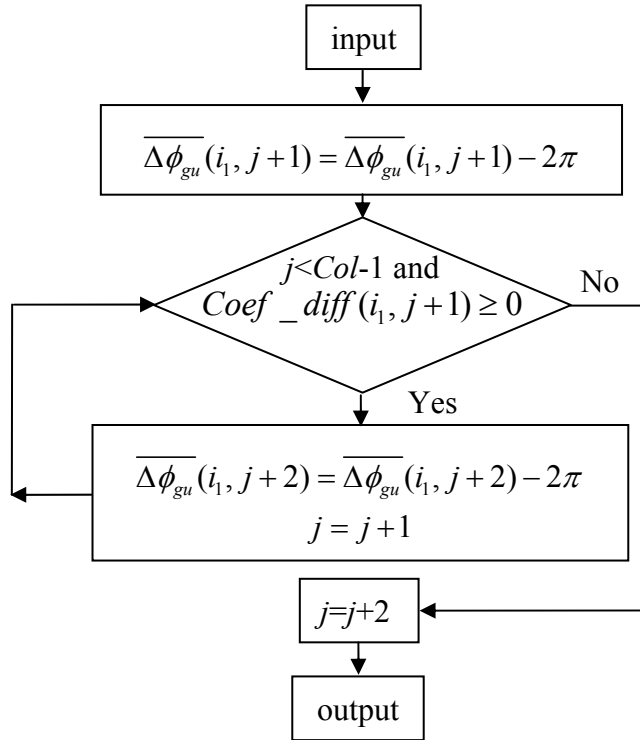


Fig. 3.5 A flow chart of the phase error correction algorithm



(a)



(b)

Fig. 3.6 (a) Subroutine 1; (b) Subroutine 2

CHAPTER FOUR

EXPERIMENTAL WORK

This chapter details the experimental work carried out to verify the proposed methods. The experimental work consists of ESPI with carriers for deformation measurement, DSSI with carriers for deformation derivative measurement, ESPI with temporal phase shifting for deformation measurement, and two-wavelength DSSI with temporal phase shifting for deformation derivative measurement.

4.1 ESPI with carriers

Figure 4.1 shows a Michelson type ESPI setup for deformation measurement. The specimen used in this experiment is a circular aluminum plate fully clamped at the boundary and has a diffused surface. The diameter and thickness of the circular plate are respectively 65.4mm and 1.66mm. A load is applied to the center of the plate by a micrometer screw and a He–Ne laser (30mW, $\lambda = 632.8\text{nm}$) is used for illumination. The expanded beam from the laser is divided into two beams by a beam splitter: one is an object beam and the other is a reference beam. The object beam illuminates the surface of the specimen and the reflected beam is imaged at a CCD camera (Pulnix TM-62EX) through the beam splitter. The reference beam illuminates a reference plate and the reflected beam is recorded at the image plane of the CCD camera after passing through the beam splitter. The object and reference beams interfere on the

image plane of the camera and produce a speckle interferogram. This interferogram is used to extract the phase information due to any change on the object surface.

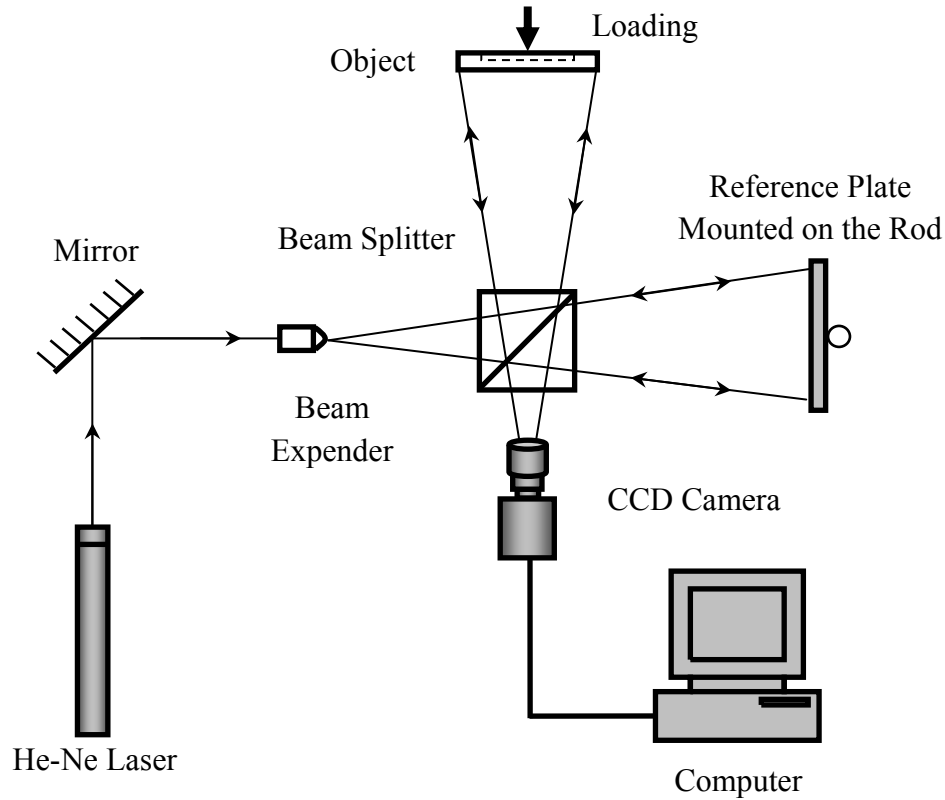


Fig. 4.1 ESPI setup for deformation measurement

In the experiment, a speckle pattern is first captured before the object plate is deformed. A carrier is then introduced by tilting the reference plate by a small angle and the second speckle pattern is captured. The object plate is then deformed by applying a central load with a micrometer screw and the third speckle pattern is captured. Subtraction of the first and second images by Eq. (2.7) produces a speckle fringe pattern due to the carrier. Subtraction of the first and third images by Eq. (2.7) produces a speckle fringe pattern of the carrier modulated by the object deformation.

With the introduction of the carrier, the spectrum of the speckle fringe pattern can be separated. The Fourier transform and 2D wavelet transform methods are employed for phase retrieval from the noisy speckle fringe patterns and the object deformation is obtained using Eq. (2.8). The size of the image captured by the CCD camera is 768×576 pixels.

4.2 DSSI with carriers

Figure 4.2 shows a DSSI setup for out-of-plane displacement derivative measurement. The test specimen used is also a circular plate with a diffused surface and is fully clamped at the boundary. The plate, which has a diameter of 5cm, is loaded at the center by a micrometer head. A He–Ne laser (50 mW, $\lambda = 632.8 \text{ nm}$) beam is directed through an optical fiber and illuminates the specimen at a small illumination angle (θ_3), which is less than 10° . The output connector of the optical fiber is mounted on a translation stage which is used to introduce carrier fringes by translation of the fiber along the direction of illumination. The distance between the plate and the beam splitter cube is 57 cm. The magnitude of the shear in the x direction is 1 cm and the resulting speckle pattern is captured by a CCD camera (Pulnix TM-62EX CCD with a Nikon Micro-Nikkor 55 mm lens). The image size captured by the CCD camera is 768×576 pixels.

Similar to the ESPI system, three speckle interferograms are captured. One is before the object deformation, a second one is after introduction of the carrier and a third is captured after the object deformation. The carrier fringe pattern is obtained by

subtraction between the first and the second interferograms. Subtraction of the first and third interferograms produces a modulated carrier speckle fringe pattern due to the object deformation. The phase of the carrier fringe pattern and the modulated carrier fringe pattern are obtained by the fast WFF method as explained in Section 3.2. Subtraction of the two phase maps results in a phase map representing the deformation derivative of the object.

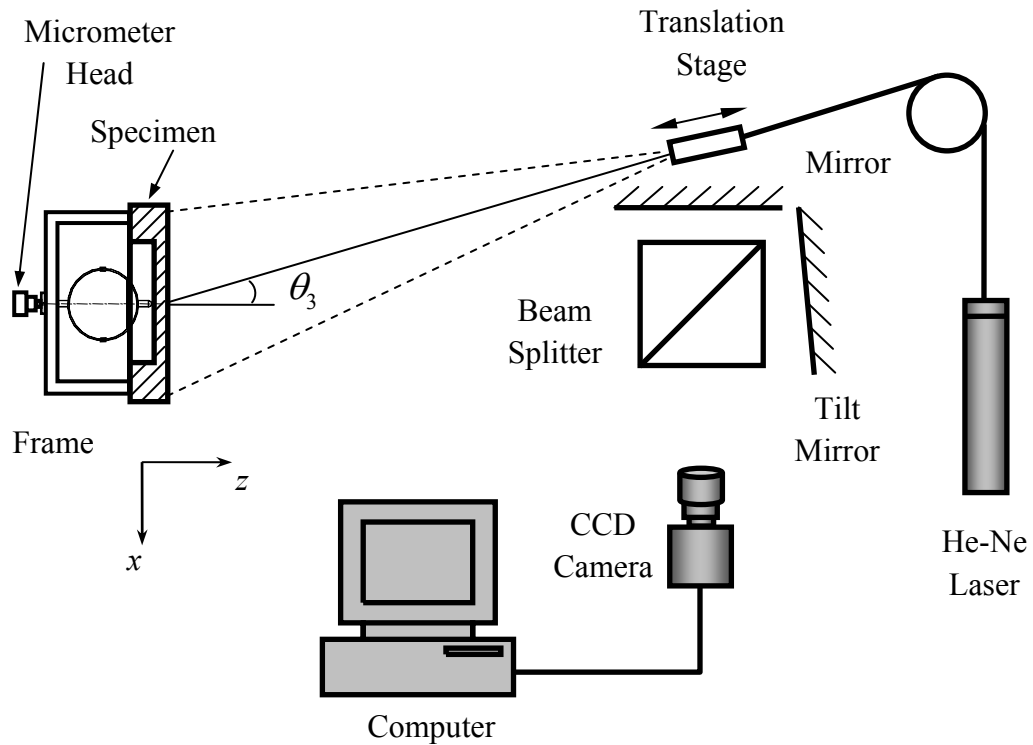


Fig. 4.2 DSSI for deformation derivative measurement with carriers

4.3 ESPI with temporal phase shifting

An experiment is carried out using the ESPI technique with temporal phase shifting to measure the deformation of a fully clamped circular plate. The resulting phase fringe

patterns are processed using the proposed WFF method. Figure 4.3 shows the experimental setup of ESPI with temporal phase shifting for deformation measurement. A diffused surface circular plate with a diameter of 6.54 cm is illuminated by a He-Ne laser (wavelength $\lambda_r = 632.8$ nm) and is loaded at the center by a micrometer head. A beam splitter is employed to separate the expanded beam into an object and a reference beams. The object beam illuminates the plate, while the reference beam illuminates a diffused reference plate. The reference plate is mounted on a PZT transducer, which moves the reference plate by a constant distance in order to introduce a phase shift before and after the object is deformed. A 3-CCD color camera (JAI CV-M9CL) is used to capture four phase shifted images each before and

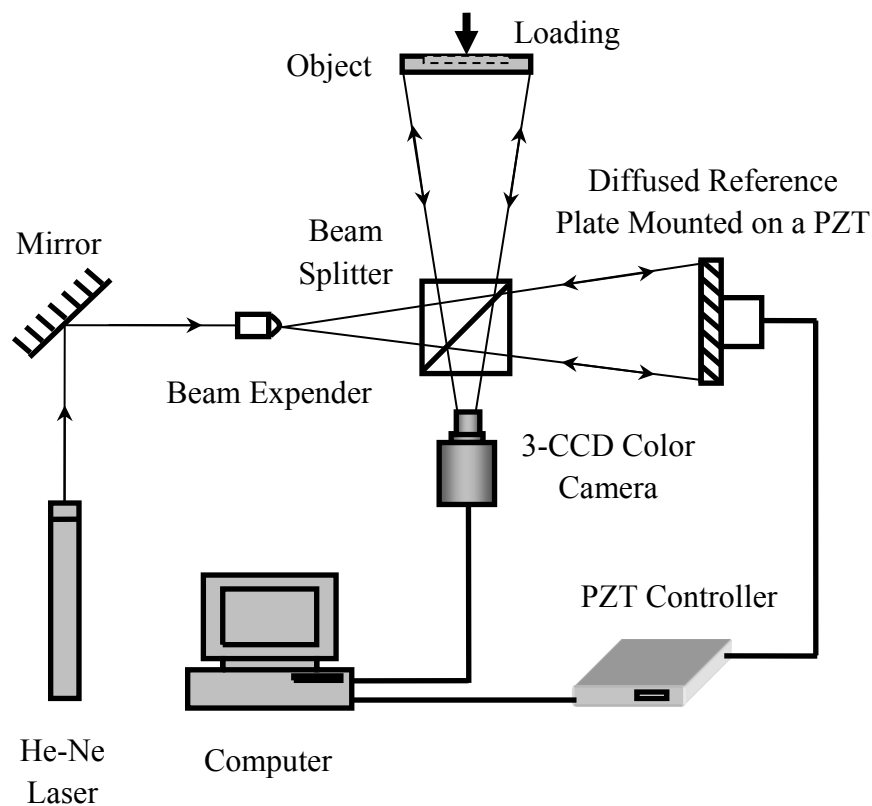


Fig. 4.3 ESPI for deformation measurement with phase shifting

after the object is deformed. As the red light is used, the speckle interferograms are recorded by the red channel of the 3-CCD camera. The phase difference of the speckle interferograms are obtained by subtracting the phase maps obtained before and after the object deformation. The deformation of the object is then obtained from the phase difference.

4.4 Two-wavelength DSSI system

Figure 4.4 shows the experimental setup of a two-wavelength DSSI for deformation derivative measurement of a centrally loaded fully clamped circular plate of diameter 6.54 cm with a diffused surface. The experiment is carried out on a vibration isolation table (MELLES GRIOT). Both single and two-wavelength techniques are investigated. Illumination is carried out using red and green beams generated by a He-Ne laser (wavelength $\lambda_r = 632.8$ nm) and a diode pumped solid state laser (wavelength $\lambda_g = 532$ nm), respectively. The red and green beams are combined by a beam splitter and then expanded by a beam expander for simultaneously illuminating the test object at a small incident angle, as shown in Fig. 4.4. Shearing is carried out by a beam splitter and two mirrors. One of the mirrors is tilted to introduce a shear of 5 mm in the x -direction while another mirror is mounted on a computer controlled PZT to introduce a phase shift. A 3-CCD color camera (JAI CV-M9CL) is used to capture the interference patterns before and after the object is deformed. Two different speckle shearing interference patterns of red and green beams are captured separately at the red and green channels of the CCD camera in one single exposure. The constant but

different phase shifting values for red and green beams are achieved by moving the mirror mounted on the PZT by a constant distance. Four phase shifted images each before and after the object is deformed are recorded. The phase shift values for red and green beams are $\delta_r = 1.1424$ rad and $\delta_g = 1.3594$ rad, respectively.

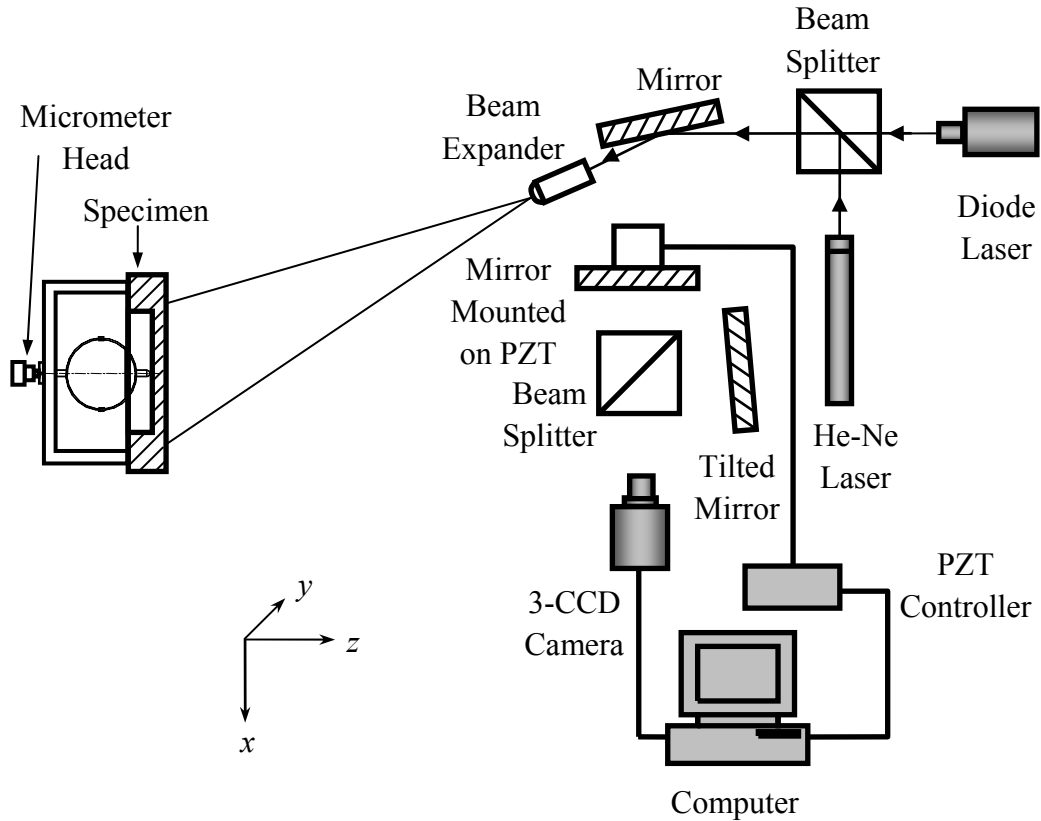


Fig. 4.4 Two-wavelength DSSI for deformation derivative measurement

From the phase shifted images the phase values for the two wavelengths are retrieved using the Carré phase shifting algorithm. For each wavelength the phase difference due to the object deformation is obtained by subtraction of the phases before and after the object deformation. In this experiment, both the single and two-wavelength technique can be used to measure a relatively large deformation and the proposed WFF can be employed to retrieve the phase values using the single

wavelength technique. As a comparison, the ISCAF method is used on a noisy sparse phase fringe pattern obtained by the two-wavelength technique. The measurements are also verified using strain gauge measurement. The proposed combined filtering method is also verified using this experimental setup.

CHAPTER FIVE

RESULTS AND DISCUSSION

5.1 Two-dimensional CWT for phase retrieval in ESPI

The novel 2D Gabor CWT for phase retrieval and fringe filtering of a speckle fringe pattern with a spatial carrier is employed. Both the computer simulation and experimental results are shown. The computer program of the 2D Gabor CWT is also shown in Appendix A.

5.1.1 Simulation results

The phase values of a speckle fringe pattern of 512×512 pixels can be simulated by

$$\phi(\mathbf{X}) = 0.15[(x - 256)^2 + (y - 256)^2]^{1/2} \quad (5.1)$$

The intensity of a point on the speckle fringe pattern is given by

$$I(\mathbf{X}) = \cos[2\pi f_x x + \phi(\mathbf{X})] + WGN \quad (5.2)$$

where WGN represents white Gauss noise and f_x is the carrier in the x direction (set to $1/16$). The white Gauss noise is set to a zero mean with a variance of 0.3. Figure 5.1(a) shows the phase values $\phi(\mathbf{X})$. Figure 5.1(b) shows the simulated phase values

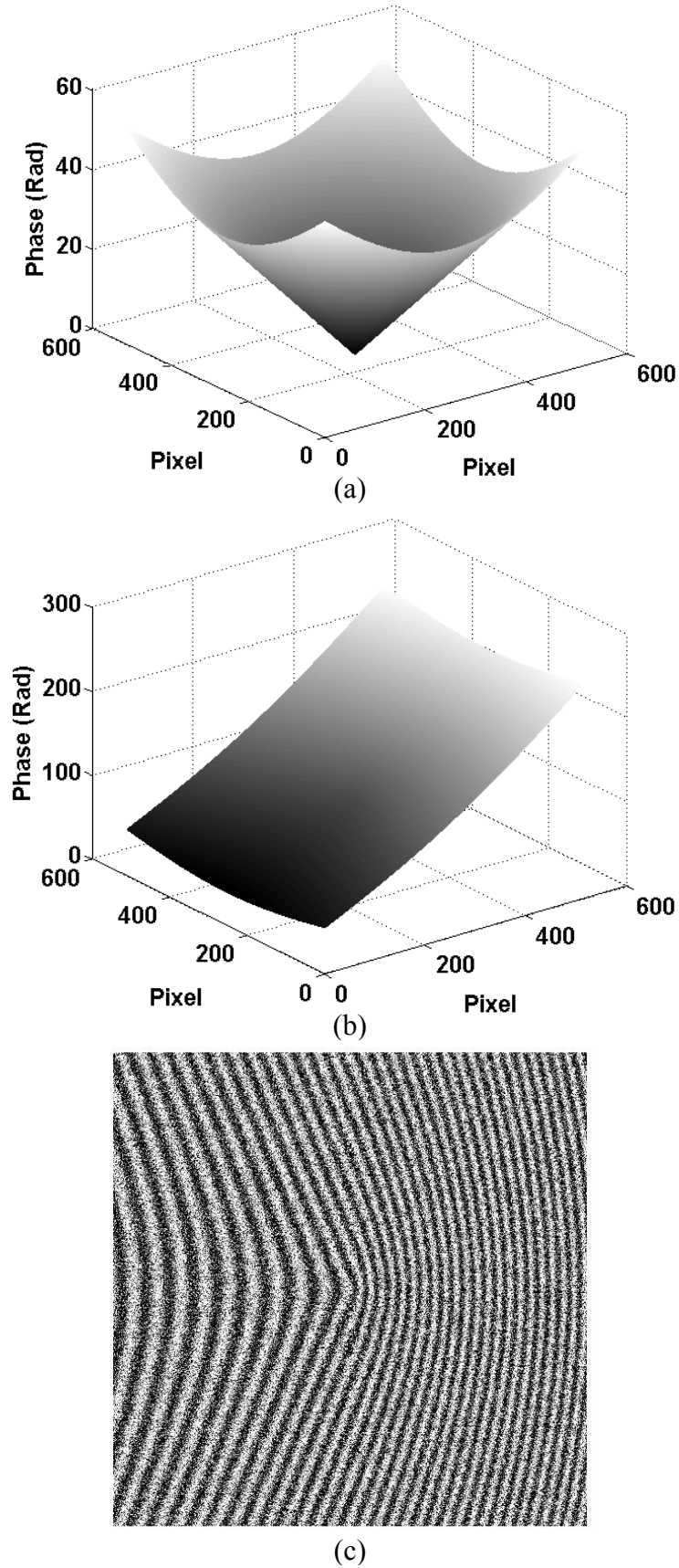


Fig. 5.1 (a) Original phase values $\phi(X)$; (b) simulated phase values with a carrier; (c) simulated fringe pattern with WGN

with a carrier added and Fig. 5.1(c) shows a simulated fringe pattern with WGN . Before applying the 2D Gabor CWT, the Gerchberg method which can reduce the boundary effect is employed to extrapolate the fringe pattern at each boundary. The zero-frequency term and left side-frequency component are subsequently removed from the spectrum of the extrapolated fringe pattern and the 2D CWT method is used to extract the CWT coefficients with maximum modulus, and the phase values of the fringe pattern are obtained from the coefficients. Figures 5.2(a) and 5.2(b) show wrapped phase maps retrieved using 2D Gabor CWT and advanced 2D fan CWT, respectively. The wrapped phase map retrieved by the advanced 2D fan CWT is more susceptible to the noise than that retrieved by the 2D Gabor CWT. Figures 5.3(a) and 5.3(b) show the error maps of the retrieved phase maps. The root mean square error

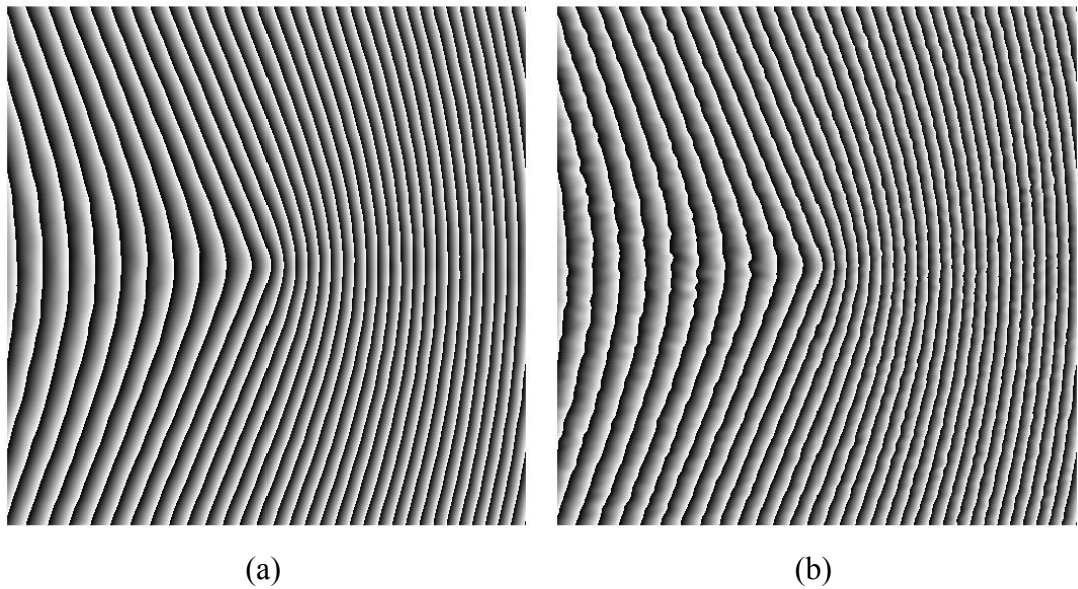
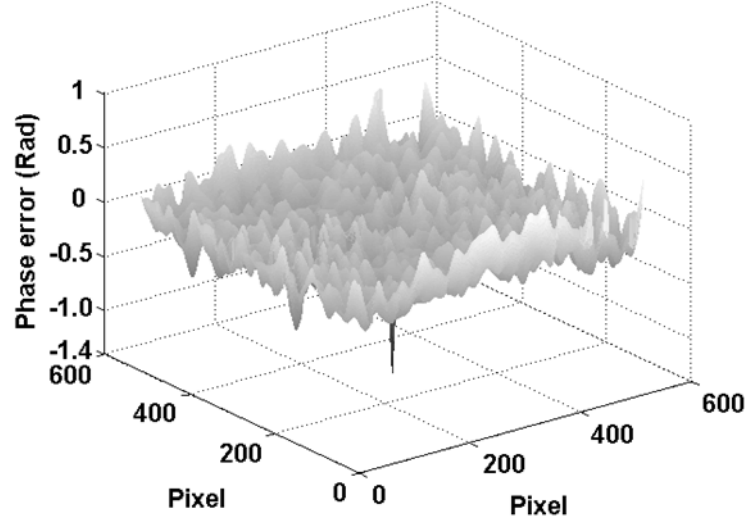
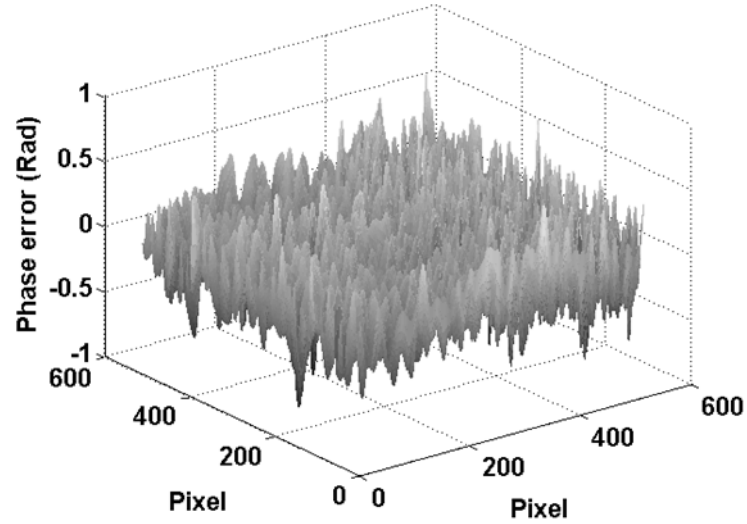


Fig. 5.2 (a) Wrapped phase map retrieved using 2D Gabor CWT;
(b) wrapped phase map retrieved using advanced 2D fan CWT

(RMSE) for the 2D Gabor CWT is 0.1013 (Fig. 5.3a) and the RMSE for the advanced 2D fan CWT is 0.1695 (Fig. 5.3b).



(a)



(b)

Fig. 5.3 (a) Error map by 2D Gabor CWT; (b) error map by advanced 2D fan CWT

Figure 5.4 shows the errors on the 256th row of the phase maps obtained using the two methods: the solid line denotes the 2D Gabor CWT errors and the dash line

denotes the advanced 2D fan CWT errors. As can be seen from Fig. 5.4, there is larger fluctuation in the errors of the advanced 2D fan CWT due to the wider spectrum of the advanced 2D fan wavelet. The wider spectrum of a wavelet is helpful for obtaining the useful signal simultaneously with more noise introduced. However, if the wavelet spectrum width is narrow, insufficient signal may be obtained and phase demodulation may be unsuccessful. Since wavelet transform acts as a filter in the frequency domain of a fringe pattern, there is a tradeoff in the spectrum size of the wavelet between obtaining useful signal and a noise reduction. As can be seen from the simulated results, the 2D Gabor CWT has a better noise immunity than the advanced 2D fan CWT.

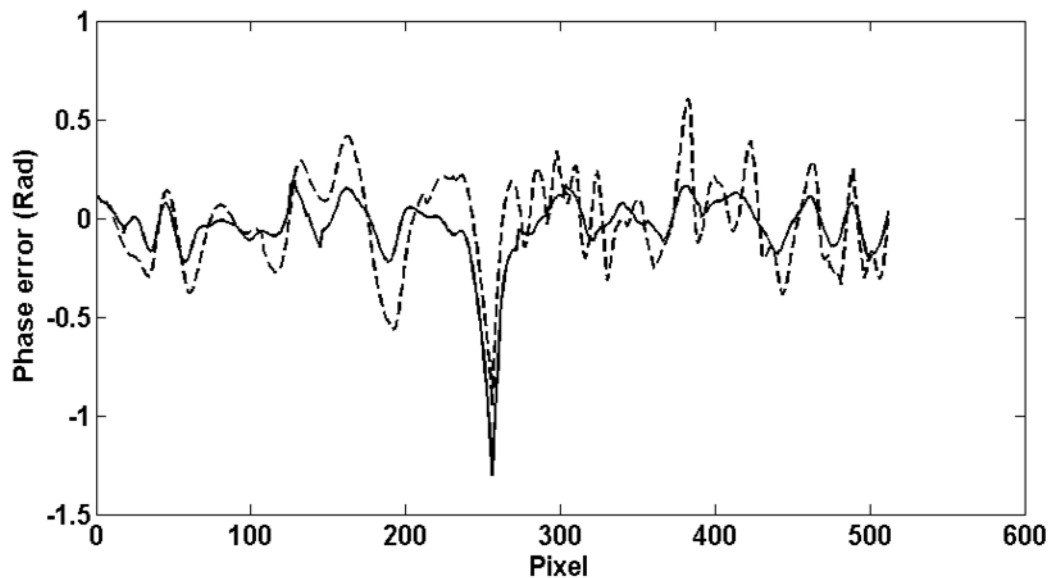


Fig. 5.4 Error on the 256th row of phase maps obtained using the two methods: the solid line denotes the 2D Gabor CWT errors and the dash line denotes the advanced 2D fan CWT errors

5.1.2 Experimental results

The speckle fringe patterns are obtained from the ESPI with carriers for deformation measurement. The image size of the speckle fringe pattern used for processing is 571×576 pixels. Figure 5.5 shows a speckle fringe pattern with spatial carriers on a deformed plate. The carriers require to be introduced by the reference plate for phase retrieval using the proposed 2D CWT method. The speckle fringe pattern appears more noise than the simulated speckle fringe pattern. The Gerchberg method is first employed to extrapolate the fringe pattern at the boundary. The zero-frequency term and the left side-frequency component of the speckle fringe pattern are then removed in the frequency domain for further processing. The advanced 2D fan CWT, 2D Fourier transform with a small rectangular filtering window and 2D Gabor CWT are subsequently employed to the spectrum of the fringe pattern after the pre-processing. Figures 5.6(a), 5.6(b) and 5.6(c) show respectively wrapped phase obtained using the advanced 2D fan CWT, 2D Fourier transform and 2D Gabor CWT. As can be seen,

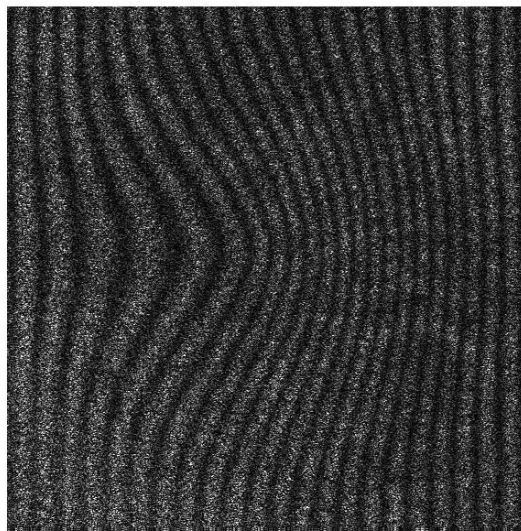
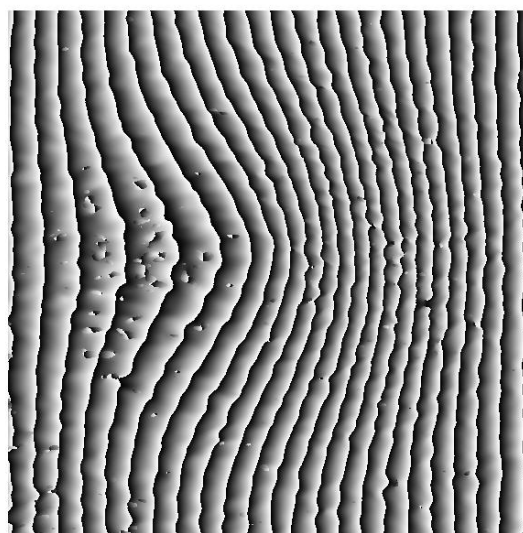
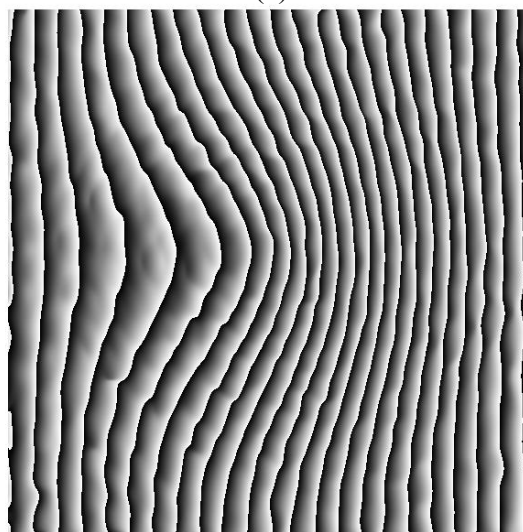


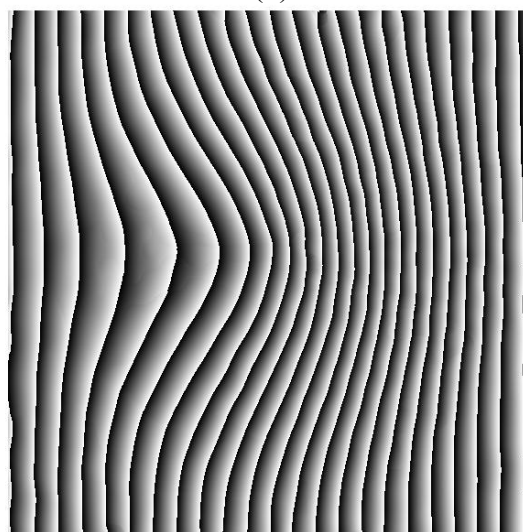
Fig. 5.5 Speckle fringe pattern with spatial carriers



(a)



(b)



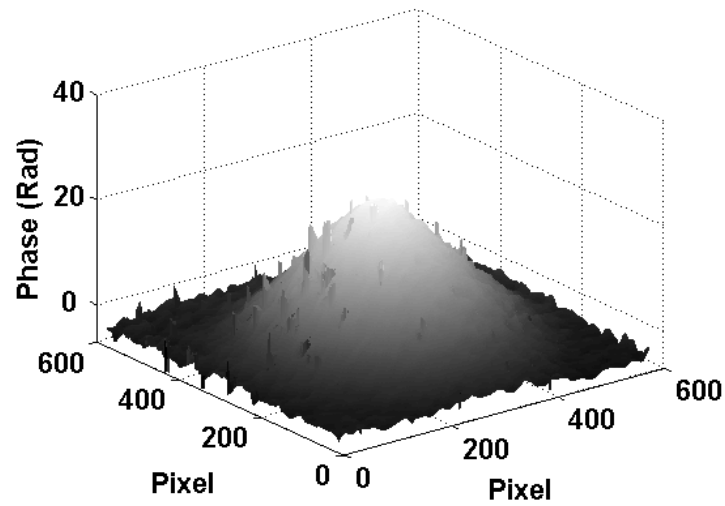
(c)

Fig. 5.6 (a) Wrapped phase map by advanced 2D fan CWT; (b) wrapped phase map by 2D Fourier transform; (c) wrapped phase map by 2D Gabor CWT

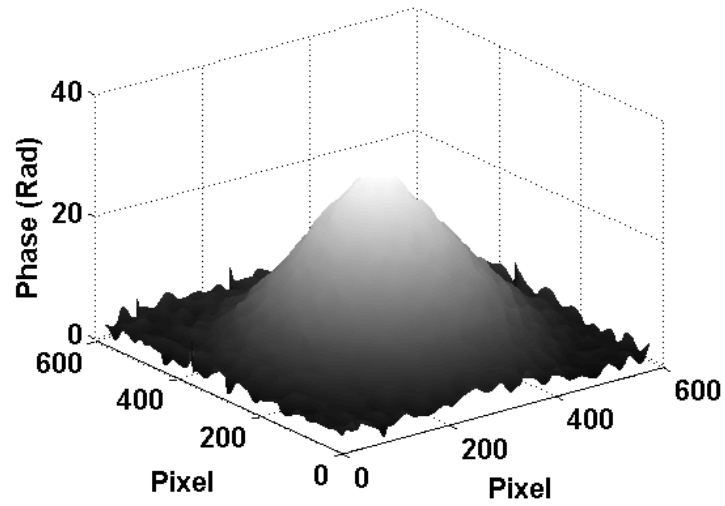
the proposed 2D Gabor CWT produces better results than the other two methods in terms of speckle noise reduction. Although the 2D Fourier transform method can be used to directly retrieve the phase values, the noise in the window would still affect the results and thus the window size should be selected carefully. In contrast, the proposed 2D Gabor CWT has removed most of the speckle noise using the maximum modulus algorithm. When the local fringe direction angle is equal to the rotation angle of the 2D Gabor wavelet and the local fringe period satisfies the condition $q = (k_0 / 2\pi)P$, the modulus of the 2D CWT coefficient reaches a maximum value. Using the maximum modulus algorithm the phase values can be extracted with the speckle noise suppression effectively. Figure 5.7 shows an unwrapped phase map with carriers removed using the 2D Gabor CWT and Fig. 5.8 shows the 3D phase maps obtained using the advanced 2D fan CWT, 2D Fourier transform and 2D Gabor CWT, respectively. As can be seen, the speckle noise is effectively suppressed using the proposed 2D Gabor CWT and the deformation of the plate can be obtained.



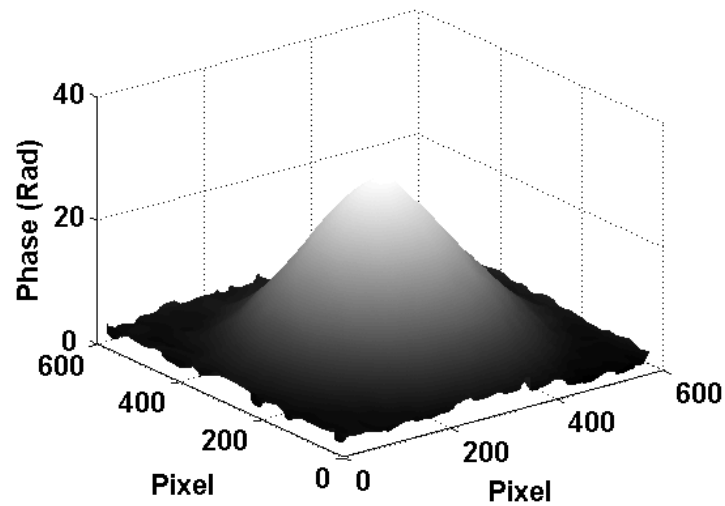
Fig. 5.7 Unwrapped phase map with carriers removed using 2D Gabor CWT



(a)



(b)



(c)

Fig. 5.8 (a) 3D phase map using advanced 2D fan CWT; (b) 3D phase map using 2D Fourier transform; (c) 3D phase map using 2D Gabor CWT

5.2 Improved WFT for fringe demodulation in DSSI

An improved algorithm of WFT for fringe demodulation in DSSI has been proposed. The algorithm is able to reduce the computation time efficiently. The program of the proposed algorithm is made using the Matlab platform and shown in Appendix B.

5.2.1 Simulated analysis

The phase value of a simulated speckle fringe pattern of 512×512 pixels is given by

$$\phi(x+257, y+257) = 50 \times \frac{x}{96} \times \exp \left[-\left(\frac{x}{96} \right)^2 - \left(\frac{y}{96} \right)^2 \right] \quad (5.3)$$

where the values of x and y range from -256 to 255 with an interval of 1, and $50/96$ is a coefficient of the simulated phase values and should be suitably selected for the modulation by a carrier. A simulated phase map using the above equation is shown in Fig. 5.9(a). The speckle fringe pattern with a carrier and white Gaussian noise is given by

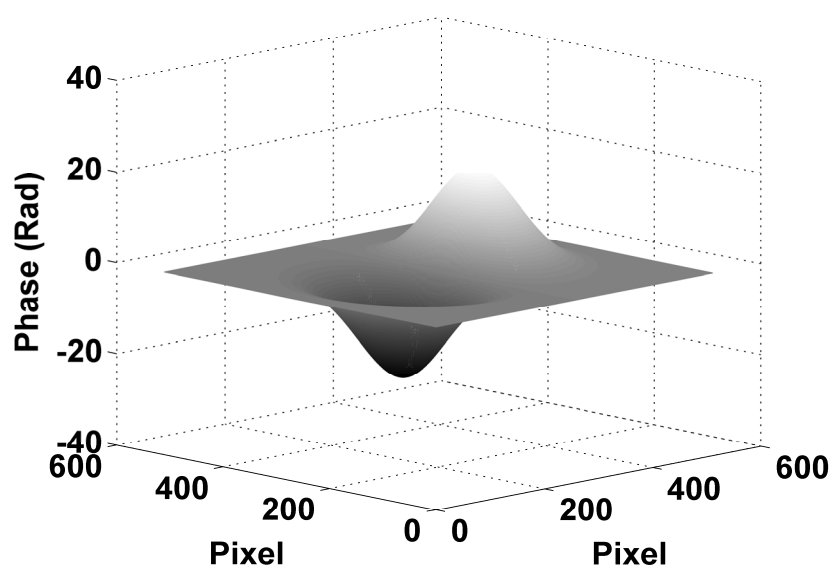
$$I(x+257, y+257) = \cos \left[\pi \times \frac{x}{10} + \phi(x+257, y+257) \right] + WGN \quad (5.4)$$

where $(\pi x)/10$ represents a carrier phase in the x direction and WGN denotes white Gaussian noise with a zero mean value and a variance of 0.6. A simulated speckle-shearing fringe pattern using Eq. (5.4) is shown in Fig. 5.9(b). Before applying the

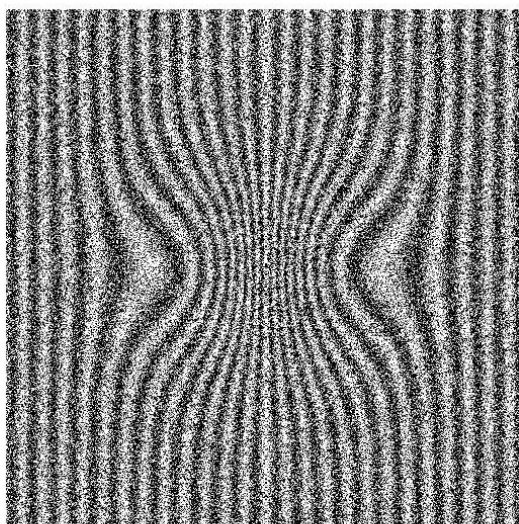
proposed WFF algorithm to demodulate the simulated fringe pattern, extrapolation of the fringe pattern at each boundary (with 20 pixels) is carried out using the Gerchberg method to remove the boundary effect. Figure 5.10 shows an extrapolated fringe pattern. The proposed WFF method is subsequently applied to the extrapolated fringe pattern to retrieve the phase values. Excess extrapolated pixels at the boundary are removed to obtain the original size. Figure 5.11(a) shows a retrieved phase map using the proposed WFF method from Fig. 5.10 after removing the extrapolated boundary pixels. For comparison, Fig. 5.11(b) shows a retrieved phase map using the WFF with convolution method (Qian, 2007b). Figures 5.12(a) and 5.12(b) show the error maps using the proposed WFF and the WFF with convolution method resulting from the retrieved phase values minus the simulated phase values, respectively. The corresponding error values of each method in Fig. 5.12(a) and Fig. 5.12(b) are shown in Table 5.1. As can be seen, both methods show similar error values. However, the computation time of the proposed WFF method for phase retrieval is 65.94 seconds (including 3.62 seconds for fringe extrapolation), while the computation time by the WFF with convolution method for phase retrieval from Fig. 5.9(b) is 563.41 seconds, as shown in Table 5.1. The computer used is a Dell Optiplex GX620 PC with a windows XP operating system and a Matlab 7.1 software. The window size σ in both methods is 16, ε_l and ε_h are 0 and 1 respectively with an interval of 0.1, γ_l and γ_h are -0.3 and 0.3 respectively with an interval of 0.1. The threshold set for the proposed WFF method is 7 and for the WFF with convolution method is 450. It is noteworthy that the computation time is not affected by the window size in the

proposed WFF method. Although the proposed WFF method shows an improvement in the computation time, the WFF with convolution method has the advantage of not requiring a complex boundary extension algorithm. The importance of the proposed WFF method in speed will be shown especially in real-time dynamic measurement or for processing a large amount of fringe patterns.

In addition, the proposed WFF method is also able to process complex fringe patterns with speckle noise and produce less error for some interferograms with both dense and sparse fringes. Figure 5.13(a) shows a simulated speckle fringe pattern with both dense and sparse fringes and Fig. 5.13(b) shows an error map using the proposed WFF method without using boundary extension. As can be seen from Fig. 5.13(b), without using any boundary extension method the phase error will affect the boundary pixels as much as fourteen pixels. Therefore, the fringe pattern is extended with twenty pixels at each boundary to reduce the error. Table 5.2 shows the comparison of RMSE between the Fourier transform, 2D Gabor CWT and proposed WFF method for phase retrieval of Fig. 5.13(a). As can be seen, the Gerchberg method is suitable to reduce the boundary effect and the proposed WFF method is able to retrieve the phase with less RMSE compared with the other methods.



(a)



(b)

Fig. 5.9 (a) Simulated phase map; (b) simulated speckle-shearing fringe pattern

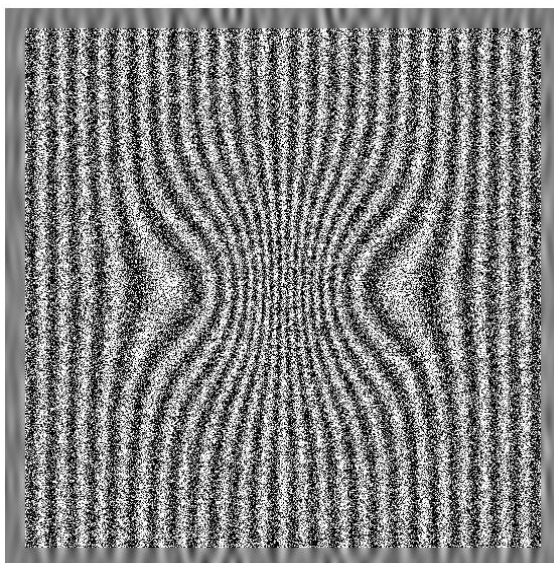


Fig. 5.10 Extrapolated fringe pattern

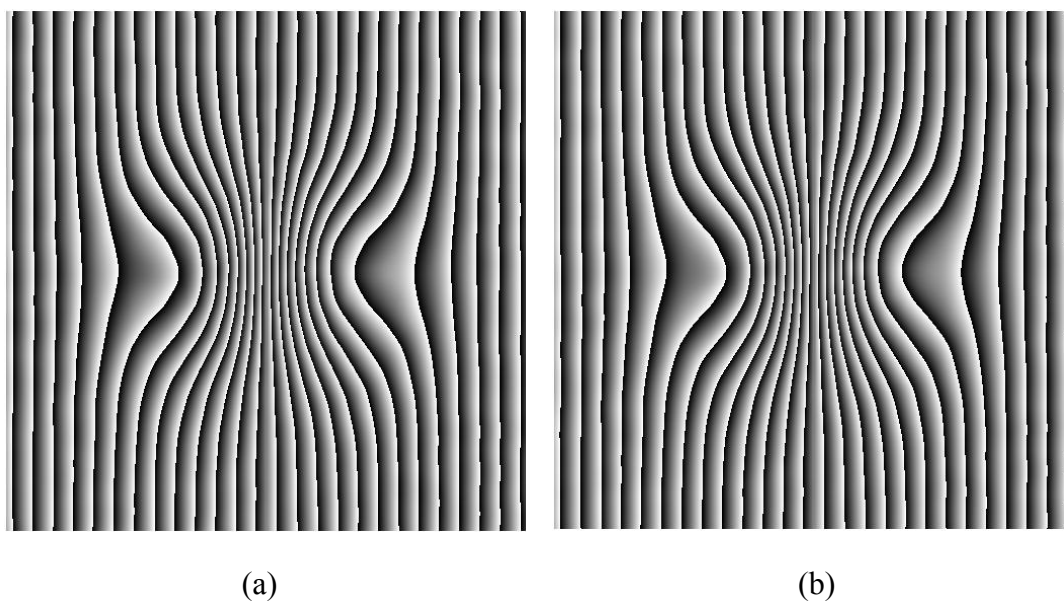


Fig. 5.11 (a) Retrieved phase map using the proposed WFF method;
(b) retrieved phase map using the WFF with convolution method

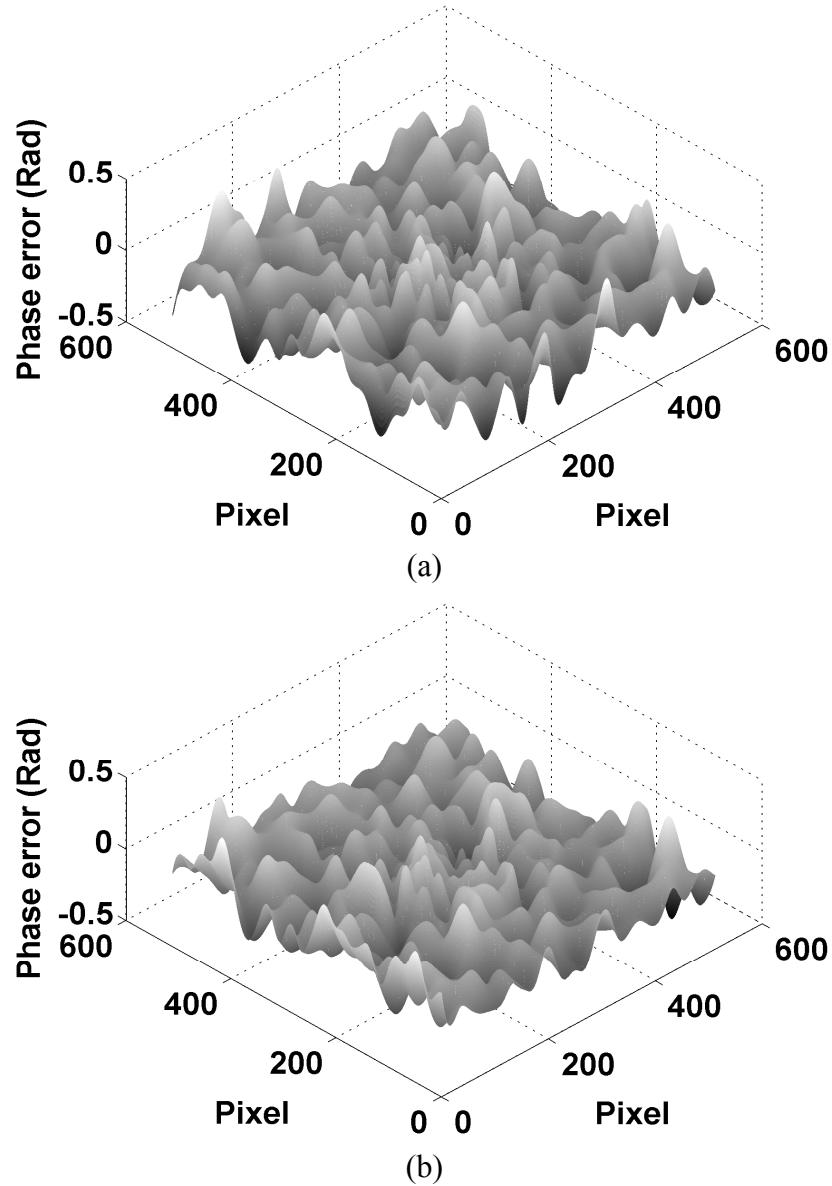
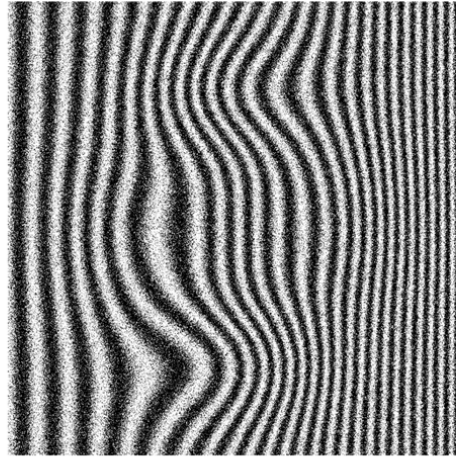


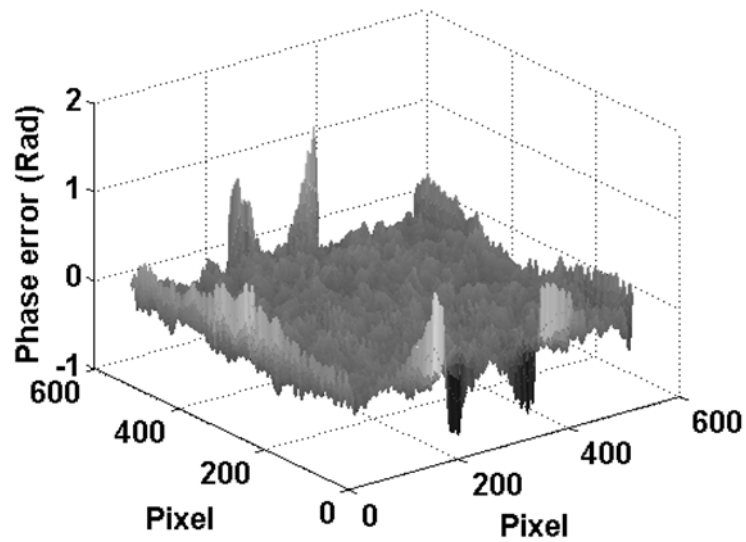
Fig. 5.12 (a) Error map by the proposed WFF method; (b) error map by the WFF with convolution method

Table 5.1 Comparison between the proposed method and the WFF with convolution method

Methods	Maximum error (rad)	Minimum error (rad)	RMSE (rad)	Time for simulated fringes (seconds)	Time for experimental fringes (seconds)
Proposed WFF algorithm	0.4133	-0.4230	0.1028	65.94	44.05
WFF with convolution method	0.4483	-0.4603	0.1053	563.41	337.87



(a)



(b)

Fig. 5.13 (a) A simulated speckle fringe pattern with both dense and sparse fringe patterns; (b) error map using the proposed WFF method without using boundary extension

Table 5.2 Comparison of RMSE between the Fourier transform, 2D Gabor CWT and proposed WFF method

Methods	No boundary extension	Zero-padded	Gerchberg
Fourier transform	0.1095	0.1049	0.0935
2D Gabor CWT	0.1253	0.0890	0.0857
Proposed WFF	0.0853	0.0875	0.0752

5.2.2 Experimental results

The speckle fringe patterns are obtained from the DSSI with carriers for out-of-plane displacement derivative measurement. The image size of the speckle fringe pattern used for processing is 465×481 pixels. Figure 5.14(a) shows a speckle fringe pattern representing the displacement derivative of a deformed flat plate fully clamped at the boundary and Fig. 5.14(b) shows the carriers introduced. Figure 5.14(c) shows the extrapolated speckle fringe pattern based on Fig. 5.14(a) by the Gerchberg method. Figure 5.15(a) shows a phase map retrieved from Fig. 5.14(a) using fast Fourier transform and Fig. 5.15(b) shows a phase map retrieved from Fig. 5.14(c) using the proposed WFF method after the removal of excessive extrapolated pixels. Figure 5.15(c) shows a phase map retrieved from Fig. 5.14(a) using the WFF with convolution method. As can be seen from Fig. 5.15(b), it contains less noise than that of the fast Fourier transform method shown in Fig. 5.15(a) and is comparable with that obtained by the WFF with convolution method. The benefit between noise reduction and signal retention has to be weighed for the WFF method. Figures 5.16(a) and 5.16(b) show respectively the unwrapped phase maps after carrier removal using the proposed WFF and the WFF with convolution method. As can be seen, there are still some noises in the phase map retrieved using the convolution method. This is due to the difference in the threshold values and the extrapolation method used. Figure 5.16(c) shows a plot of the unwrapped phase values along central line CC in Figs. 5.16(a) and 5.16(b). As can be seen, both methods show similar results with a RMSE of 0.49 rad. In both methods, the window size σ is 16, ε_l and ε_h are 0.1 and 0.7

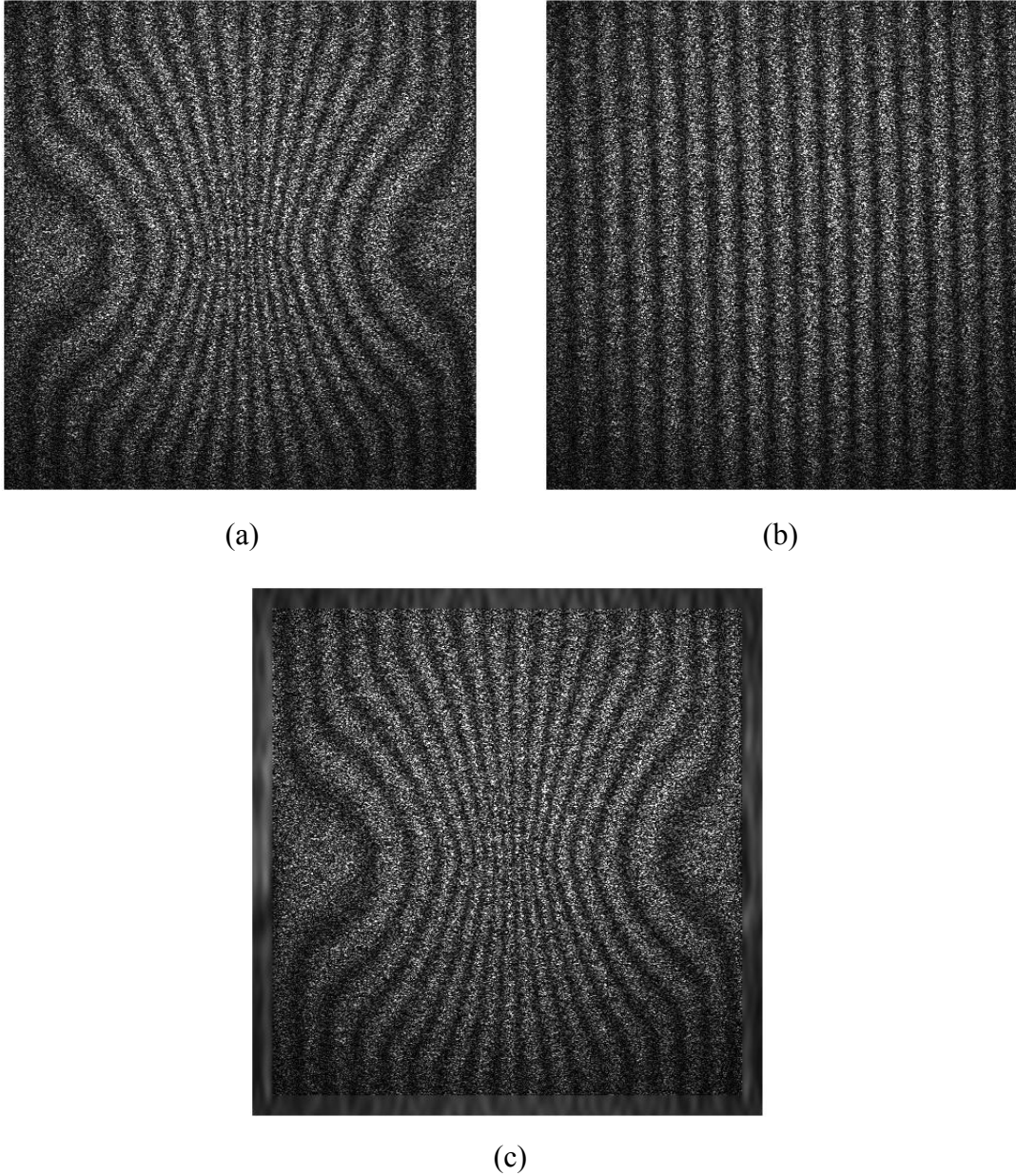


Fig. 5.14 (a) Speckle fringe pattern indicating displacement derivative; (b) carrier fringe pattern; (c) extrapolated speckle fringe pattern based on (a)

respectively with an interval of 0.1, γ_l and γ_h are -0.3 and 0.3 respectively with an interval of 0.1. The thresholds used in the proposed WFF and the WFF with convolution method are 2.55 and 140, respectively. As shown in Table 5.1, the total computation time using the proposed WFF method for phase retrieved from Fig. 5.14(c) is 44.05 seconds while that by the WFF with convolution method for phase

retrieval from Fig. 5.14(a) is 337.87 seconds. Here the proposed WFF method has an advantage in computation time and is not affected by the window size σ . It is noteworthy that the boundary effect for phase retrieval is suppressed using the WFF with convolution method since a zero padded algorithm is employed in the convolution method.

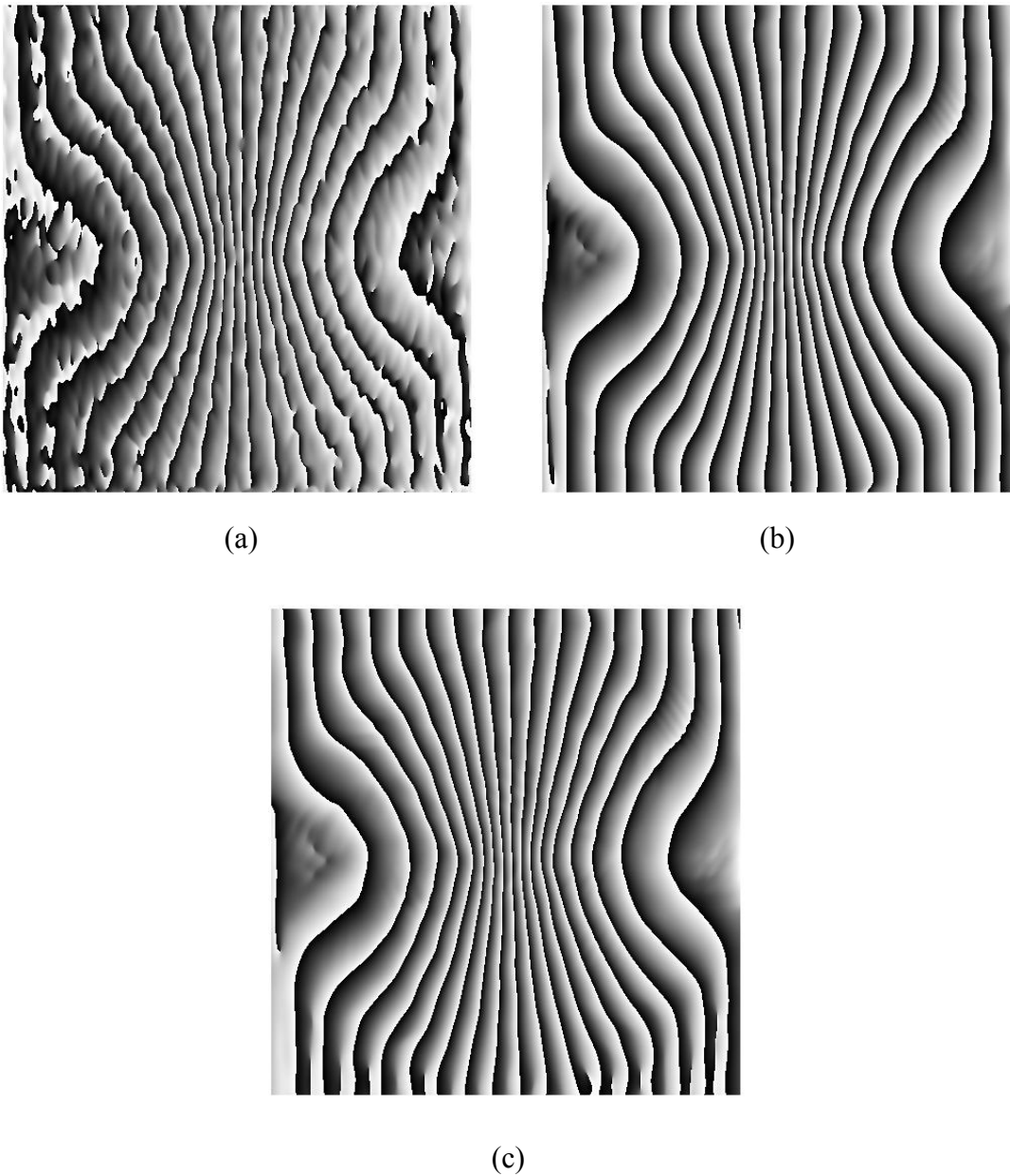
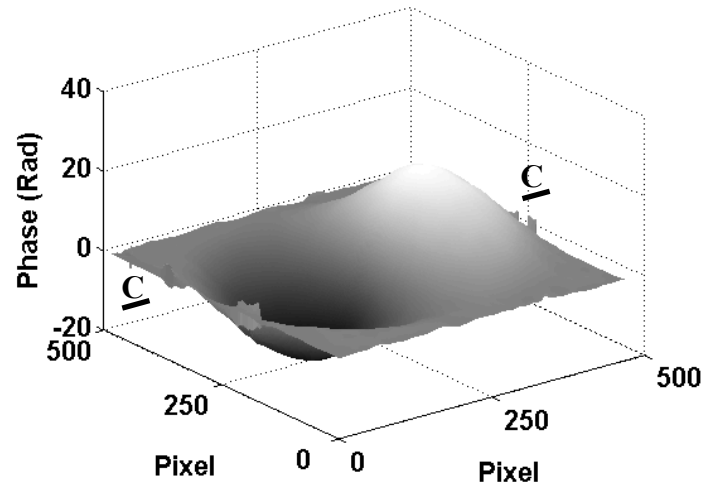
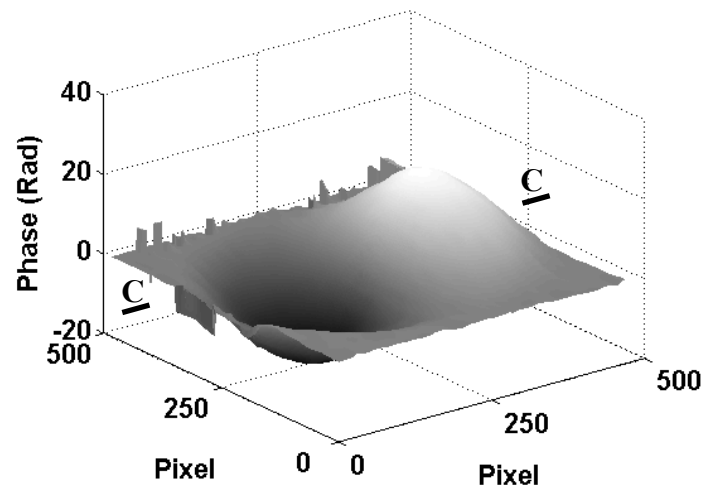


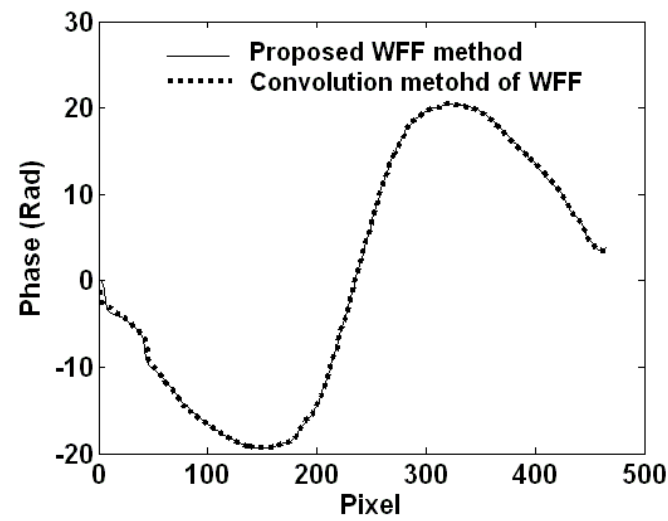
Fig. 5.15 (a) Retrieved phase map using fast Fourier transform method; (b) retrieved phase map using proposed WFF method; (c) retrieved phase map using WFF with convolution method



(a)



(b)



(c)

Fig. 5.16 (a) Unwrapped phase map after carrier removal using proposed WFF method; (b) unwrapped phase map after carrier removal using WFF with convolution method; (c) unwrapped phase values along central line CC in (a) and (b)

5.3 Relatively large deformation measurement

In a dense phase fringe pattern, denoising is an important issue in optical measurement since it determines the measurement range. The ISCAF technique which uses low-pass filtering is no longer suitable in this case. The WFF technique is proposed for phase retrieval from noisy and dense phase fringe patterns obtained using ESPI and DSSI.

5.3.1 Phase fringe denoising in ESPI

For a relatively large deformation measurement in ESPI, phase shifting method has to be employed and would produce a noisy and dense phase fringe pattern. The Carré phase shifting algorithm is used in the experiment since it only requires capturing four phase shifted speckle patterns. To retrieve the correct phase values from a noisy and dense phase fringe pattern obtained using the Carré phase shifting method, denoising is required. Numerical simulation work has been carried out to show the effects of the phase fringe density and speckle size on the results.

5.3.1.1 Simulated results

Figure 5.17 shows a simulated dense wrapped phase map with speckle noise normally encountered when ESPI is used for large deformation measurement. The simulated image size of Fig. 5.17 is 513×513 pixels which has the same pixel number around the image center. The wrapped phase map is simulated using five pixels per period and the phase difference between adjacent pixels in the horizontal direction is $\pi/2$

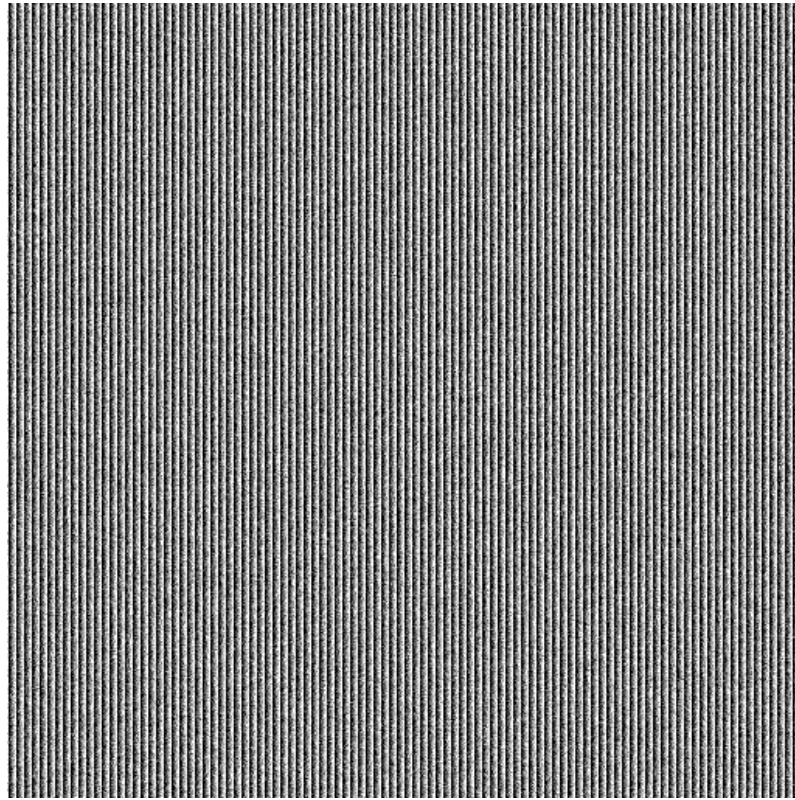


Fig. 5.17 Simulated wrapped phase map with speckle noise

rad. The added noise is Gaussian noise with a zero mean value and a variance of 0.7896. Figure 5.18(a) shows the phase values along the first row of the pixels in Fig. 5.17. As can be seen, the noises introduce errors and difficulties for phase unwrapping of Fig. 5.17 when filtering is not employed. For speckle noise reduction, the fast WFF method is employed. Figure 5.18(b) shows a filtered phase fringe pattern using the fast WFF technique. As can be seen, the noise is effectively suppressed and the RMSE compared with the theoretical phase values is 0.28 rad. A conventional sine-cosine average filter using a 3-by-3 window is also used for comparison and the RMSE is 0.65 rad which is about twice of the fast WFF technique. As can be seen, the fast WFF technique produces a better result than that of the conventional sine-cosine

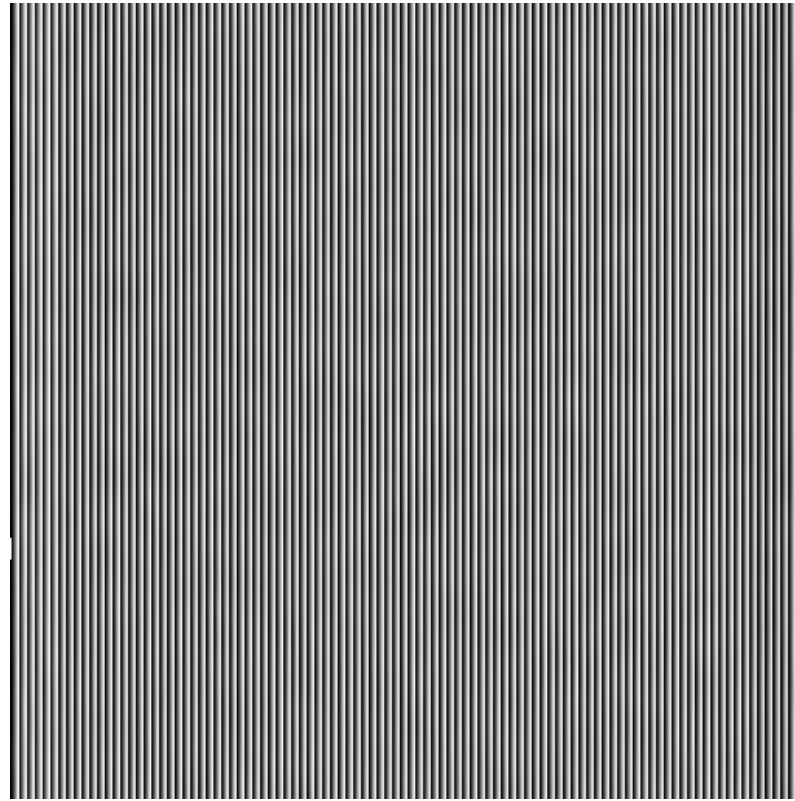
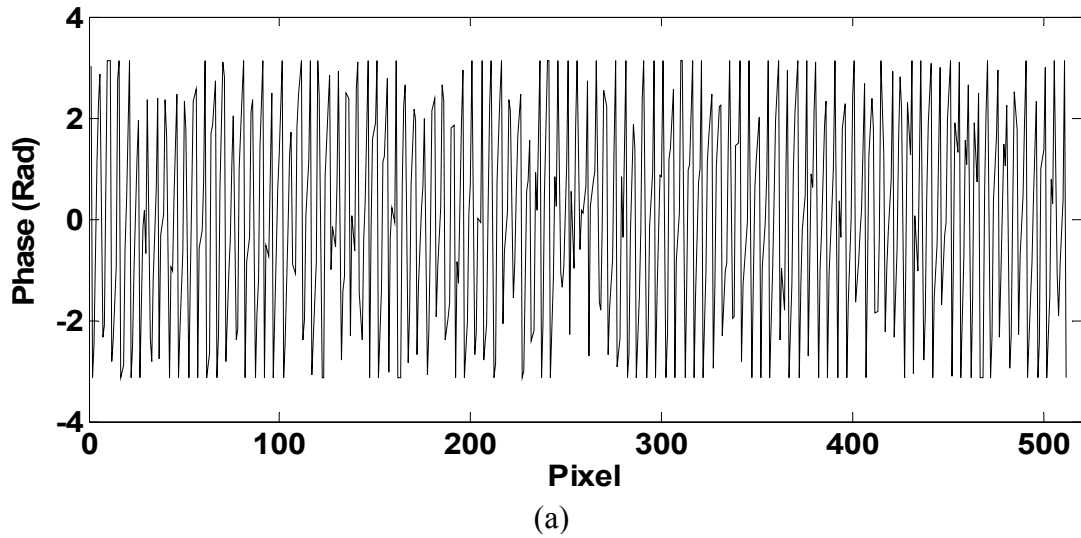


Fig. 5.18 (a) Phase values along the first row of pixels in Fig. 5.17;
 (b) filtered phase fringe pattern using fast WFF technique

average filter. It is noteworthy that when the density of the phase fringe pattern reduces, the RMSE of the proposed fast WFF technique also reduces. For example, the RMSE using the proposed technique is 0.07 rad for a phase fringe pattern of 30

pixels per period. It shows that the dense phase fringe pattern is more difficult for filtering than the sparse phase fringe pattern. In addition, speckle size will also affect the RMSE using the fast WFF technique. Figure 5.19 shows a plot of speckle size versus the RMSE. Four sets of noisy phase fringe patterns with different speckle sizes are simulated and the results are marked as the triangles in the plot. The trend is shown by a dashed line. As can be seen, with increasing speckle size, the RMSE using the fast WFF technique increases. This suggests that a smaller speckle size would produce more accurate results.

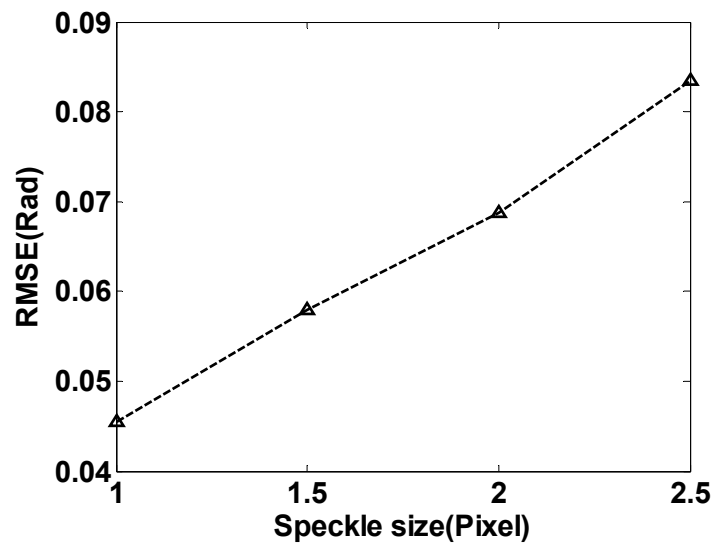


Fig. 5.19 A plot of speckle size versus the RMSE

5.3.1.2 Experimental results

An ESPI system used is shown in Fig. 4.3. Figure 5.20 shows a phase difference map retrieved using the Carré phase shifting method. The speckle noise in the phase difference map will introduce errors in phase unwrapping if filtering is not employed.

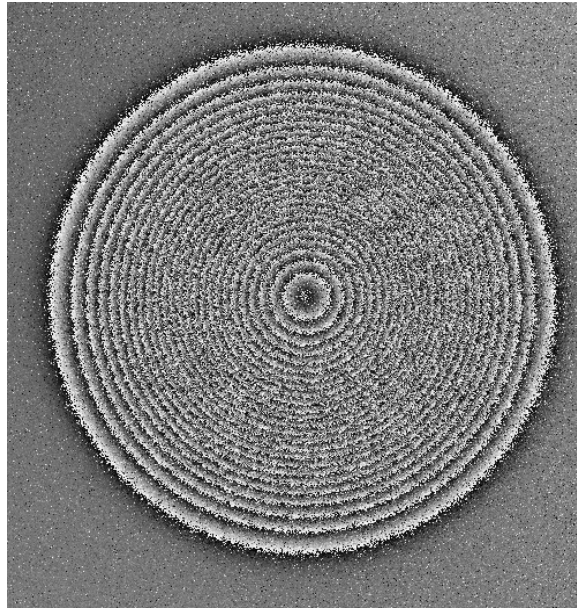
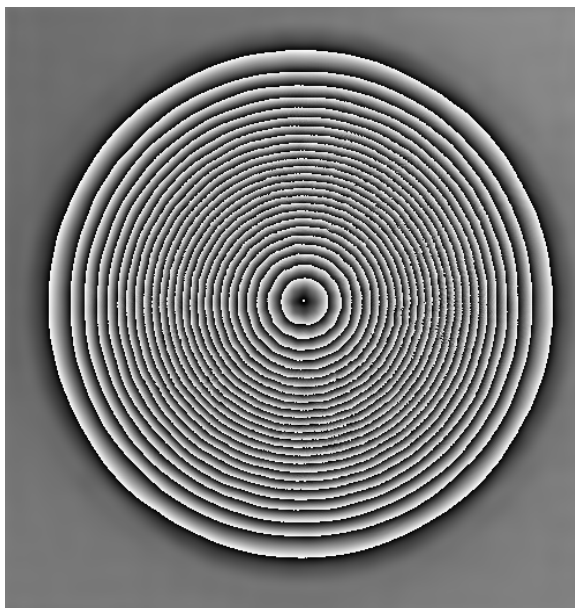
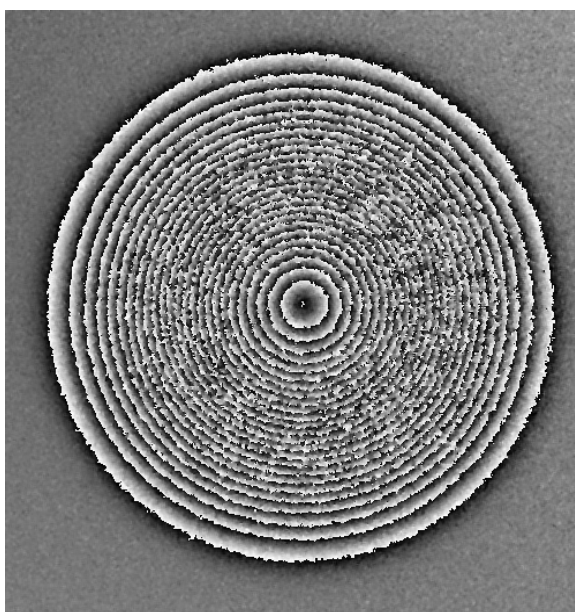


Fig. 5.20 Phase difference map retrieved using Carré phase shifting method

Hence the proposed fast WFF technique is employed for denoising. Figure 5.21(a) shows a filtered phase fringe pattern using the fast WFF technique and Fig. 5.21(b) shows a filtered phase fringe pattern using the conventional sine-cosine average filtering technique. Figures 5.22(a) and 5.22(b) show the corresponding unwrapped phase maps using quality guided phase derivative variance method (Ghiglia and Pritt, 1998). As can be seen, the proposed technique provides a phase fringe pattern with noise suppressed even in areas with a high fringe density which is suitable for phase unwrapping to proceed. The unwrapped phase map can further be employed to obtain the deformation of the object.



(a)



(b)

Fig. 5.21 (a) Filtered phase fringe pattern by fast WFF technique; (b) filtered phase fringe pattern by conventional sine-cosine average filtering technique

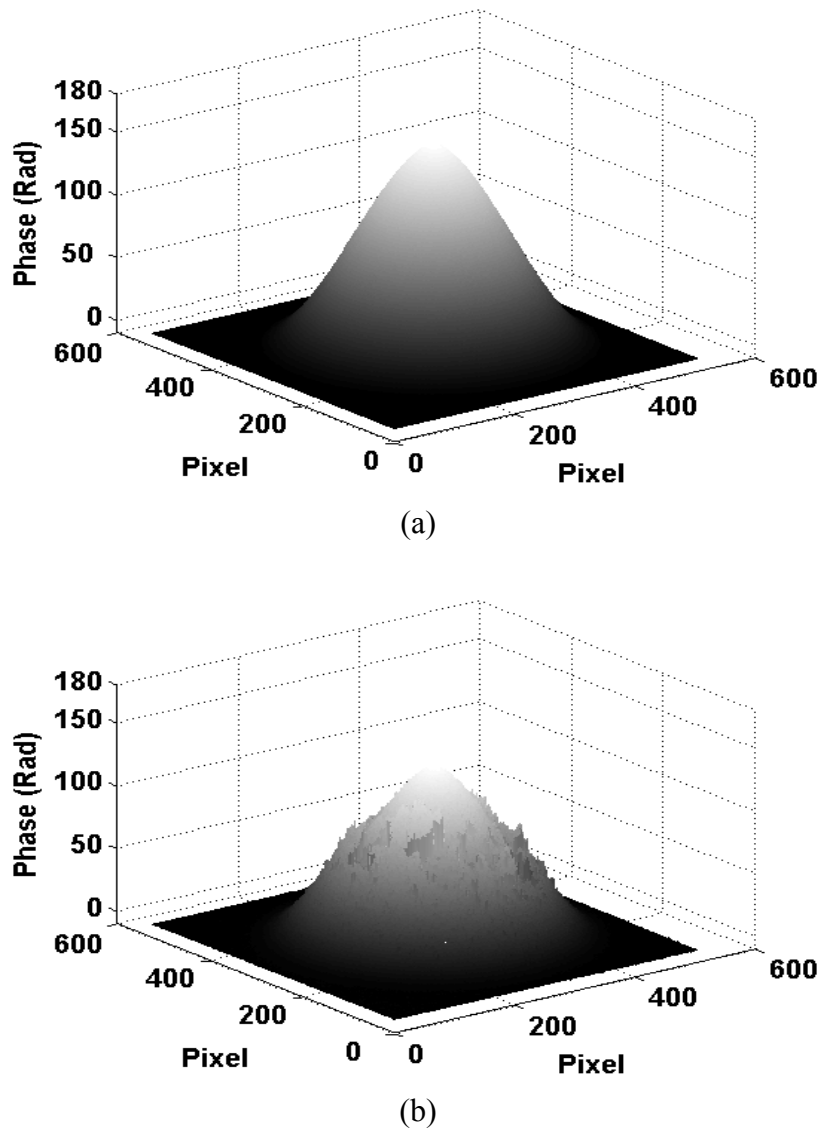


Fig. 5.22 (a) Unwrapped phase map by fast WFF technique; (b) unwrapped phase map by conventional sine-cosine average filtering technique

5.3.2 Phase fringe denoising in DSSI

Figures 5.23 shows the phase difference maps obtained using a two-wavelength DSSI system shown in Fig. 4.4. Figures 5.23(a) and 5.23(b) show respectively the phase difference maps for the red and green lights. Figure 5.24(a) shows a filtered phase map of Fig. 5.23(a) obtained using the ISCAF technique with a 3 by 3 (smallest

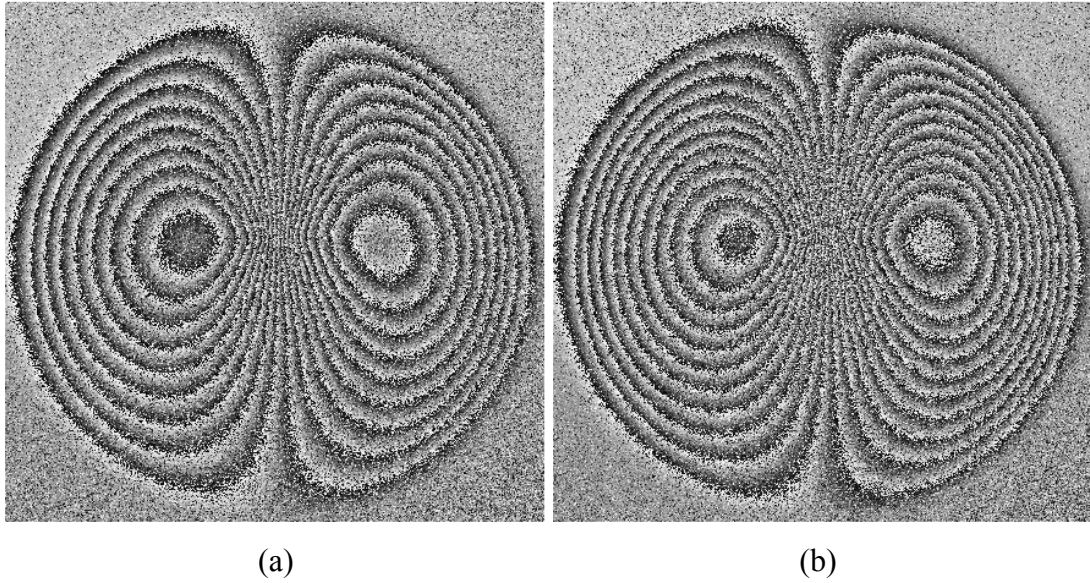


Fig. 5.23 (a) Phase difference retrieved for red light; (b) phase difference retrieved for green light

possible) window and with 10 iterations. As can be seen, the phase fringe pattern is distorted at the central region where the fringe density is high even though the noise at the region with sparse fringes is filtered. The ISCAF technique is not able to produce a satisfied result in this case. Figure 5.24(b) shows a phase difference map of the synthetic wavelength obtained by subtracting the phase difference maps between the red and green lights without filtering. Figure 5.25(a) shows the filtered phase difference obtained using the ISCAF (with a 7 by 5 window and 30 iterations) and the contour of the phase fringes is retrieved. Figure 5.25(b) shows filtered phase values of Fig. 5.23(a) by the fast WFF technique with filtering parameters $\varepsilon l = -2.1$ and $\varepsilon h = 2.1$ with a step of 0.2; $\gamma l = -0.7$ and $\gamma h = 0.7$ with a step of 0.1; $\sigma = 10$ and a threshold value of 0.07. As can be seen from Fig. 5.25(b), effective filtering is achieved even in areas of high fringe density. Figures 5.26 and 5.27 show the

unwrapped phase maps of Figs. 5.25(a) and 5.25(b), respectively. The phase values of the synthetic wavelength in Fig. 5.26 is converted to the phase values of the red light by multiplying a value of λ_s / λ_r . Figure 5.28 shows the phase values along cross-section A-A in Figs 5.26 and 5.27. The dash line is obtained from the converted phase values of Fig. 5.26 whereas the solid line is from Fig. 5.27. As can be seen, both techniques produce similar results.

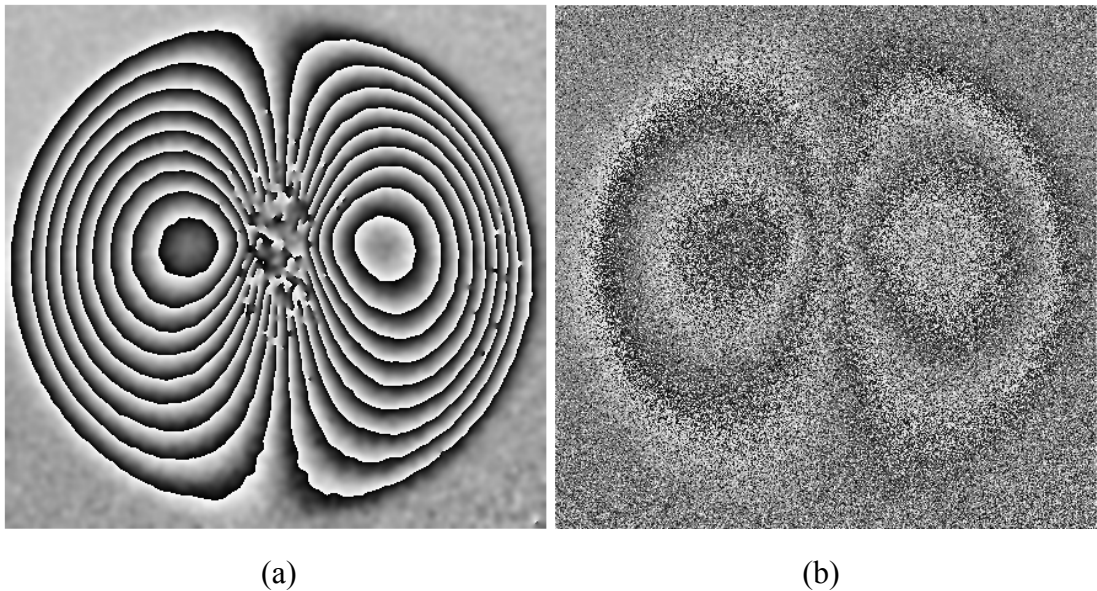


Fig. 5.24 (a) Filtered phase of Fig. 5.23(a) obtained with ISCAF; (b) raw phase difference of the synthetic wavelength obtained by subtracting the phase difference maps between the red and green lights

To validate the results, the slope values obtained from cross-section A-A in Figs 5.26 and 5.27 are compared with those obtained using the strain gauge method. The strain gauge mounted with two gauges in tension and two gauges in compression employs a full-bridge circuit. The load at the center point of the fully clamped circular plate is measured and the displacement derivative for the plate can be estimated from

the measured load. The RMSE between the two-wavelength and the strain gauge method is 3.95×10^{-5} , while the RMSE between the single wavelength and the strain gauge method is 3.86×10^{-5} . As can be seen, the two-wavelength method with ISCAF shows similar results as the single wavelength method with WFF. However, Fig. 5.28 shows a slight difference in phase values representing the maximum slope. This is due to an amplification of the error in the two-wavelength method.

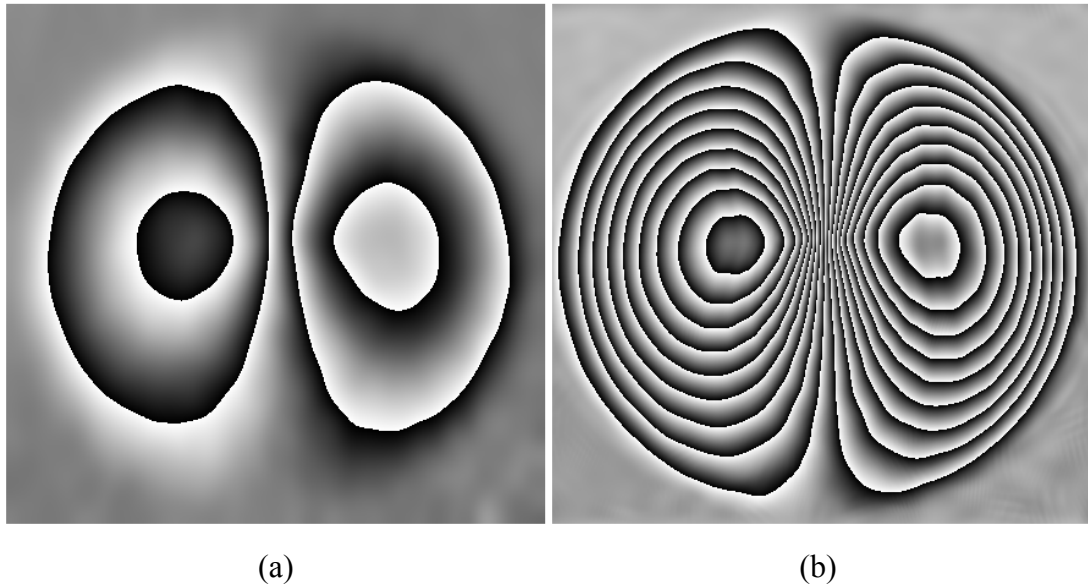


Fig. 5.25 (a) Filtered phase difference of the synthetic wavelength obtained with ISCAF; (b) filtered phase of Fig. 5.23(a) using fast WFF

It is noteworthy that even though the fast WFF algorithm requires more manual intervention than the ISCAF technique, it has a good potential for noise suppression where the fringe density is high. Since the ISCAF technique is a simple filtering technique with the advantage of less manual intervention, it is employed for

noise suppression where the fringe density is relatively low as with two-wavelength simultaneous illumination.

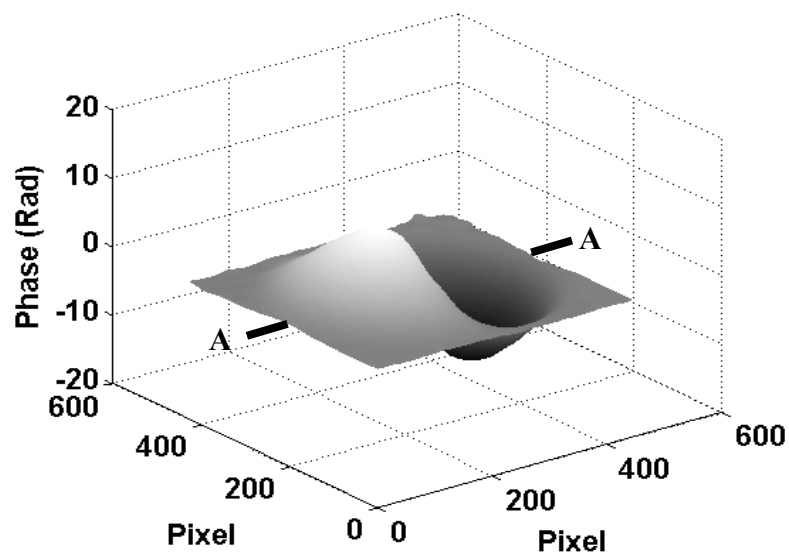


Fig. 5.26 Unwrapped phase map of Fig. 5.25(a)

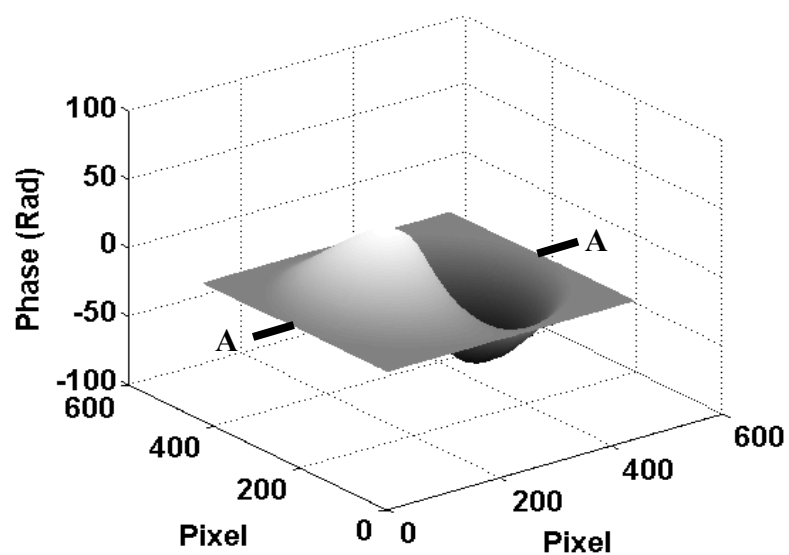


Fig. 5.27 Unwrapped phase map of Fig. 5.25(b)

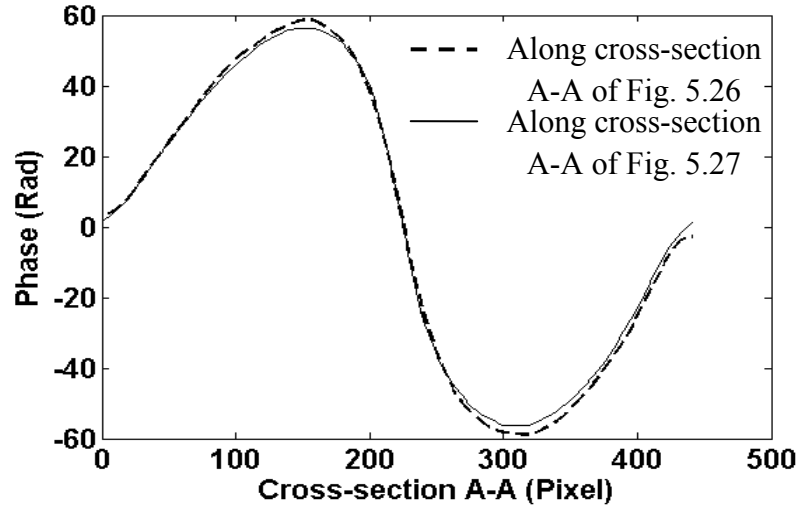


Fig. 5.28 Phase values along cross-section A-A from the unwrapped phase maps using two filtering techniques

5.4 Two-wavelength DSSI using combined filter

The experimental results are obtained for small deformation derivative measurement in two-wavelength DSSI system shown in Fig. 4.4. Figures 5.29(a) and 5.29(b) show wrapped phase maps of $\Delta\phi_r$ (for $\lambda_r = 632.8$ nm) and $\Delta\phi_g$ (for $\lambda_g = 532$ nm) retrieved by the Carré phase shifting algorithm, respectively. The wrapped phase maps $\overline{\Delta\phi_r}$ and $\overline{\Delta\phi_g}$ filtered using the fast WFF technique are shown in Figs. 5.29(c) and 5.29(d), respectively. Figure 5.30(a) shows a phase map of $\Delta\phi_s$ for a synthetic wavelength $\lambda_s = 3.3398$ μm obtained by subtraction of phase maps shown in Figs. 5.29(c) and 5.29(d) whereas Fig. 5.30(b) shows a filtered phase map $\overline{\Delta\phi_s}$ obtained using the fast WFF technique. The parameters of the fast WFF algorithm used for obtaining Figs. 5.29(c), 5.29(d) and 5.30(b) are shown in Table 5.3. The phase map shown in Fig. 5.30(b) is already an unwrapped phase map though no unwrapping

procedure has been carried out. To improve the sensitivity of the two-wavelength technique, integral multiples of 2π obtained from $\overline{\Delta\phi_s}$ are utilized for unwrapping of $\overline{\Delta\phi_g}$, the filtered phase map for the green light.

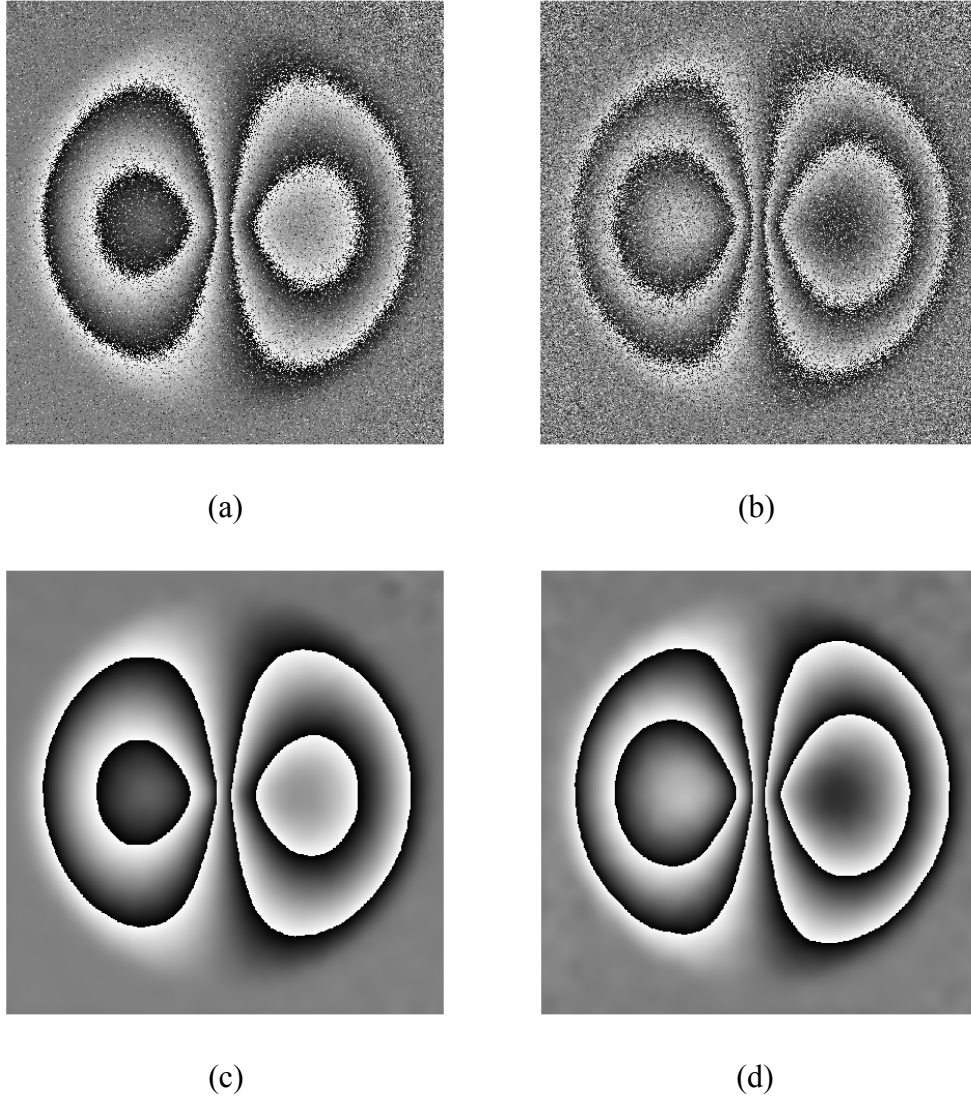


Fig. 5.29 (a) Wrapped phase $\Delta\phi_r$ for red light; (b) wrapped phase $\Delta\phi_g$ for green light; (c) filtered wrapped phase $\overline{\Delta\phi_r}$; (d) filtered wrapped phase $\overline{\Delta\phi_g}$

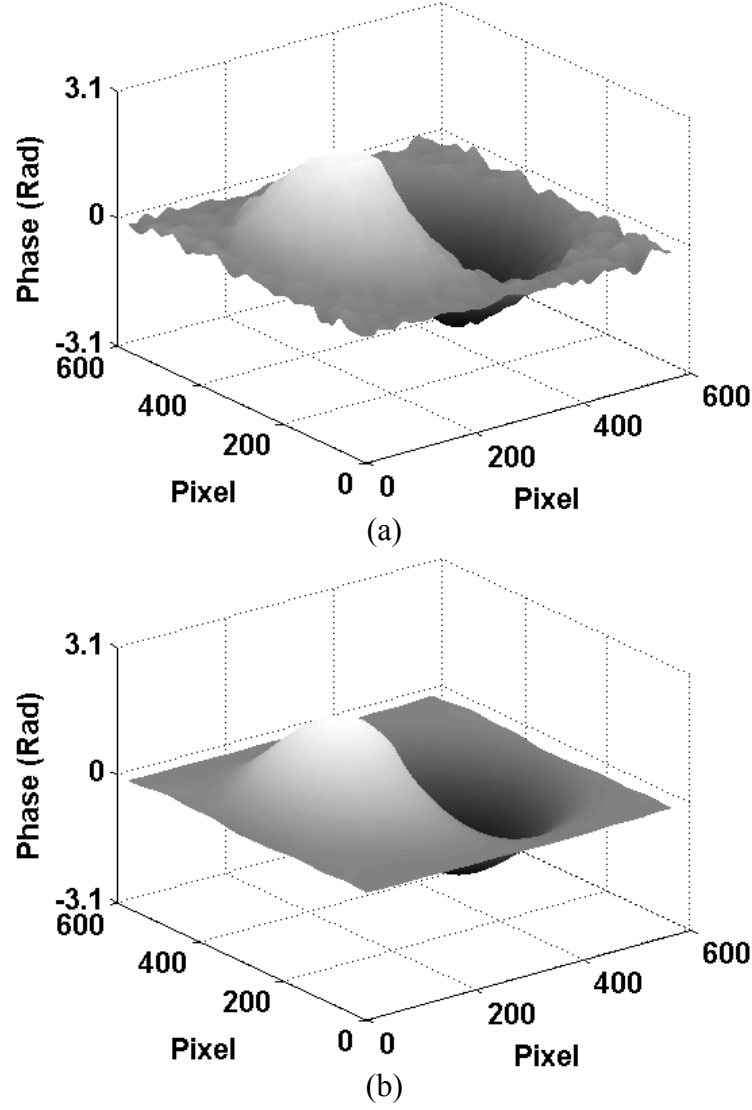


Fig. 5.30 (a) Phase $\Delta\phi_s$ for synthetic wavelength $\lambda_s = 3.3398 \text{ } \mu\text{m}$; (b) filtered phase $\overline{\Delta\phi_s}$

Table 5.3 Parameters used for the fast WFF algorithm

	Window size σ	Integration in x -direction $\epsilon l : step : \epsilon h$	Integration in y -direction $\gamma l : step : \gamma h$	Threshold values
Fig. 5.29(c)	10	-1:0.1:1	-0.3:0.1:0.3	0.15
Fig. 5.29(d)	10	-1:0.1:1	-0.3:0.1:0.3	0.15
Fig. 5.30(b)	18	-0.6:0.1:0.6	-0.6:0.1:0.6	0.6

Figure 5.31(a) shows an unwrapped phase map $\Delta\phi_{gu}$ obtained using $\overline{\Delta\phi_g}$ and $Coef$ (as explained in Sec. 3.3.2.1) without phase error correction and Fig. 5.31(b) shows a corresponding 3D plot of the phase values. It can be seen from Fig. 5.31(b) that there are noticeable errors in the form of spikes which are caused by incorrect 2π integral multiples obtained from $\overline{\Delta\phi_s}$. $\overline{\Delta\phi_{gu}}$ represents the filtered values of $\Delta\phi_{gu}$ and is assigned the values of $\Delta\phi_{gu}$. Phase error correction algorithm is then applied to remove the spikes. Figure 5.32(a) shows the phase $\Delta\phi_{gu}$ (Line 1) along cross-section A-A in Fig. 5.31(a) and the corresponding values of $Coef_diff$ (Line 2). Figure 5.32(b) shows the initial distribution of Fig. 5.32(a) from 1 to 120 pixels. As can be seen, each spike in Line 1 corresponds to a pair of positive and negative numbers in Line 2. Hence, with the line scanning of the values of $Coef_diff$, spikes in each line of $\overline{\Delta\phi_{gu}}$ can be detected and the phase values of $\overline{\Delta\phi_{gu}}$ within the upward and downward spikes can be corrected by subtracting or adding a value of 2π , respectively. The corrected phase map $\overline{\Delta\phi_{gu}}$ is shown in Fig. 5.32(c). As can be seen, the spikes have been removed completely and the derivative of deformation can be evaluated from $\overline{\Delta\phi_{gu}}$. The phase values shown in Fig. 5.32(c) have also been compared with the unwrapped phase obtained by spatially unwrapping $\overline{\Delta\phi_g}$ using quality guided phase derivative variance method and it is found that the RMSE between them is negligible. Thus the proposed technique using a two-wavelength interferometry has a novelty that the same level of sensitivity as the single wavelength for phase retrieval is achieved.

It should be noted that the phase error correction algorithm can be applied only to continuous surface deformation where the optical path difference between the adjacent pixels is smaller than the wavelength of the light source used. However, with the boundary detection algorithm it could be employed for phase retrieval on discontinuous surface deformation.

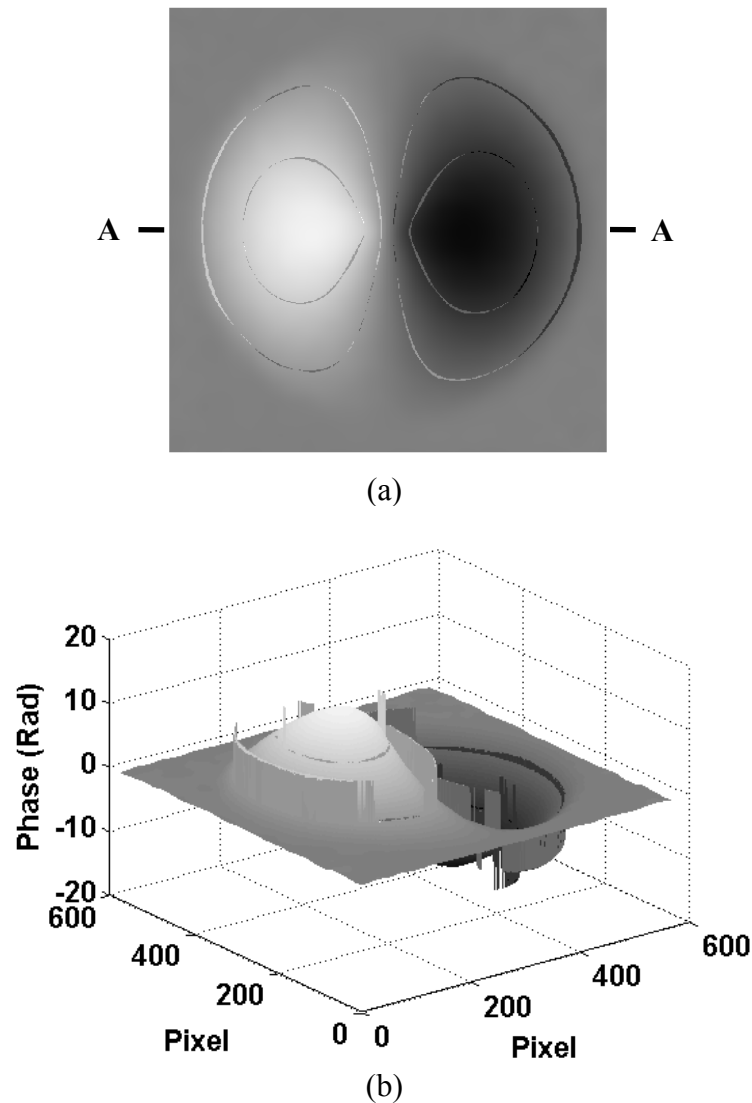


Fig. 5.31 (a) Unwrapped phase $\Delta\phi_{gu}$ without combined filter;
(b) corresponding 3D plot

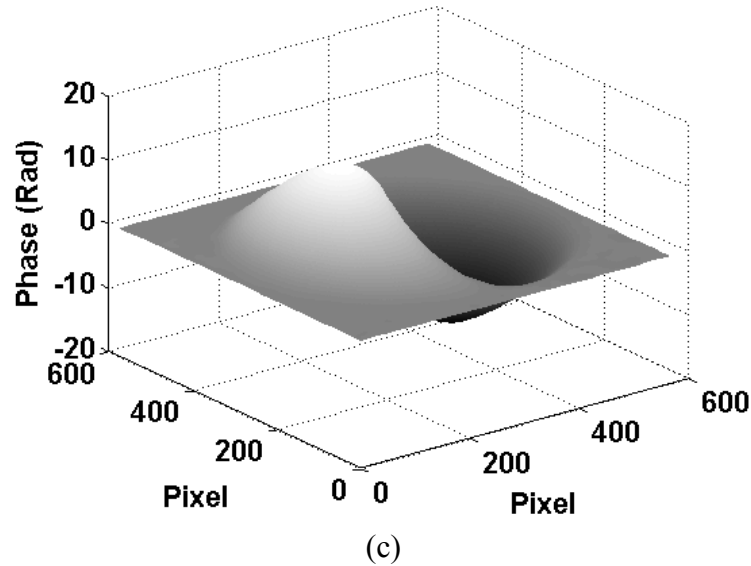
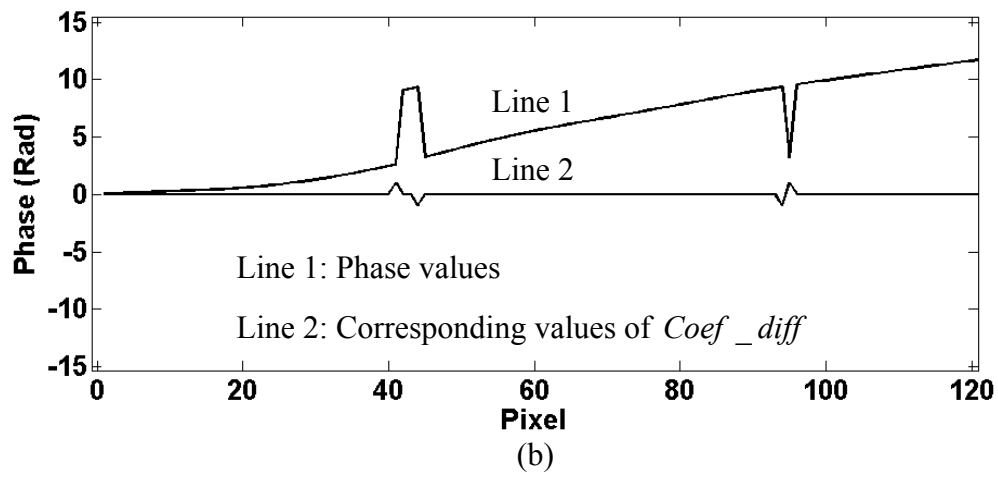
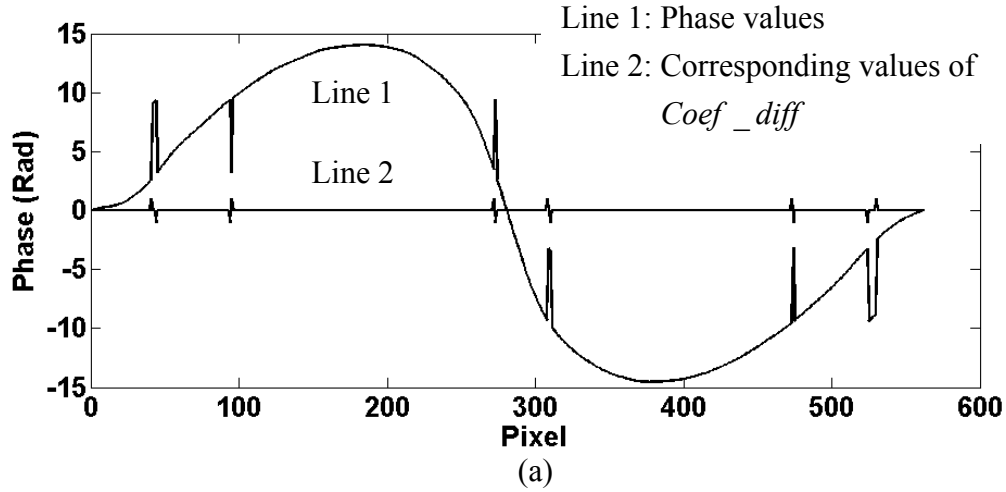


Fig. 5.32 (a) Phase values (Line 1) and corresponding values of $Coef_diff$ (Line 2) on cross-section A-A in Fig. 5.31(a); (b) initial values of Fig. 5.32(a) (from 1 to 120 pixels); (c) phase map $\overline{\Delta\phi_{gu}}$ with combined filter

CHAPTER SIX

CONCLUSIONS AND RECOMMENDATIONS

6.1 Concluding remarks

In this thesis challenging issues in optical measurement techniques like phase retrieval and phase unwrapping are discussed in detail. The time-frequency analysis based techniques for phase retrieval in optical measurement using speckle interferometry and speckle shearing interferometry are discussed. The 2D Gabor CWT is proposed for phase retrieval in speckle interferometry with spatial carriers. The advantages of 2D Gabor CWT over 1D wavelet transform in phase retrieval from fringe patterns are addressed. The proposed 2D Gabor CWT utilized the maximum modulus method to retrieve phase information from the coefficients of a wavelet transform. The proposed method is able to reduce the speckle noise effectively. The 2D Gabor wavelet is employed to demodulate fringe patterns with wide bandwidths which could not be correctly demodulated by the 2D fan wavelet transform. Simulated and experimental results show that the proposed 2D Gabor CWT method has a better noise suppression capability.

A time-frequency analysis based technique, namely the WFT, is also employed for phase retrieval from speckle fringe patterns. The proposed WFT utilizes a fast Fourier transform algorithm and reduces computation time significantly compared with the WFT with convolution method. The proposed WFT method has an

advantage over the Fourier transform method for phase retrieval since the WFT is a local transform and simultaneously provides time and frequency information of a signal, while the Fourier transform is a global transform and the signal in different region will affect each other so that the noise reduction capability of the Fourier transform is not satisfied. The proposed WFT method also has an advantage that the resolution of WFT in both time and frequency domain can be selected according to the spectrum of a fringe pattern for phase retrieval since a suitable resolution can retain useful signals and restrict the speckle noise. Simulated and experimental results have shown the validity of the proposed WFT method.

The WFT method is also employed for noise reduction of dense phase fringe patterns obtained using the ESPI and DSSI systems. In ESPI, the effect of phase fringe density and speckle size on the WFF technique is studied and it is shown that a smaller speckle size would improve the noise suppression capability in the WFF. The WFF technique is also employed for dense phase fringe denoising using single wavelength illumination in DSSI for relatively large deformation measurement. Experimental results show that the WFF technique has a better denoising capability than the ISCAF technique and is able to extend the measurement range.

Phase retrieval in two-wavelength DSSI using a combined filtering method is also studied for small deformation derivative measurement. The proposed method exploits the advantages of a two-wavelength technique and is shown to be an alternative to phase unwrapping. It also has the potential for measurement of discontinuous surface profile and deformation when combined with a boundary

detection algorithm.

In conclusion, the novelties of the proposed 2D Gabor CWT method are that the proposed 2D Gabor CWT method is able to overcome the narrow spectrum limitation of the previous 2D CWT and it is also an improvement from the 1D CWT. The novelties of the improved WFT method are that the improved WFT method has a significant improvement in reduction of computation time for fringe pattern demodulation and it is expected in real-time dynamic measurement or for processing a large amount of fringe patterns. It is a new application to phase retrieval and noise reduction in DSSI. It is also a suitable method for noise reduction of a dense phase fringe pattern in relatively large deformation measurement.

6.2 Recommendations

It is recommended that future work could be carried out in the following areas.

Demodulation of a closed fringe pattern is still a challenging problem in optical measurement. Since the Fourier spectrum of a close fringe pattern overlaps each other, the phase values of the fringe pattern can not be correctly retrieved. Many methods have been proposed for phase retrieval on this type of fringe patterns, but there are still limitations, such as low accuracy and complications. Therefore, suitable algorithms need to be developed for demodulation of this kind of fringe patterns. One possible solution is to cut the closed fringe pattern into several regions and perform phase retrieval for each region before combining them to obtain a final phase map.

Dynamic interferometry technique can reduce effects of vibration using the phase shifting interferometry. Since a four-step phase shifting technique was employed for phase retrieval, the accuracy of phase retrieval may be improved if an eight-step phase shifting technique is employed. This would require improvement in a pixelated mask. Thus improvement in phase retrieval technique for the dynamic interferometry can be further studied.

Fringe projection technique is also widely employed in surface profile measurement. However, most of the applications are for static measurement. Accurate color fringe projection using phase shifting method has a potential and can be further studied for dynamic measurement.

REFERENCES

1. Aebischer, H. A. and S. Waldner, A simple and effective method for filtering speckle-interferometric phase fringe patterns, *Opt. Commun.* 162, pp. 205-210. 1999.
2. Afifi, M., A. Fassi-Fihri, M. Marjane, K. Nassim, M. Sidki, and S. Rachafi, Paul wavelet-based algorithm for optical phase distribution evaluation, *Opt. Commun.* 211, pp. 47-51. 2002.
3. Antoine, J. P., P. Carrette, R. Murenzi, and B. Piette, Image analysis with two-dimensional continuous wavelet transform, *Signal Processing* 31, pp. 241-72. 1993.
4. Bone, D. J., Fourier fringe analysis: the two-dimensional phase unwrapping problem, *Appl. Opt.* 30, pp. 3627-3632. 1991.
5. Bruck, H. A., S. R. McNeil, M. A. Sutton, and W. H. Peters, Digital image correlation using Newton-Raphson method of partial differential correction, *Experimental Mechanics* 29, pp. 261-267. 1989.
6. Bruning, J. H., Fringe scanning interferometers, in *Optical Shop Testing*, D. Malacara, ed. (Wiley, New York), pp. 409-437. 1978.
7. Burke, J., T. Bothe, W. Osten, and C. Hess, Reverse engineering by fringe projection, *Proc. SPIE* 4778, pp. 312-324. 2002.
8. Carré, P., Installation et utilisation du comparateur photoélectrique et interférentiel du Bureau International des Poids et Mesures, *Metrologia* 2, pp. 13-23. 1966.
9. Chen, W. J., P. Bu, S. Z. Zheng, and X. Y. Su, Study on Fourier transforms profilometry based on bi-color projecting, *Opt. Laser Tech.* 39, pp. 821-7. 2007.
10. Cheng, Y. and J. C. Wyant, Two-wavelength phase-shifting interferometry, *Appl. Opt.* 23, pp. 4539-4543. 1984.
11. Cheng, Y. and J. C. Wyant, Multiple-wavelength phase-shifting interferometry,

- Appl. Opt. 24, pp. 804-807. 1985.
 12. Choi, Y. B. and S. W. Kim, Phase-shifting grating projection moiré topography, Opt. Eng. 37, pp. 1005-1010. 1998.
 13. Chu, T. C., W. E. Ranson, M. A. Sutton, and W. H. Peters, Applications of digital image correlation techniques to experimental mechanics, Experimental Mechanics 25, pp. 232-244. 1985.
 14. Creath, K., Phase-shifting speckle interferometry, Appl. Opt. 24, pp. 3053-3058. 1985.
 15. Creath, K., Step height measurement using two-wavelength phase-shifting interferometry, Appl. Opt. 26, pp. 2810-2816. 1987.
 16. Cuhe, E., F. Bevilacqua, and C. Depeursinge, Digital holography for quantitative phase-contrast imaging, Opt. Lett. 24, pp. 291-293. 1999.
 17. Dainty, J. C., Laser speckle and related phenomena, in Topics in Applied Physics, vol. 9. Berlin, Germany: Springer-Verlag, 1975.
 18. Decker, J. E., J. R. Miles, A. A. Madej, R. F. Siemsen, K. J. Siemsen, S. D. Bonth, K. Bustraen, S. Temple, and J. R. Pekelsky, Increasing the range of unambiguity in step-height measurement with multiple-wavelength interferometry-application to absolute long gauge block measurement, Appl. Opt. 42, pp. 5670-5678. 2003.
 19. Dorrió, B. V. and J. L. Fernández, Phase-evaluation methods in whole-field optical measurement techniques, Meas. Sci. Technol. 10, pp. R33-R55. 1999.
 20. Durson, A., S. Ozder, and F. N. Ecevit, Continuous wavelet transform analysis of projected fringe patterns, Meas. Sci. Technol. 15, pp. 1768-1772. 2004.
 21. Ennos, A. E., Speckle interferometry, in Laser Speckle and Related Phenomena, J. C. Dainty, Ed. (Springer, Berlin), 9, pp. 203-253. 1975.
 22. Ettemeyer, A., Combination of 3-D deformation and shape measurement by electronic speckle-pattern interferometry for quantitative strain-stress analysis, Opt. Eng. 39, pp. 212-215. 2000.
 23. Fan, H., J. Wang, and Y. S. Tan, Simultaneous measurement of whole in-plane displacement using phase-shifting ESPI, Opt. Laser Eng. 28, pp. 249-57. 1997.
 24. Federico, A. and G. H. Kaufmann, Evaluation of the continuous wavelet
-

- transform method for the phase measurement of electronic speckle pattern interferometry fringes, *Opt. Eng.* 41, pp. 3209-3216. 2002.
25. Flynn, T. J., Consistent 2-D phase unwrapping guided by a quality map, *Proceedings of the 1996 International Geoscience and Remote Sensing Symposium. (IGARSS)*, pp. 057-2059. 1996.
 26. Flynn, T. J., Two-dimensional phase unwrapping with minimum weighted discontinuity, *J. Opt. Soc. Am. A* 14, pp. 2692-2701. 1997.
 27. Ford, H. D., H. Atcha, and R.P. Tatam, Optical fibre technique for the measurement of small frequency separations: application to surface profile measurement using electronic speckle pattern interferometry, *Meas. Sci. Technol.* 4, pp. 601-607. 1993.
 28. Funnell, W. R. J., Image processing applied to the interactive analysis interferometric fringes, *Appl. Opt.* 20, pp. 3245-3250. 1981.
 29. Gao, W., N. T. T. Huyen, S. L. Ho, and K. Qian, Real-time 2D parallel windowed Fourier transform for fringe pattern analysis using Graphics Processing Unit, *Opt. Express* 17, pp. 23147-23152. 2009.
 30. Gdeisat, M. A., D. R. Burton, and M. J. Lalor, Spatial carrier fringe pattern demodulation by use of a two-dimensional continuous wavelet transform, *Appl. Opt.* 45, pp. 8722-32. 2006.
 31. Gerchberg, R. W., Super-resolution through error energy reduction, *Opt. Acta* 21, pp. 709-20. 1974.
 32. Ghiglia, D. C., G. A. Mastin, and L. A. Romero, Cellular-automata method for phase unwrapping, *J. Opt. Soc. Am. A* 4, pp. 267-280. 1987.
 33. Ghiglia, D. C. and L. A. Romero, Robust two-dimensional weighted and unweighted phase unwrapping that uses fast transforms and iterative methods, *J. Opt. Soc. Am. A* 11, pp. 107-117. 1994.
 34. Ghiglia, D. C. and L. A. Romero, Minimum L^p -norm two-dimensional phase unwrapping, *J. Opt. Soc. Am. A* 13, pp. 1999-2013. 1996.
 35. Ghiglia, D. C. and M. D. Pritt, *Two dimensional phase unwrapping: theory, algorithm and software*, New York, Wiley, 1998.
 36. Goldstein, R. M., H. A. Zebker, and C. L. Werner, Satellite radar interferometry: two-dimensional phase unwrapping, *Radio Sci.* 23, pp. 713-
-

720. 1988.
 37. Goodman, J. W., Some fundamental properties of speckle, *J. Opt. SOC. Amer.* 66, pp. 1145-1149. 1976.
 38. Guo, H., H. He, and M. Chen, Gamma correction for digital fringe projection profilometry, *Appl. Opt.* 43, pp. 2906-2914. 2004.
 39. Guo, H., H. He, Y. Yu, and M. Chen, Least-squares calibration method for fringe projection profilometry, *Opt. Eng.* 44, pp. 033603. 2005.
 40. Hack, E., B. Frei, R. Kästle, and U. Sennhauser, Additive-subtractive two-wavelength ESPI contouring by using a synthetic wavelength phase shift, *Appl. Opt.* 37, pp. 2591-2597. 1998.
 41. Huang, J. R., H. D. Ford, and R. P. Tatam, Slope measurement by two-wavelength electronic shearography, *Opt. Lasers Eng.* 27, pp. 321-333. 1997.
 42. Huang, L., Q. Kemao, B. Pan, and A. K. Asundi, Comparison of Fourier transform, windowed Fourier transform, and wavelet transform methods for phase extraction from a single fringe pattern in fringe projection profilometry, *Opt. Lasers Eng.* 48, pp. 141-148. 2010.
 43. Huang, P. S., Q. Hu, F. Jin, and F. P. Chiang, Color-encoded digital fringe projection technique for high-speed three dimensional surface contouring, *Opt. Eng.* 38, pp. 1065-1071. 1999.
 44. Huang, P. S., C. Zhang, and F. P. Chiang, High-speed 3-D shape measurement based on digital fringe projection, *Opt. Eng.* 42, pp. 163-168. 2003.
 45. Huang, P. S. and S. Zhang, Fast three-step phase-shifting algorithm, *Appl. Opt.* 45, pp. 5086-5091. 2006.
 46. Hung, Y. Y. and C. E. Taylor, Speckle-shearing interferometric camera-a tool for measurement of derivatives of surface-displacement, In: *SPIE Proc.* 41, pp. 169-175. 1973.
 47. Hung, Y. Y. and A. J. Durelli, Simultaneous measurement of three displacement-derivatives using a multiple image shearing interferometric camera, *J. Strain Anal.* 14, pp. 81-88. 1979.
 48. Hung, Y. Y., Shearography: a new optical method for strain measurement and nondestructive testing, *Opt. Eng.* 21, pp. 391-395. 1982.
-

49. Hung, Y. Y., Computerized shearography and its application for nondestructive evaluation of composites, in *Manual on Experimental Methods of Mechanical Testing of Composites*, C. H. Jenkins, Ed., Society for Experimental Mechanics, Bethel, CT, 1998.
 50. Huntley, J. M. and H. O. Saldner, Temporal phase unwrapping algorithm for automated interferogram analysis, *Appl. Opt.* 32, pp. 3047-3052. 1993.
 51. Huntley, J. M. and H. O. Saldner, Shape measurement by temporal phase unwrapping: comparison of unwrapping algorithm, *Meas. Sci. Technol.* 8, pp. 986-992. 1997a.
 52. Huntley, J. M. and H. O. Saldner, Error reduction methods for shape measurement by temporal phase unwrapping, *J. Opt. Soc. Am. A* 14, pp. 3188-3196. 1997b.
 53. Høgmoen, K. and O. J. Løkberg, Detection and measurement of small vibrations using electronic speckle pattern interferometry, *Appl. Opt.* 16, pp. 1869-1875. 1977.
 54. Iwahashi, Y., K. Iwata, and R. Nagata, Influence of in-plane displacement in single-aperture and double-aperture speckle shearing interferometry, *Appl. Opt.* 24, pp. 2189-2192. 1985.
 55. Jin, L., T. Yoshizawa, and Y. Otani, Shadow moiré profilometry using the phase-shifting method, *Opt. Eng.* 39, pp. 2119-2123. 2000.
 56. Jin, L. H., Y. Otani, and T. Yoshizawa, Shadow moiré profilometry by frequency sweeping, *Opt. Eng.* 40, pp. 1383-1386. 2001.
 57. Joenathan, C. and B. M. Khorana, Phase-measuring fiber optic electronic speckle pattern interferometer: phase step calibration and phase drift minimization, *Opt. Eng.* 31, pp. 315-321. 1992.
 58. Johansson, S. and K. G. Predko, Performance of a phase-shifting speckle interferometer for measuring deformation and vibration, *J. Phys. E Sci. Instrum.* 22, pp. 289-292. 1989.
 59. Judge, T. R. and P. J. Bryanston-Cross, A review of phase unwrapping techniques in fringe analysis, *Opt. Lasers Eng.* 21, pp. 199-239. 1994.
 60. Kadooka, K., K. Kunoo, N. Uda, K. Ono, and T. Nagayasu, Strain analysis for moiré interferometry using the two-dimensional continuous wavelet transform, *Exp. Mech.* 43, pp. 45-51. 2003.
-

61. Kato, J., I. Yamaguchi, and Q. Ping, Automatic deformation analysis by a TV speckle interferometer using a laser diode, *Appl. Opt.* 32, pp. 77-83. 1993.
 62. Kaufmann, G. H. and G. E. Galizzi, Phase measurement in temporal speckle pattern interferometry: comparison between the phase-shifting and the Fourier transform methods, *Appl. Opt.* 41, pp. 7254-63. 2002.
 63. Kaufmann, G. H., Phase measurement in temporal speckle pattern interferometry using the Fourier transform method with and without a temporal carrier, *Opt. Comm.* 217, pp. 141-9. 2003.
 64. Kirby, F., Which wavelet best reproduces the Fourier power spectrum, *Comput. Geosci.* 31, pp. 846-64. 2005.
 65. Kong, I. B. and S. W. Kim, General algorithm of phase-shifting interferometry by iterative least-squares fitting, *Opt. Eng.* 34, pp. 183-187. 1995.
 66. Kreis, T., *Handbook of holographic interferometry*, Wiley-VCH, 2005.
 67. Kumar, U. P., N. K. Mohan, and M. P. Kothiyal, Measurement of discontinuous surfaces using multiple-wavelength interferometry, *Opt. Eng.* 48, pp. 073603. 2009a.
 68. Kumar, U. P., B. Bhaduri, N. K. Mohan, and M. P. Kothiyal, Two wavelength micro-interferometry for 3-D surface profiling, *Opt. Lasers Eng.* 47, pp. 223-229. 2009b.
 69. Kumar, U. P., N. K. Mohan, M. P. Kothiyal, and A. K. Asundi, Deformation and shape measurement using multiple wavelength microscopic TV holography, *Opt. Eng.* 48, pp. 023601. 2009c.
 70. Lim, H., W. Xu, and X. Huang, Two new practical methods for phase unwrapping, *IEEE Trans. Geosci. Remote Sens. IGARSS'95* 33, Firenze, Italy, pp. 196-198. 1995.
 71. Løkberg, O. J. and K. Høgmoen, Vibration phase mapping using electronic speckle pattern interferometry, *Appl. Opt.* 15, pp. 2701-2704. 1976.
 72. Løkberg, O. J. and J. T. Malmö, Detection of defects in composite materials by TV-holography, *NDT Int.* 21, pp. 223-228. 1988.
 73. Lu, Y., X. Wang, and X. Zhang, Weighted least-squares phase unwrapping algorithm based on derivative variance correlation map, *Optik* 118, pp. 62-66. 2007.
-

74. Macy, W. W, Two-dimensional fringe-pattern analysis, *Appl. Opt.* 22, pp. 3898-3901. 1983.
 75. Malacara, D., M. Servin, and Z. Malacara, *Interferogram analysis for optical testing*, Marcel Dekker, New York, 1998.
 76. Mallat, S., *A wavelet tour of signal processing*. 2nd ed. San Diego: Academic Press. 2001.
 77. Massie, N. A., R. D. Nelson, and S. Holly, High-performance real-time heterodyne interferometry, *Appl. Opt.* 18, pp. 1797-1803. 1979.
 78. Meadows, D. M., W. O. Johnson, and J. B. Allen, Generation of surface contours by moiré patterns, *Appl. Opt.* 9, pp. 942-947. 1970.
 79. Mohan, N. K. and R.S. Sirohi, Fringe formation in multiaperture speckle shear interferometry, *Appl. Opt.* 35, pp. 1617-1622. 1996.
 80. Moore, A. J. and J. R. Tyrer, An electronic speckle pattern interferometer for complete in-plane displacement measurement, *Meas. Sci. Technol.* 1, pp. 1024-1030. 1990.
 81. Nakadate, S., T. Yatagai, and H. Saito, Digital speckle-pattern shearing interferometry, *Appl. Opt.* 19, pp. 4241-4246. 1980.
 82. Patil, A. and P. Rastogi, Moving ahead with phase, *Opt. Lasers Eng.* 45, pp. 253-257. 2007.
 83. Pedrini, G., Y. L. Zou, and H. Tiziani, Quantitative evaluation of digital shearing interferogram using the spatial carrier method, *Pure Appl. Opt.* 5, pp. 313-321. 1996.
 84. Polhemus, C., Two-wavelength interferometry, *Appl. Opt.* 12, pp. 2071-2074. 1973.
 85. Qian, K., Windowed Fourier transform for fringe pattern analysis, *Appl. Opt.* 43, pp. 2695-2702. 2004.
 86. Qian, K., On window size selection in the windowed Fourier ridges algorithm, *Opt. Lasers Eng.* 45, pp. 1186-1192. 2007a.
 87. Qian, K., Two-dimensional windowed Fourier transform for fringe pattern analysis: principles, applications and implementations, *Opt. Lasers Eng.* 45, pp. 304-317. 2007b.
-

88. Quiroga, J. A., A. Gonzalez-Cano, and E. Bernabeu, Phase unwrapping algorithm based on an adaptive criterion, *Appl. Opt.* 34, pp. 2560-2563. 1995.
 89. Rastogi, P. K., *Digital speckle pattern interferometry and related techniques*, West Sussex: Wiley, 2001.
 90. Robinson, D. W. and G. T. Reid, *Interferogram analysis: Digital fringe pattern measurement techniques*, Institute of Physics, Bristol, UK, 1993.
 91. Roddier, C. and F. Roddier, *Interferogram analysis using Fourier transform techniques*, *Appl. Opt.* 26, pp. 1668-73. 1987.
 92. Saldner, H. O. and J. M. Huntley, Profilometry by temporal phase unwrapping and spatial light modulator based fringe projector, *Opt. Eng.* 36, pp. 610-615. 1997a.
 93. Saldner, H. O. and J. M. Huntley, Temporal phase unwrapping: application to surface profiling of discontinuous objects, *Appl. Opt.* 36, pp. 2770-2775. 1997b.
 94. Sandoz, P., Wavelet transform as a processing tool in white light interferometry, *Opt. Lett.* 22, pp. 1065-1067. 1997.
 95. Shang, H. M., Y. Y. Hung, W. D. Luo, and Frank Chen, Surface profiling using shearography, *Opt. Eng.* 39, pp. 23-31. 2000a.
 96. Shang, H. M., C. G. Quan, C. J. Tay, and Y. Y. Hung, Generation of carrier fringes in holography and shearography, *Appl. Opt.* 39, pp. 2638-2645. 2000b.
 97. Slettemoen, G. A., Electronic speckle pattern interferometric system based on a speckle reference beam, *Appl. Opt.* 19, pp. 616-623. 1980.
 98. Su, X. and W. Chen, Fourier transform profilometry: a review, *Opt. Lasers Eng.* 35, pp. 263-84. 2001.
 99. Takasaki, H., Moiré topography, *Appl. Opt.* 9, pp. 1467-1472. 1970.
 100. Takasaki, H., Moiré topography, *Appl. Opt.* 12, pp. 845-850. 1973.
 101. Takeda, M., H. Ina, and S. Kobayashi, Fourier-transform method of fringe-pattern analysis for computer-based topography and interferometry, *J. Opt. Soc. Am.* 72, pp. 156-160. 1982.
 102. Takeda, M. and K. Mutoh, Fourier transform profilometry for the automatic
-

- measurement of 3-D object shapes, *Appl. Opt.* 22, pp. 3977-3982. 1983.
103. Trillo, C., A. F. Doval, D. Cernadas, O. López, J. C. López, B. V. Dorrio, J. L. Fernández, and M. Pérez-Amor, Measurement of the complex amplitude of transient surface acoustic waves using double-pulsed TV holography and a two-stage spatial Fourier transform method, *Meas. Sci. Technol.* 14, pp. 2127-34. 2003.
 104. Vest, C. M., *Holographic interferometry*, Wiley, New York, 1979.
 105. Wagner, C., W. Osten, and S. Seebacher, Direct shape measurement by digital wavefront reconstruction and multiwavelength contouring, *Opt. Eng.* 39, pp. 79-85. 2000.
 106. Wang, D. N., Y. N. Ning, K. T. V. Grattan, A. W. Palmer, and K. Weir, Three-wavelength combination source for white-light interferometry, *IEEE Photon. Technol. Lett.* 5, pp. 1350-1352. 1993.
 107. Wang, J. and A. Asundi, Strain contouring with Gabor filters: filter bank design, *Appl. Opt.* 41, pp. 7229-36. 2002.
 108. Wang, W., C. Hwang, and S. Lin, Vibration measurement by the time-averaged electronic speckle pattern interferometry methods, *Appl. Opt.* 35, pp. 4502-4509. 1996.
 109. Wang, Z. and H. Ma, Advanced continuous wavelet transform algorithm for digital interferogram analysis and processing, *Opt. Eng.* 45, pp. 045601. 2006.
 110. Warnasooriya, N. and M. K. Kim, Quantitative phase imaging using three-wavelength optical phase unwrapping, *J. Mod. Opt.* 56, pp. 67-74. 2009.
 111. Watkins, L. R., S. M. Tan, and T. H. Barnes, Interferometer profile extraction using continuous wavelet transform, *Electronics Letters* 33, pp. 2116-2117. 1997.
 112. Watkins, L. R., S. M. Tan, and T. H. Barnes, Determination of interferometer phase distributions by use of wavelets, *Opt. Lett.* 24, pp. 905-907. 1999.
 113. Watkins, L. R., Phase recovery from fringe patterns using the continuous wavelet transform, *Opt. Lasers Eng.* 45, pp. 298-303. 2007.
 114. Wyant, J. C., Testing aspherics using two-wavelength holography, *Appl. Opt.* 10, pp. 2113-2118. 1971.
-

115. Wyant, J. C., Dynamic interferometry, *Opt. Phot. News* 14, pp. 38-41. 2003.
116. Xiao, F., J. Wu, L. Zhang, and X. Li, A new method about placement of the branch cut in two-dimensional phase unwrapping, *IEEE trans.* 1-4244-1188-2, 2007.
117. Xu, W. and I. Cumming, A region-growing algorithm for In-SAR phase unwrapping, *IEEE Trans. Geosci. Remote Sens. IGARSS'96* 34, Lincoln, Nebraska, USA, pp. 2044-2046. 1996.
118. Yamaguchi, I. and T. Zhang, Phase-shifting digital holography, *Opt. Lett.* 22, pp. 1268-1270. 1997.
119. Yamaguchi, I., Digital holography and three-dimensional display, pp. 145-171. 2006.
120. Yet Another Wavelet Toolbox (YAWTB), home page: <http://rhea.tele.ucl.ac.be/yawtb/>.
121. Yokozeki, S., K. Patorski, and K. Ohnishi, Collimation method using Fourier imaging and moiré techniques, *Opt. Commun.* 14, pp.401-405. 1975.
122. Zhang, S. and S. T. Yau, Generic nonsinusoidal phase error correction for three-dimensional shape measurement using a digital video projector, *Appl. Opt.* 46, pp. 36-43. 2007.
123. Zheng, S. Z., W. J. Chen, and X. Y. Su, Adaptive windowed Fourier transform in 3-D shape measurement, *Opt. Eng.* 45, pp. 63601-1-4. 2006.
124. Zhong, J. G. and H. P. Zeng, Multiscale windowed Fourier transform for phase extraction of fringe patterns, *Appl. Opt.* 46, pp. 2670-2675. 2007.
125. Zhong, J. and J. Weng, Spatial carrier-fringe pattern analysis by means of wavelet transform: wavelet transform profilometry, *Appl. Opt.* 43, pp. 4993-4998. 2004a.
126. Zhong, J. and J. Weng, Dilating Gabor transform for the fringe analysis of 3-D shape measurement, *Opt. Eng.* 43, pp. 895-899. 2004b.
127. Zhong, J. and J. Weng, Phase retrieval of optical fringe patterns from the ridge of a wavelet transform, *Opt. Lett.* 30, pp. 2560-2562. 2005.

APPENDICES

Appendix A. Code for 2D Gabor and 2D fan CWT

This program is for 2D Gabor and 2D fan CWT in fringe demodulation using Matlab software. The algorithm is programmed with the aid of the Yet Another Wavelet Toolbox (YAWTB).

function [cwtcoef scalex anglex] = cwt2d(fimg, waveletname, scales, angles)

% Two-dimensional continuous wavelet transform for phase retrieval from fringe patterns with carriers

% fimg: Fourier transform of the fringe pattern

% waveletname: Name of the wavelet to use

% scales, angles : Scales and angles of the wavelet transform to use

% cwtcoef : Coefficients of the wavelet transform by maximum modulus method

% scalex, anglex : Scales and angles obtained by maximum modulus method

% The algorithm of 2D wavelet transform is composed with the aid of YAW Toolbox (Yet Another Wavelet Toolbox)

% YAW Toolbox : <http://rhea.tele.ucl.ac.be/yawtb/>

% Obtain the wavelet name

waveletname = lower([waveletname '2d']);

% Obtain the image size


```
[Hgth,Wdth] = size(fimg);

% Warning if the scales contain nonpositive numbers

for i = 1:length(scales)

    if (scales(i) <= 0)

        error("'scales' must be positive');

    end

end

% Construct x and y coordinates in Fourier spectrum

num_half = floor((Wdth-1)/2);

freqlx = 2*pi/Wdth*[ 0:num_half (num_half-Wdth+1):-1 ];

num_half = floor((Hgth-1)/2);

freqly = 2*pi/Hgth*[ 0:num_half (num_half-Hgth+1):-1 ];

[fx,fy] = meshgrid(freqlx,freqly);

% Obtain the number of scales and angles

nsc = length(scales);

nang = length(angles);

h = waitbar(0,'Please wait...'); % Create the progress bar

% Define the parameters for the wavelet transform

cwtcoef = fimg; cwtcoef = 0; scalex = cwtcoef; anglex = cwtcoef;

% Wavelet transform of the maximum modulus method

for scnum = 1:nsc,

    for angnum = 1:nang,
```

```
sc = scales(scnum); % Take a scale from the scale vector

ang = angles(angnum); % Take an angle from the angle vector

% Perform the dilation and rotation of the wavelet in the frequency domain

nfx = sc * ( cos(ang).*fx - sin(ang).*fy );

nfy = sc * ( sin(ang).*fx + cos(ang).*fy );

% Generate a wavelet function in the frequency domain

wavf = sc * feval(waveletname,nfx,nfy);

% Perform wavelet transform

out = ifft2(fimg.* conj(wavf));

% Obtain coefficients of the wavelet transform with maximum modulus method

coef = abs(out)>abs(cwtcoef);

cwtcoef = coef.*out+~coef.*cwtcoef;

scalex = coef*sc+~coef.*scalex; % Obtain scale parameters of the wavelet
transform with maximum modulus method

anglex = coef*ang+~coef.*anglex; % Obtain angle parameters of the wavelet
transform with maximum modulus method

waitbar(scnum/nsc) % Display of the progress bar

end

end
```

function [out] = morlet2d(kx,ky)

% Generate a 2D Gabor wavelet using 2D Morlet wavelet function

% kx, ky : x and y coordinates in the frequency domain

% out : Output of the 2D Gabor wavelet in the frequency domain

% Define wavelet parameters

$k_0 = 5.336;$

$\sigma = 1/2;$ *% Resolution control*

% Fourier spectrum of the wavelet function

$out = \exp(-\sigma^2 * ((kx - k_0).^2 + ky.^2)/2);$

function [out] = fan2d(kx,ky)

% 2D fan wavelet

% kx, ky : x and y coordinates in the frequency domain

% out : Output of the 2D fan wavelet in the frequency domain

% Define wavelet parameters

$k_0 = 5.336;$

$\sigma = 1/2;$ *% Resolution control*

% Superposition of 6 Morlet wavelets

$out = 0;$

for count = 1:6

$sita = (count-1)*\pi/6;$

% Fourier spectrum of the wavelet function

```
outtemp = exp( - sigma^2 * ((ky - k_0*cos(sita)).^2 + (kx- k_0*sin(sita)).^2)/2 );  
  
out = out+outtemp;  
  
end
```

Appendix B. Code for improved WFT

This program includes the improved WFF and windowed Fourier ridges algorithms for phase retrieval from fringe patterns.

function [temp] = winfff(fimg,wx,wy,sigma,thr)

% Windowed Fourier filtering function

% fimg : Fourier transform of the input fringe pattern, which is better with negative and zero frequencies removed firstly

% wx, wy : Selected frequency vectors in x and y direction, respectively

% sigma : Window size

% thr : Threshold

% temp : Coefficients of WFF method

% Example: wffcoef = winfff(fimg,0:0.1:1,-0.3:0.1:0.3,16,7);

% Obtain image size

[Hgth,Wdth] = size(fimg);

% Construct x and y coordinates in Fourier spectrum

[kx,ky] = freqcord2(Wdth, Hgth);

% Initiate coefficients of WFF

temp = fimg; temp = 0;

h = waitbar(0,'Please wait...'); *% Create the progress bar*

% Obtain the number of the elements in the selected frequency vector

```
nwx = length(wx);

nwy = length(wy);

% Compute the WFF coefficients by fast Fourier transform

for cx = 1:nwx

    for cy = 1:nwy

        % Take an element from the selected frequency vector

        wx1 = wx(cx);

        wy1 = wy(cy);

        % Compute windowed Fourier basis in frequency domain

        mask = win(kx,ky,wx1,wy1,sigma);

        % Perform WFT

        out = ifft2(fimg.*mask);

        % Filter the coefficients of the transform by a threshold

        out = out.*(abs(out)>=thr);

        % Perform inverse WFT

        out = fft2(out);

        temp = temp+ifft2(out.*mask);

    end

    waitbar(cx/nwx) % Display of the progress bar

end
```

function [temp scalex scaley] = winffr(fimg,wx,wy,sigma)

% Windowed Fourier ridges method

% fimg : Fourier transform of the input fringe pattern, which is better with negative and zero frequencies removed firstly

% wx, wy : Selected frequency vectors in x and y direction, respectively

% sigma : Window size

% temp : Coefficients of windowed Fourier ridges method

% scalex, scaley : Obtained frequency parameters in x and y direction of the transform with the maximum modulus method

% Example : wfrcoef = winffr(fimg,0:0.1:1,-0.3:0.1:0.3,12);

% Obtain image size

[Hgth,Wdth] = size(fimg);

% Construct x and y coordinates in the Fourier spectrum

[kx,ky] = freqcord2(Wdth, Hgth);

% Initiate coefficients of windowed Fourier ridges method

temp = fimg; temp = 0; scalex = temp; scaley = temp;

h = waitbar(0,'Please wait...'); *% Create the progress bar*

% Obtain the number of the elements in the selected frequency vector

nwx = length(wx);

nwy = length(wy);

% Compute coefficients of windowed Fourier ridges method by fast Fourier transform

for cx = 1:nwx

```
for cy = 1:nwy

    % Take an element from the selected frequency vector

    wx1 = wx(cx);

    wy1 = wy(cy);

    % Compute the windowed Fourier basis in the frequency domain

    mask = win(kx,ky,wx1,wy1,sigma);

    % Perform WFT

    out = ifft2(fimg.* conj(mask));

    % Perform the maximum modulus method

    coef = abs(out)>abs(temp);

    % Obtain the coefficients of the transform with the maximum modulus

    temp = coef.*out+~coef.*temp;

    % Obtain the frequency parameters of the transform with the maximum modulus

    scalex = coef*wx1+~coef.*scalex;

    scaley = coef*wy1+~coef.*scaley;

end

waitbar(cx/nwx) % Display of the progress bar

end
```



```
function [freqx,freqy] = freqcord2(Wdthx, Hgthy)
```

```
% Construct x and y coordinates in the Fourier spectrum
```

```
% freqx, freqy : Matrixs of x and y coordinates of the Fourier spectrum
```

```
% Wdthx, Hgthy : Width and height of the image
```

```
[freqx,freqy] = meshgrid(freqcord1(Wdthx),freqcord1(Hgthy));
```

```
function dout = freqcord1(vars)
```

```
% Construct the coordinates in the Fourier spectrum
```

```
vars_2 = floor((vars-1)/2);
```

```
dout = 2*pi/vars*[ 0:vars_2 (vars_2-vars+1):-1 ];
```

```
function [out] = win(kx,ky,wx,wy,sigma)
```

```
% Compute window function in frequency domain
```

```
out = exp( - sigma^2 * ((kx - wx).^2 + (ky-wy).^2)/2 );
```

Appendix C. List of publications

Journal papers:

1. H. Niu, C. Quan, and C.J. Tay, "Phase retrieval of speckle fringe pattern with carriers using 2D wavelet transform", *Opt. Lasers Eng.* 47(12), 1334-1339, (2009).
2. C. Quan, H. Niu, and C.J. Tay, "An improved windowed Fourier transform for fringe demodulation", *Opt. Laser Technol.* 42(1), 126-131, (2010).
3. H. Niu, C. Quan, C.J. Tay, and B. Bhaduri, "Phase retrieval in DSSI for relatively large deformation", *Opt. Commun.* 284(1), 118-122, (2011).
4. Basanta Bhaduri, C.J. Tay, C. Quan, H. Niu, and Mikael Sjödaahl, "Two wavelength simultaneous DSPI and DSP for 3D displacement field measurements", *Opt. Commun.* 284, 2437-2440, (2011).
5. C.J. Tay, C. Quan, H. Niu, and B. Bhaduri, "Phase retrieval in two-wavelength DSSI using a combined filtering method", *Optik* 122(23), 2114-2118, (2011).

Conference papers:

6. H.T. Niu, C. Quan, and C.J. Tay, "Temporal Paul wavelet analysis for phase retrieval using shadow moiré technique", *Proc. SPIE* 7155, 71552B (2008).
7. H. Niu, C. Quan, and C.J. Tay, "A modified WFT for shape and deformation measurement", *Proc. SPIE* 7522, 752247 (2009).
8. H. Niu, C. Quan, and C.J. Tay, "Phase retrieval in ESPI from a dense phase fringe pattern", *Proc. SPIE* 7718, 771817 (2010).